On the Role of Oxygen Vacancies in the Surface Chemistry of Ceria (CeO_2)

Dissertation

zur Erlangung des akademischen Grades

doctor rerum naturalium

(Dr. rer. nat.)

im Fach Chemie: Spezialisierung:

Physikalische und Theoretische Chemie

eingereicht an der

Mathematisch-Naturwissenschaftlichen Fakultät

der Humboldt-Universität zu Berlin

von

M. Sc. Kristin Werner

Präsidentin der Humboldt-Universität zu Berlin

Prof. Dr.-Ing. Dr. Sabine Kunst

Dekan der Mathematisch-Naturwissenschaftlichen Fakultät

Prof. Dr. Elmar Kulke

Gutachter:
1. Prof. Dr. Hans-Joachim Freund
2. Prof. Dr. Klaus Rademann
3. Prof. Dr. Günther Rupprechter

Datum der Promotion: 11.07.2019

The most exciting phrase to hear in science,
the one that heralds new discoveries,
is not "Eureka!", but
"That's funny...".

Isaac Asimov

Abstract

In recent years, ceria (CeO_2) has attracted much scientific interest due to its activity as a catalyst in the selective hydrogenation of alkynes to alkenes. To gain further insights into the role of CeO_2 in propyne hydrogenation, this thesis explores the fundamental processes of H_2, CO_2, and propyne adsorption, as well as the interaction of hydroxyls and propyne on well-defined $CeO_2(111)$ surfaces. A special emphasis thereby lies on the role of oxygen (O) vacancies in these processes.

H_2 dissociation on $CeO_2(111)$ is an activated process that takes place at elevated pressure and temperature. We show that the dissociation of H_2 on $CeO_2(111)$ leads to the formation of hydroxyls and to a reduction of the oxide surface. If O vacancies are present below the surface of $CeO_2(111)$, H species are incorporated in the form of hydrides. This results in a re-oxidation by electron transfer from Ce^{3+} ions towards H, forming Ce^{4+}. At elevated temperatures, the formation of surface hydroxyls dominates over hydride formation.

We furthermore explore the interaction of CO_2, an often encountered impurity during catalytic reactions, with the $CeO_2(111)$ surface. CO_2 chemisorbs onto $CeO_2(111)$, most likely as a carbonate species, which is stable up to 270 K. The presence of O vacancies on $CeO_2(111)$ stabilizes chemisorbed CO_2.

O vacancies also play an essential role in the adsorption of alkynes on $CeO_2(111)$. While propyne interacts only weakly with stoichiometric $CeO_2(111)$, it is considerably stabilized in the presence of O vacancies.
H_2 and propyne interact only weakly on the $CeO_2(111)$ surface. The previously reported high activity of CeO_2 in hydrogenation could not be reproduced on our model catalyst surface. It appears, however, that the presence of O vacancies sustains the reaction rate at long reaction times.

Ultimately, this thesis verifies that O vacancies on $CeO_2(111)$ have a strong effect on adsorption processes, by increasing the binding strength of adsorbates and opening up new adsorption pathways. This is especially important in the interaction with H_2, where the presence of O vacancies below the surface enables the formation of hydrides. We believe that our work makes a significant contribution to a more fundamental understanding of $CeO_2(111)$ catalysis and hope that it will inspire future investigations.

Zusammenfassung

Ceroxid (CeO_2) wurde in den letzten Jahren als Katalysator für die Hydrierung von Alkinen zu Alkenen entdeckt und hat als solcher großes wissenschaftliches Interesse geweckt. Um weitere Einblicke in die Funktion von CeO_2 in der Reaktion zu gewinnen, beschäftigt sich diese Arbeit mit der Adsorption von H_2, CO_2 und Propin, sowie mit der Interaktion von Hydroxylgruppen und Propin auf CeO_2(111)-Oberflächen. Ein besonderer Fokus liegt dabei auf der Rolle von Sauerstoffleerstellen.

Die Dissoziation von H_2 auf CeO_2(111) ist ein aktivierter Prozess und findet bei erhöhten Drücken und Temperaturen statt. Sie führt zur Bildung von Hydroxylgruppen und zur Reduktion der Oberfläche. Die Anwesenheit von Sauerstofleerstellen unter der Oberfläche ermöglicht außerdem die Bildung von Hydridspezies. Dieser Prozess führt über einen Elektronentransfer von Ce^{3+} zu Wasserstoffspezies zu einer Re-oxidierung. Wenn CeO_2 bei höheren Temperaturen H_2 ausgesetzt wird, werden auch in Anwesenheit von Sauerstoffleerstellen bevorzugt Hydroxylgruppen gebildet.

CO_2, das bei katalytischen Reaktionen oft als Verunreinigung zugegen ist, chemisorbiert auf CeO_2(111) wahrscheinlich als Karbonat und ist bis zu 270 K stabil. Die Interaktion mit Sauerstoffleerstellen stabilisiert adsorbierte CO_2-Spezies zusätzlich.

Auch in der Adsorption von Alkinen auf CeO_2(111) spielen Sauerstoffleerstellen eine tragende Rolle. Während Propin nur schwach mit der perfekten CeO_2(111)-Oberfläche wechselwirkt, stabilisiert die Anwesenheit von Sauerstoffleerstellen adsorbierte Alkinspezies erheblich. H_2 und Propin interagieren nur schwach auf der Oxidoberfläche. Die zuvor ausgewiesene hohe Aktivität von CeO_2 in der Hydrierungsreaktion konnte in unseren Modelexperimenten nicht nachvollzogen werden. Es scheint allerdings, dass die Anwesenheit von Sauerstoffleerstellen die Reaktionsrate bei langen Reaktionszeiten fördert.

Letztlich zeigt die vorliegende Arbeit, dass Sauerstoffleerstellen einen starken Einfluss auf Adsorptionsprozesse auf CeO_2(111) ausüben. Dies geschieht einserseits durch eine verstärkte Interaktion mit Adsorbaten und andererseits durch die Eröffnung neuer Reaktionswege, wie beispielsweise der Bildung von Hydridspezies. Wir glauben, dass die vorliegende Arbeit einen wesentlichen Beitrag zum Verständnis fundamentaler Prozesse auf der CeO_2(111)-Oberfläche liefert und Anregung für zukünftige Reaktivitätsstudien bietet.

Table of Contents

1 Introduction

1.1 Heterogeneous Catalysis

Catalytic processes shape our world. 90% of all industrial products are manufactured with the help of a catalyst.[1, 2] Some products, like synthetic fibers, a large number of plastics, pharmaceuticals, resins, and dyes, could not be fabricated without catalysis. Today, the most important catalytic applications lie within the fields of emission control, petrochemistry, energy conversion, and the production of fine and base chemicals. Of the latter, alone the production of ammonia (NH_3) from N_2 and H_2 in the so-called *Haber-Bosch Process* is so essential to our way of living that it employs 1% of the world's energy supply.[3]

Catalysts are chemical agents that accelerate a reaction by lowering its overall activation barrier. Apart from the decreased demand in activation energy, a catalyst provides several other advantages. With catalysts, a higher selectivity for a specific chemical product is achievable, and the output of undesired reaction byproducts can be minimized. More than that, catalysis provides a way to highly tune the desired reaction product towards a specific stereochemistry.

80% of the catalytic processes we use industrially are so-called *heterogeneous* catalytic processes, while 15% fall to homogeneous catalysis, and 5% to biocatalysis (i.e. processes involving enzymes).[1] Homogeneous catalysis takes place in a uniform phase (gaseous or liquid). Heterogeneous catalysis, on the other hand, involves several phases. Typically, a heterogeneous catalyst is solid and interacts with reactants in gas or liquid phase via its *surface*.

An exemplary energy diagram of a heterogeneously catalyzed reaction is shown in Fig. 1.1. Here, a direct reaction of reactant A to product B involves a high activation energy $E_{a,0}$. In presence of a catalyst, A first adsorbs on the catalyst surface as an adsorbate A*. The reaction then proceeds through a surface transition state to the adsorbed species B*, which finally desorbs as product B. Though the reaction A*$\rightarrow$B* still requires a certain amount of activation energy ($E_{a,1}$), the overall activation energy $E_{a,2}$ is considerably lower than for the non-catalyzed reaction. In consequence, the reaction on the catalyst will proceed with a higher reaction rate.

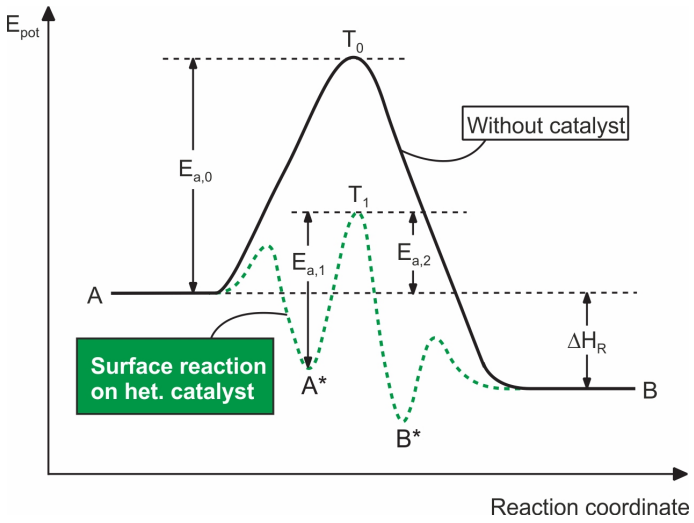

Fig. 1.1: Energy diagram of a reaction A→B without and with heterogeneous catalyst. ΔH_R is the overall reaction enthalpy. $E_{a,0}$ and T_0 are the activation energy and the transition state energy, respectively, of the non-catalyzed reaction. $E_{a,1}$ and $E_{a,2}$ are the actual and apparent activation energy of the catalyzed reaction. T_1 is the transition state energy on the catalyst surface. Adapted from [1].

Since a heterogeneous catalyst interacts with reactants, intermediates and products at its surface, the catalyst's performance is defined not only through the energetics of the chemical reaction itself, but also through the efficiency of surface processes, such as adsorption of the reactants, diffusion to and from catalytically active sites, and desorption of the products. In heterogeneous catalysis, particularly the bond strength of adsorbates on the catalyst surface is a crucial factor. Following the *principle of Sabatier*, a good heterogeneous catalyst should bind reactants, intermediates and products neither too weak nor too strongly. If the binding energy is weak, adsorbates will fail to bind to the catalyst, which results in low catalytic activity. Too strong adsorption, on the other hand, leads to excessive blocking of the catalyst's active sites - which also results in low activity. Besides a high activity under the considered reaction conditions, desirable catalyst features are high selectivity for a specified reaction product, a stable performance over long periods of time, recyclability, and abundance of the catalyst's constituent chemical elements.

1.2 The Surface Science Approach to Heterogeneous Catalysis

Heterogeneous catalysts, as they are used in industrial processes, are highly complex, multi-component, and non-uniform systems. Typically, their active phase are metal nanoparticles, which are supported on a high surface area material, often an oxide. The activity of an industrial catalyst depends strongly on the particle size, the type of exposed metal surface facets, the metal's interaction with the support and the presence of structural defects. To illustrate the complexity of these systems, Fig. 1.2a shows a Transmission Electron Microscopy (TEM) image of a typical heterogeneous hydrogenation catalyst.

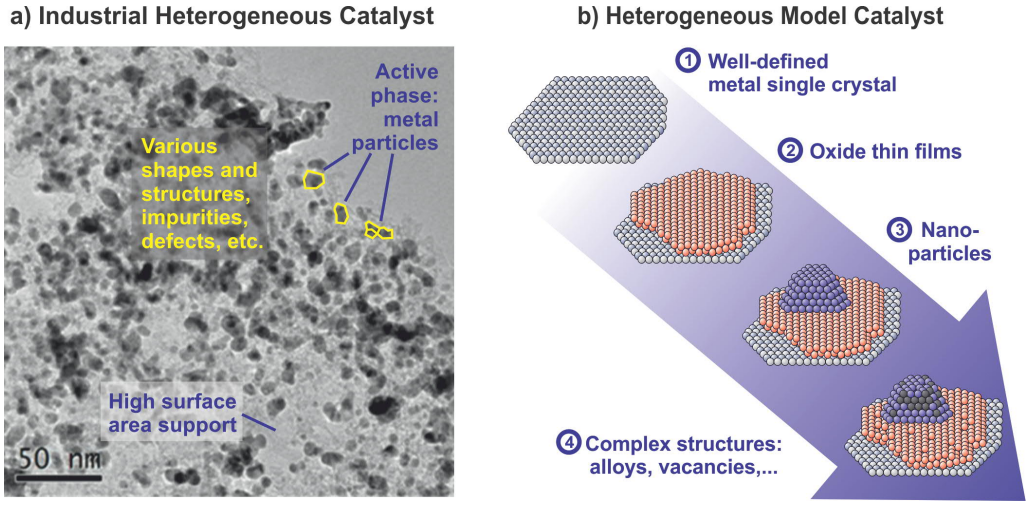

Fig. 1.2: a) TEM image of a heterogeneous Pd/C catalyst for hydrogenation reaction (adapted from [4]), b) schematic overview of complexity levels in model catalysts used in surface science (adapted from [5]).

To intelligently design heterogeneous catalysts, it is essential to understand the fundamental processes of adsorption, reaction, and desorption. These processes will be widely governed by the composition and structure of the catalyst surface. Since industrial catalysts are highly complex systems, it is hardly possible to investigate the relation of their structural features to their catalytic performance. For this reason, the *surface science approach* to heterogeneous catalysis consists in the investigation of *model catalysts*.

Model catalysts are well-defined systems of known composition and structure. The most simple types of model catalysts are metal single crystals with highly uniform surfaces. In ultra-high vacuum (UHV) environments, reactants may be offered to

the catalyst in controlled amounts and their interaction with the surface investigated by a vast number of spectroscopic and imaging methods. In a bottom-up approach, the complexity of model catalysts may be increased by stepwise alterations, in order to reconstruct the multi-component system of an industrial catalyst. As such, crystalline oxide films may be grown on top of the metal single crystal, nanoparticles of known size and composition may be added, and finally, complex defects may be introduced. A schematic illustration of this approach is shown in Fig. 1.2b. The aim of surface science is to resolve the properties of adsorbates and the mechanisms of catalytic reactions, and to link these to the physical and electronic properties of the catalyst surface. Theoretical modeling, in addition, serves as a tool to compute (among others) adsorbate geometries, bond strengths, reaction pathways, and activation energy barriers. The combination of experimental and theoretical model studies provides fundamental insights into catalytic processes.

To apply the understanding of model catalysts to realistic systems, it is important to overcome the so-called materials and pressure gaps. The *materials gap* addresses the differences in structure between model catalysts and industrial catalysts. These may be overcome by efforts to include complex structural features, such as morphological defects, into ideal model systems. Furthermore, an effort is made to apply surface science methods to micro-crystalline catalysts, such as oxide nanoparticles of well-known termination. The *pressure gap*, on the other hand, constitutes the difference between the UHV environment of most model catalyst studies and the high pressure conditions of industrial catalysis. Efforts to overcome the pressure gap include the combination of high-pressure reaction and vacuum characterization, as well as spectroscopic measurements under elevated pressure.

The systematic investigation of metal oxides plays an essential role in surface science. Oxides are vastly used in industrial catalysis as supporting materials and as stand-alone catalysts. Efforts in surface science during the last three decades opened up new possibilities in the preparation and characterization of well-defined metal oxide films. Up to today, however, they are less extensively studied than metal single crystals, since they exhibit a largely increased level of complexity. Especially the presence of defects, such as oxygen vacancies, widely determines their interplay with adsorbates. Achieving a fundamental understanding of the adsorption, reaction, and desorption processes on metal oxide surfaces will enhance our understanding of catalysis and enable us to design smarter catalytic systems.

1.3 Catalytic Application and Properties of CeO_2

1.3.1 Application in Catalysis

Due to its unique redox and structural properties, ceria (CeO_2) is an often-employed supporting material in various catalytic applications. Especially the oxide's oxygen storage-and-release capacity, i.e. its ability to easily release O atoms without changing its lattice parameters, makes CeO_2 an outstanding supporting material in many reactions. The presence of O vacancies on the CeO_2 surface is thereby known to largely influence the oxide's reactivity.[6–10]

As a supporting material for Pt, Rh, or Pd particles, CeO_2 is employed most prominently in the three-way automotive catalyst.[6, 7] Other applications of CeO_2 include steam reforming of hydrocarbons, the low temperature water-gas shift reaction, the preferential oxidation of CO in H_2-rich streams, the hydrogenation of various functional groups, and the dehydrogenation of alcohols.[6–10] As a stand-alone catalyst, CeO_2 is used in the oxidation of volatile organic compounds.[10]

Only recently, CeO_2 has been reported as a catalyst in the selective hydrogenation of alkynes to alkenes with remarkable activity and selectivity.[11–16] Vilé and coworkers, the authors of these first studies, reported an increased activity of the $CeO_2(111)$ surface as opposed to other CeO_2 facets, and identified the dissociation of H_2 as the rate-limiting step in the hydrogenation reaction.[11, 14] Furthermore, they attribute a decrease in alkene selectivity at high temperatures (see Fig. 1.3) to an increased oxygen vacancy density on the oxide surface.

1.4 $CeO_2(111)$ and $CeO_{2-x}(111)$ Surfaces

1.4.1 Cerium Oxide Bulk Phases

Ceria exists in a variety of stable stoichiometries, of which the fully oxidized phase is CeO_2. CeO_2 adopts a fluorite (CaF_2) structure with space group *Fm3m* (a=0.541 nm), in which Ce^{4+} ions are arranged in a face-centered cubic (FCC) lattice. O^{2-} ions are ordered in a cubic arrangement, such that that each O^{2-} ion is tetrahedrally coordinated to four nearest neighbor Ce^{4+} ions. Each Ce^{4+} ion is coordinated to eight equivalent O^{2-} ions (see Fig. 1.4).

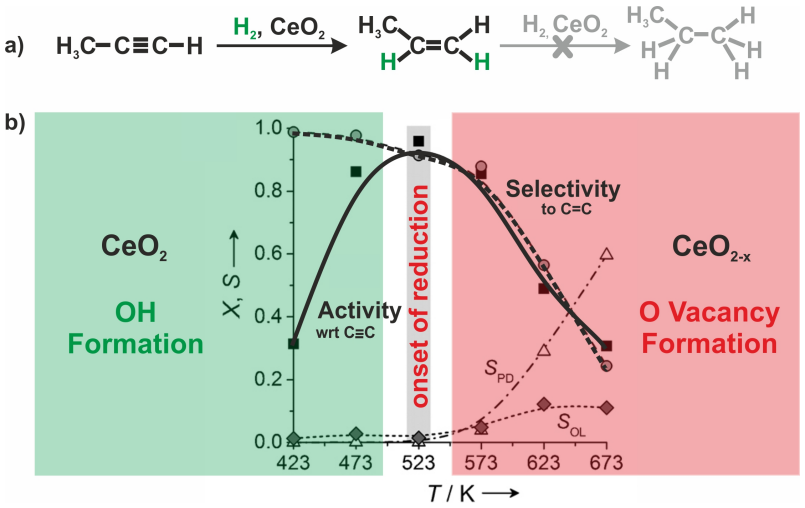

Fig. 1.3: Selective hydrogenation of alkynes to alkenes over CeO_2 powders: a) reaction equation, b) activity and selectivity as a function of reaction temperature. Adapted with permission from [11].

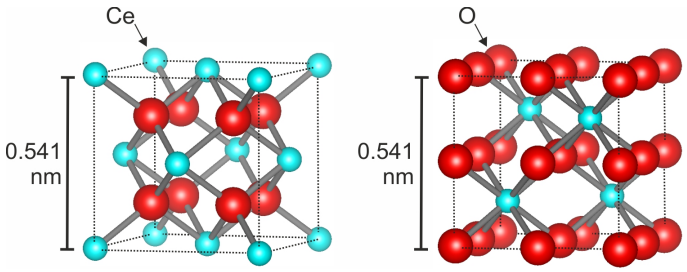

Fig. 1.4: CeO_2 unit cell in two alternative representations.

The release of O atoms from the lattice (at high temperature and low O_2 pressure) generates vacant positions (□), also called *oxygen (O) vacancies*. In the course of O vacancy formation, two Ce^{4+} ions are reduced to Ce^{3+}.[17–21]

$$2\,Ce^{4+} + O^{2-} \longrightarrow 2\,Ce^{3+} + \square + 0.5\,O_2 \tag{1.1}$$

Removal of O leads to reduced oxide phases of often complex stoichiometry. Intermediate stoichiometries of CeO_{2-x} with $0.5<x<0$ have a bulk structure based on the fluorite lattice, where Ce ions stay close to their FCC positions. Periodical partially reduced phases are $Ce_{11}O_{20}$ (triclinic, $P\bar{1}$) and Ce_7O_{12} (trigonal, $R\bar{3}$). Furthermore, a Ce_3O_5 bulk phase has been proposed, but not yet experimentally observed.[22] The fully reduced C-Ce_2O_3 bixbyite phase is formed when 25% of O atoms are removed from the fluorite lattice. Another, structurally non-related, Ce_2O_3 phase crystallizes in hexagonal structure (space group $P\bar{3}ml$), and is slightly more stable than C-Ce_2O_3.[6, 17, 23]

1.4.2 Structures of $CeO_2(111)$ and $CeO_{2-x}(111)$

The low-index facets of CeO_2 are its (111), (110), and (100) terminations. Their stability decreases in the order of (111)>(110)>(100) due to charging effects.[9] The formation energy of O vacancies on the surfaces decreases in the order of (111)>(100)>(110), making $CeO_2(111)$ the least prone to release O.[24] Since this thesis is centered around the surface chemistry of $CeO_2(111)$, we consider its structure in the following.

$CeO_2(111)$ (see Fig. 1.5) is a Tasker type 2 surface, consisting of O-Ce-O trilayers (3.1 Å in height) which repeat in [111] direction. Each atomic layer is charged, but since charges are balanced within the trilayer, no net dipole moment results perpendicular to the surface. The $CeO_2(111)$ surface is terminated by O^{2-} ions and resembles bulk truncation, with a slight contraction between the first and second atomic layer to minimize the surface energy. Since the O-O distance is quite large in the topmost layer (3.8 Å), Ce^{4+} ions in the layer below may react with molecules on the surface.[9] The majority of studies on $CeO_2(111)$ has been carried out on thin films that are grown epitaxially on single crystal substrates, such as Si(111), Pt(111), Cu(111), and Ru(0001).[9, 17]

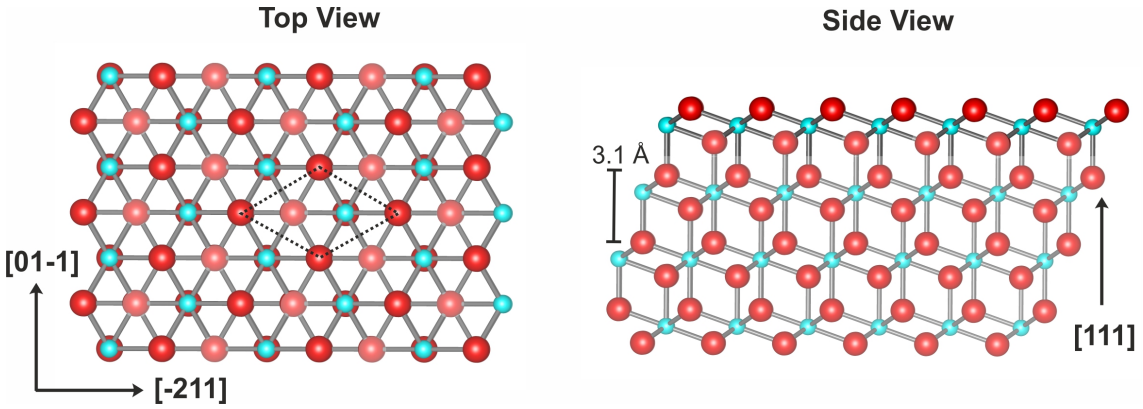

Fig. 1.5: Schematic representation of the $CeO_2(111)$ surface. Ce^{4+} (blue) and O^{2-} ions (red) are drawn with their ionic radii. O^{2-} ions below the topmost layer are shown in lighter color for clarity.

Reduced $CeO_{2-x}(111)$ surfaces are prepared from $CeO_2(111)$ by various methods, including Ar^+ sputtering,[25, 26] reduction by H_2,[25, 27] high temperature annealing in UHV,[23, 28–31] and thermal incorporation of metallic Ce.[32–34] Alternatively, a reduced thin film may be formed by reactive deposition of Ce in low O_2 pressure.[35, 36]

The location and structure of O vacancies on $CeO_2(111)$ has been extensively studied. O vacancies form easier on the $CeO_2(111)$ surface than in the CeO_2 bulk.[33, 37–39] Upon release of an O atom, the left-behind electrons localize on two Ce^{4+} ions within the surface, reducing them to Ce^{3+}.[38, 40–43] Microscopic and DFT+U studies showed that multiple configurations of energetically similar structures are possible, where the Ce^{3+} ions occupy different lattice positions. Thereby, at least one, possibly both Ce^{3+} ions are not in direct vicinity to the vacant O site.[41, 42, 44–46]
The creation of O vacancies results in lattice distortions.[41, 46, 47] O^{2-} ions next to the vacant O site move slightly upward from their lattice positions, away from Ce ions, and form O^{2-} ion pairs on the surface. These relaxations are justified by lattice strain, resulting from the larger radius of the Ce^{3+} ion with respect to Ce^{4+}.[38] Furthermore, space charge stress induces distortion, when O vacancies form predominantly in a narrow layer.[48]

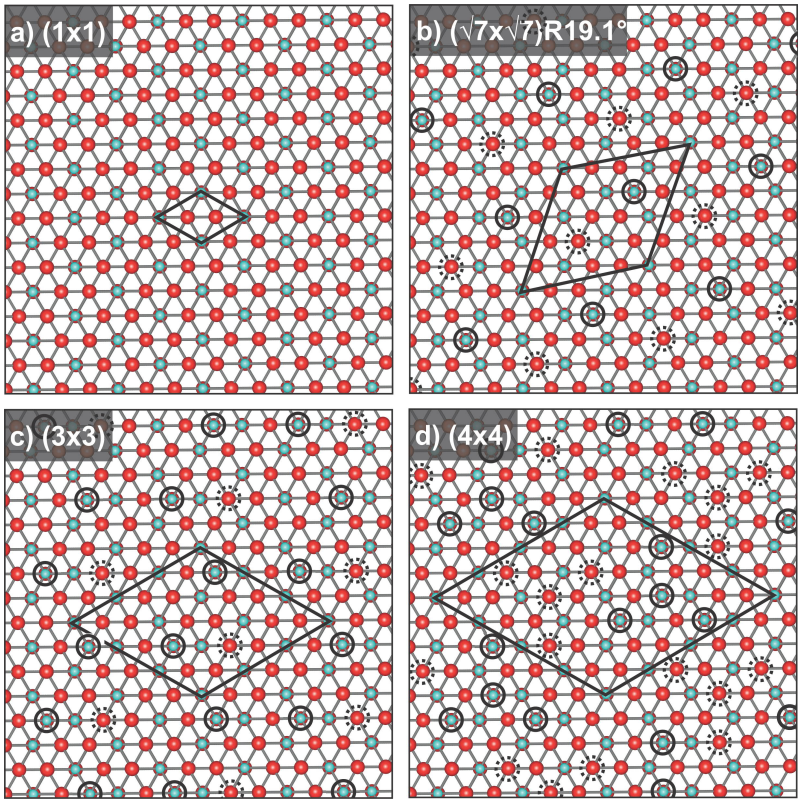

Fig. 1.6: Schematic representation (top view) of experimentally observed, ordered $CeO_{2-x}(111)$ surfaces derived from (a) $CeO_2(111)$:
b) $(\sqrt{7}\times\sqrt{7})$R19.1°-reconstruction, c) (3×3)-reconstruction, d) (4×4) reconstruction. O ions are shown in red, Ce ions (of both reduction states) in blue. Full circles represent O vacancies in the topmost, dashed circles in the second O layer. Adapted from [33].

At low temperature, isolated O vacancies form in the surface and subsurface (2nd O layer) of CeO_2(111). Isolated O vacancies are most stable in the subsurface, where they may reconstruct into periodic (2x2) arrays.[22, 44, 45, 47] At higher temperature, O vacancies agglomerate into linear and triangular surface clusters.[41, 42, 49–52] O vacancy clusters may also be formed by agglomeration of surface and subsurface vacancies.[43]

The formation energy of O vacancies increases with increasing O vacancy density.[38] At high degrees of reduction and elevated temperature, O vacancies may reconstruct into ordered arrays. A variety of CeO_{2-x}(111) surfaces with long-range ordered O vacancy structures has been identified and correlated with metastable CeO_{2-x} phases.[22, 23, 33] Fig. 1.6 shows a schematic representation of experimentally observed ordered CeO_{2-x}(111) surfaces. An overview of CeO_{2-x}(111) surface structures is given in Table 1.1.

1.5 Aims and Structure of This Work

The aims of this thesis has been to investigate the interaction of H_2, CO_2, and propyne with the CeO_2(111) surface, in order to gain further insights into adsorption processes and the selective hydrogenation reaction over CeO_2. A special emphasis thereby lies in the influence of oxygen vacancies. To elucidate the latter, we have performed comparative adsorption and reactivity experiments on stoichiometric CeO_2(111) and oxygen vacancy-containing, reduced CeO_{2-x}(111) thin films.

Chapter 2 provides basic insights into the applied experimental techniques and describes the experimental setups. Furthermore, it summarizes the preparation and characteristics of the CeO_2(111) and CeO_{2-x}(111) thin films. Chapters 3 and 4 present new insights into the interaction of CeO_2(111) with atomic and molecular hydrogen. Chapter 5 explores the adsorption of CO_2 and its thermal stability on the oxide surface. Chapter 6, finally, presents new insights into the adsorption of propyne on CeO_2(111), and investigates the oxide surfaces' activity in the selective hydrogenation reaction.

Stoichiometry	Periodicity wrt. $CeO_2(111)$	Bulk Phase	Reference (Substrate, Identification Technique)
CeO_2	(1×1)	CeO_2	Various Authors
$CeO_{1.81}$	$(\sqrt{7} \times \sqrt{13})$	$Ce_{11}O_{20}$	Predicted,[22] but not yet observed
$CeO_{1.81}$	$(\sqrt{3} \times \sqrt{31})$	$Ce_{11}O_{20}$	Predicted,[22] but not yet observed
$CeO_{1.75}$	(2×2)	Unknown	Reichling et al.[23, 47] (Bulk-like, AFM)
$CeO_{1.71}$	$(\sqrt{7} \times \sqrt{7})$R19.1°	Ce_7O_{12}	Wollschläger et al.[30] (Si(111), LEED)
			Matolin et al.[33] (Cu(111), LEED)
			Matolin et al.[34] (Ru(0001), LEED)
			Thornton et al.[53] (Pt(111), LEED)
			Reichling et al.[23] (Bulk-like, AFM)
$CeO_{1.71}$	$(\sqrt{3} \times \sqrt{13})$	Ce_7O_{12}	Predicted,[22] but not yet observed
$CeO_{1.67}$	$(\sqrt{3} \times \sqrt{3})$R30°	Ce_3O_5	Reichling et al.[23] (Bulk-like, AFM)
$CeO_{1.67}$	$(\sqrt{7} \times 3)$R19.1°	Ce_3O_5	Reichling et al.[23] (Bulk-like, AFM)
$CeO_{1.67}$	(3×3)	Ce_3O_5	Matolin et al.[33] (Cu(111), LEED)
			Matolin et al.[34] (Ru(0001), LEED)
$CeO_{1.5}$	(4×4)	C-Ce_2O_3	Carbone et al.[32] (W(110), LEED)
		(bixbyite,	Netzer et al.[54] (Rh(111), LEED)
		cubic)	Wang et al.[28] (Re(0001), LEED)
			Flege et al.[55] (Si(111), LEED)
			Matolin et al.[33, 56] (Cu(111), LEED)
			Matolin et al.[34] (Ru(0001), LEED)
$CeO_{1.5}$	$\sim(1\times1)$	A-Ce_2O_3	Schierbaum et al.[29] (Pt(111), STM)
	$Ce_2O_3(0001)$	(hexagonal)	Reichling et al.[23] (Bulk-like, AFM)
			Flege et al.[31]
			(NP/Ru(0001), LEED/LEEM)

Table 1.1: Experimentally observed and postulated structures of periodic $CeO_{2-x}(111)$ surfaces, ordered from most oxidized (CeO_2) to most reduced ($CeO_{1.5}$).

2 Theoretical Background and Experimental Methods

This chapter describes (i) the basic concepts of the experimental methods applied in this work, (ii) the experimental setups, and (iii) the growth procedure and characteristics of the $CeO_2(111)$ and $CeO_{2-x}(111)$ thin films.

2.1 The Need for Ultrahigh Vacuum

To investigate surfaces on an atomic level, it is essential that their composition stays unchanged over the time of the experiment. Therefore, the adsorption of gases from the background onto the sample surface should be minimal. The incident flux I of residual gas molecules onto the surface is given by the *Hertz-Knudsen equation*:

$$I = \frac{dN}{Adt} = \frac{p}{\sqrt{2\pi m k_B T}} \tag{2.1}$$

where N is the number of impinging gas species, A is the surface area, t is the time, p is the residual gas pressure, m is the mass of the impinging species, k_B is Boltzmann's constant, and T is the temperature.

Metal surfaces comprise approximately 10^{15} atoms per cm^2.[57] In an ambient environment (10^5 Pa (1 bar) N_2-like molecules, 300 K), assuming that every N_2 molecule sticks on top of a metal atom, the metal surface would be entirely covered after only 3.4 ns. Experiments, however, last between several minutes and several hours. As a consequence, surface science experiments are typically performed in ultra-high vacuum (UHV), thus at pressures below 10^{-7} Pa (10^{-9} mbar).

Furthermore, low pressure is essential for all preparation and characterization methods that involve free-flying particles. This is the case, for example, when a sample is characterized by low energy electrons. To ensure an even energy distribution among the particles, and thereby good quality of the resulting data, it is crucial that they do not suffer collisions with other particles. The average distance that a gas particle travels in between collisions is defined as the mean free path λ:

$$\lambda = \frac{k_B T}{\sqrt{2}\sigma p} \tag{2.2}$$

where σ is the molecular cross section (e.g. 0.43 nm^2 for N_2). Since λ is reciprocally proportional to the residual gas pressure, particles are able to travel longer distances unperturbed at lower pressures. At 300 K, pressures below 10^{-3} Pa (10^{-5} mbar) ensure a mean free path of several meters.

2.2 Experimental Techniques

2.2.1 Low Energy Electron Diffraction (LEED)

Low Energy Electron Diffraction (LEED) is a standard technique to analyze the long-range structure of well-ordered solid surfaces. In LEED, the sample is exposed to low energy electrons, which are diffracted by the surface's periodic Coulomb potential. The diffracted electrons are projected onto a luminescent screen, where they produce *diffraction spots* as a result of interference. The position, profile and intensity of these diffraction spots allow insights into the surface's structural arrangement. LEED analysis requires a conductive sample and a UHV environment.

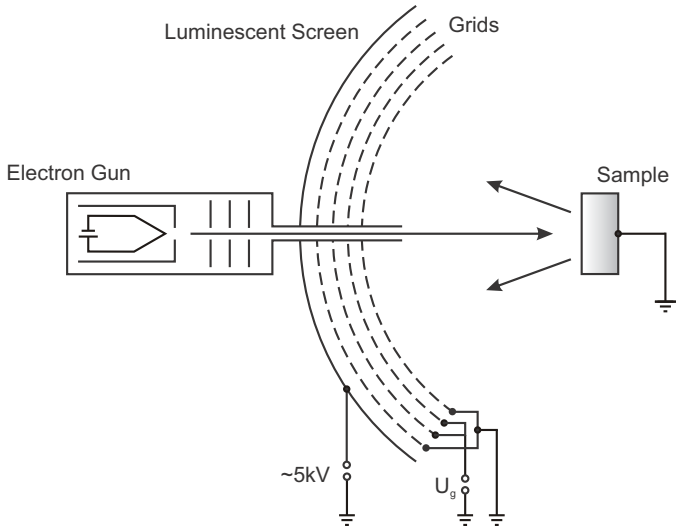

Fig. 2.1: Schematic representation of a typical LEED setup.

A typical LEED setup (see Fig. 2.1) consists of an electron gun, a hemispherical luminescent screen, and a set of hemispherical grids, which are concentrically arranged between the screen and the sample. Electrons are emitted by a thermionic cathode in the electron gun. They are focussed by a Wehnelt cylinder and a set of electrostatic lenses, so that a collimated, mono-energetic electron beam is generated. When the electron beam hits the sample surface, the surface's periodic Coulomb potential scatters the beam and the back-scattered electrons interfere. In conventional setups,

the electron beam is focused onto a sample surface area of approximately 1 mm^2. The back-scattered electrons travel towards the luminescent screen in a field-free space between the grounded sample and the grounded innermost grid. Further grids with applied retarding voltages ensure that only elastically scattered electrons pass. The diffraction electrons are finally re-accelerated between a grounded grid and the luminescent screen, on which they produce diffraction spots.

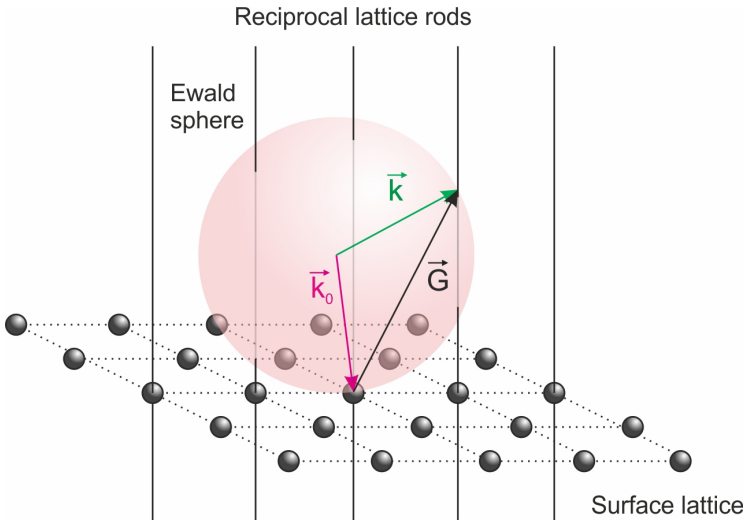

Fig. 2.2: Ewald sphere on a surface lattice (represented in reciprocal space).

Distinctive diffraction spots appear in case of constructive interference of the back-scattered electron waves, i.e. if the *Laue condition* is met:

$$\vec{k} - \vec{k_0} = \vec{G} \tag{2.3}$$

where $\vec{k_0}$ is the incident wave vector, $\vec{k}$ is the back-scattered wave vector and $\vec{G}$ is the reciprocal wave vector. $|\vec{k}| = |\vec{k_0}|$ since only elastically scattered electrons pass to the screen. This condition is commonly represented by the construction of the so-called *Ewald sphere* with radius $|\vec{k_0}|$, and $\vec{k_0}$ pointing towards the origin of the reciprocal lattice. In a three-dimensional system, the Laue condition is fulfilled when the Ewald sphere intersects with a reciprocal lattice point. A surface lattice can be thought of as a three-dimensional lattice with infinitely large lattice spacing in direction normal to the surface. In consequence, the reciprocal lattice points in this direction become reciprocal lattice rods. A diffraction spot appears when the Ewald sphere intersects with such a reciprocal rod (see Fig. 2.2). For a surface lattice, the surface-parallel component of $\vec{G}$ corresponds to the surface's reciprocal lattice vector. The arrangement of detected diffraction spots on the luminescent screen will finally represent the surface's reciprocal lattice.

The electron energy is chosen such that the electron wavelength is in the order of the surface's inter-atomic distances, since this allows optimal resolution of the diffraction pattern. Typically, energies in the range between 20 and 200 eV are applied. The electrons' low energy results in a short inelastic mean free path of the electrons in the sample, so that only diffraction from layers close to the surface will contribute to the LEED signal.

The profile of the diffraction spots is a measure for the degree of order on the surface. The spots appear bright and sharp only if the surface is atomically well-ordered on a long-range scale. Impurities and structural defects broaden the spots and result in an increased background intensity.

2.2.2 Infrared Reflection Absorption Spectroscopy (IRAS)

Infrared Reflection Absorption Spectroscopy (IRAS) is a powerful tool in surface science to characterize adsorbates on surfaces. The technique is based on the reflection of infrared (IR) light from a surface, which yields a vibrational spectrum of surface adsorbates. IRAS may provide insights into

1. chemical state, structure, and orientation of isolated adsorbates,

2. adsorbate-substrate interactions, e.g. charge transfer, preferred adsorption sites, and order-disorder phenomena,

3. adsorbate-adsorbate interactions, e.g. dipole-dipole interactions, structural information on the adsorbate layer, and phenomena of ad-layer growth, and

4. qualitative changes in bonding and reactivity between adsorbates.

The practical strengths of IRAS in comparison to other vibrational spectroscopies lie in the high resolution of spectra (1-5 cm^{-1}) and in the technique's high sensitivity, which allows to examine adsorbates in very small densities (down to 0.1% of a monolayer for strong dipole absorbers).[58] Moreover, IRAS is a highly versatile technique. It allows measurements over a wide range of temperatures and pressures, and may be combined conveniently with a variety of other measuring techniques. The practical weaknesses of IRAS lie mostly in its restricted spectral range (typically 4000-800 cm^{-1}), which does not allow to directly probe most adsorbate-substrate bonds. Moreover, only highly reflecting samples may be used, which are typically single crystal metals (with or without thin films of non-reflecting material on top).

Working Principle and Instrumentation

A typical IRAS setup is shown schematically in Fig. 2.3. Multiple mirrors direct the IR light from a source to the sample in a grazing angle of incidence. On the sample surface, adsorbates are vibrationally excited by a fraction of the IR light. The sample acts as a mirror and reflects the remainder of the IR light towards a detector.

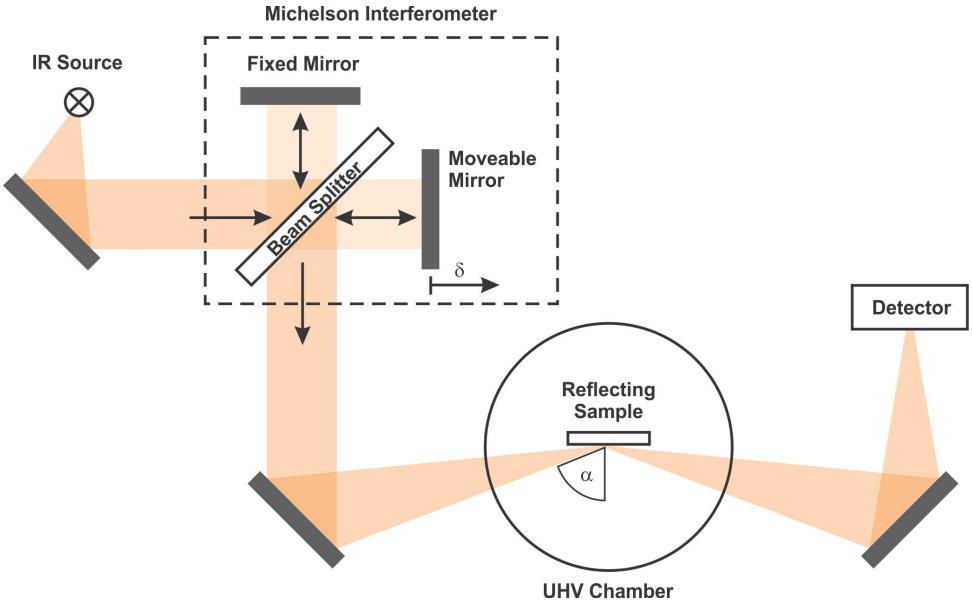

Fig. 2.3: Schematic representation of a typical IRAS setup.

Typical IR sources emit polychromatic IR light. Formerly, this IR light was divided into its spectral components, and the absorption measured for each frequency individually. Nowadays, Fourier Transform Infrared (FTIR) spectrometers have become the instrumentation of choice, since they allow to probe the sample with all spectral components simultaneously. This results in a significantly shorter scanning time and an improved signal-to-noise ratio.

At the heart of any FTIR spectrometer is a Michelson interferometer. In the interferomter, the polychromatic IR light is divided into two beams on a beam splitter. One of the beams is reflected from a fixed mirror, the other from a moveable mirror that allows to introduce a variable distance δ into the path length. When the two beams are recombined after reflection from the mirrors, interference occurs. This interference changes the intensity of each spectral component individually as a function of the path difference δ and its individual wavenumber $\tilde{\nu}$. The modulated part of the intensity, $I(\delta)$, for a single spectral component may be expressed as:[59]

$$I(\delta) \propto I_0(\tilde{\nu}) cos(2\pi\tilde{\nu}\delta) \tag{2.4}$$

where $I_0(\tilde{\nu})$ is the original intensity of the IR light with wavenumber $\tilde{\nu}$.
In practice, the intensity is further modified by instrument-specific parameters, i.e. the beam splitter efficiency, the detector response, and amplifier characteristics. The IR intensity arriving at the detector may be expressed by the parameter $B(\tilde{\nu})$, which includes the original intensity before modulation and its instrumental modifications. The detector measures a potential $S(\delta)$, which is obtained from $B(\tilde{\nu})$ by interference modulation:

$$S(\delta) = B(\tilde{\nu})cos(2\pi\tilde{\nu}\delta) \tag{2.5}$$

Since the IR beam consists of multiple spectral components with different wavenumbers $\tilde{\nu}$, the total detector signal, the so-called *interferogram*, is expressed as an integral:

$$S(\delta) = \int_{-\infty}^{\infty} B(\tilde{\nu})cos(2\pi\tilde{\nu}\delta)d\tilde{\nu} \tag{2.6}$$

The interferogram can be Fourier-transformed to give the intensity response $B(\tilde{\nu})$ for each individual spectral component.

$$B(\tilde{\nu}) = \int_{-\infty}^{\infty} S(\delta)cos(2\pi\tilde{\nu}\delta)d\delta \tag{2.7}$$

To obtain an ideal spectrum, it would be necessary to vary the beam path difference δ up to infinity. In practice, δ can only be varied up to a finite value, which will result in an IR reflectance spectrum of finite resolution. To compensate for this, the interferogram is convolved with a sinc function, also called the *instrument line shape function*. Furthermore, the interferogram will be modified by apodization to suppress artifacts and by the introduction of a wavenumber-dependent phase factor to correct for asymmetry. For further details on IRAS instrumentation and FTIR processing, please see refs. [59] and [60].

The resulting reflectance spectrum will show IR absorption features of adsorbates on the surface, but will also include features of considerable intensity that are caused by absorption in the optical beam path. To correct for these, the spectrum is divided by a reference spectrum measured with the same optical setup, but without adsorbates present on the sample. The background-corrected absorbance is finally obtained as:

$$A(\tilde{\nu}) = \frac{R_0(\tilde{\nu}) - R(\tilde{\nu})}{R_0(\tilde{\nu})} = \frac{\Delta R}{R} \tag{2.8}$$

where $A(\tilde{\nu})$ is the absorbance as a function of the wavenumber $\tilde{\nu}$, $R_0(\tilde{\nu}) - R(\tilde{\nu})$ is the signal intensity in the reflectance spectrum obtained with adsorbates on the surface and $R_0(\tilde{\nu})$ is the signal intensity of the reference spectrum of the clean sample.

Selection Rules

As can be derived by time-dependent perturbation theory,[58, 61, 62] the transition probability $P_{i\to f}$ from the ground state Ψ_i to the vibrationally excited state Ψ_f of a diatomic molecule is given according to Fermi's Golden Rule:

$$P_{i\to f} \propto |M_{i\to f}|^2 \tag{2.9}$$

where $M_{i\to f}$ is the transition dipole moment:

$$M_{i\to f} = \langle \Psi_f(Q_k)| \, \vec{\mu}(Q_k) \, |\Psi_i(Q_k)\rangle \tag{2.10}$$

with $\vec{\mu}(Q_k)$ being the dipole moment of the molecule as a function of the normal coordinate Q_k of the vibration, i.e. the displacement of the nuclei from their equilibrium position. The wave functions Ψ_i and Ψ_f can be further factorized into an electronic contribution ϵ and a nuclear contribution χ when applying the *Born-Oppenheimer approximation*. The transition dipole moment then changes to:

$$M_{\epsilon,\chi\to\epsilon',\chi'} = \langle \epsilon', \chi'| \, \vec{\mu}(Q_k) \, |\epsilon, \chi\rangle \tag{2.11}$$

where ϵ and χ are the electronic and nuclear contributions to the initial state, and ϵ' and χ' are the electronic and nuclear contributions to the final state, respectively. Since we are only interested in purely vibrational excitation (where the electronic state is not changed, i.e. $\epsilon = \epsilon'$), the transition dipole moment simplifies to

$$M_{\chi\to\chi'} = \langle \chi'| \, \vec{\mu}(Q_k) \, |\chi\rangle \tag{2.12}$$

where $\vec{\mu}$ is the dipole moment operator of the molecule in its electronic state ϵ.

We can express the variation of $\vec{\mu}$ as a function of Q_k (i.e. as a function of the displacement of the nuclei from their equilibrium position) in a Taylor expansion:

$$\vec{\mu} = \vec{\mu}_0 + \left(\frac{d\vec{\mu}}{dQ_k}\right) Q_k + \frac{1}{2}\left(\frac{d^2\vec{\mu}}{dQ_k}\right) {Q_k}^2 + \cdots \tag{2.13}$$

where $\vec{\mu}_0$ is the dipole moment when the displacement is zero.
The transition dipole moment then becomes

$$M_{\chi\to\chi'} = \langle \chi'| \, \vec{\mu} \, |\chi\rangle = \vec{\mu}_0 \, \langle \chi'|\chi\rangle + \left(\frac{d\vec{\mu}}{dQ_k}\right) \langle \chi'| \, Q_k \, |\chi\rangle + \frac{1}{2}\left(\frac{d^2\vec{\mu}}{{dQ_k}^2}\right) \langle \chi'| \, {Q_k}^2 \, |\chi\rangle + \cdots \tag{2.14}$$

The term $\vec{\mu}_0 \, \langle \chi'|\chi\rangle$ is zero since the initial and final states are orthogonal when $\chi \neq \chi'$.[62] A non-zero transition dipole moment $M_{\chi\to\chi'}$, and thereby a non-zero transition probability, is only achieved for:

$$\boxed{\left(\frac{d\vec{\mu}}{dQ_k}\right) \neq 0} \tag{2.15}$$

hence, if the dipole moment of the bond changes as a function of the displacement of the nuclei. This is the general selection rule for IR spectroscopy. $\frac{d\vec{\mu}}{dQ_k}$ is called the *dynamic dipole moment*.

Further selection rules apply for IRAS due to its special experimental setup, where the IR light is reflected from a (metal) surface.[58, 60, 63, 64]

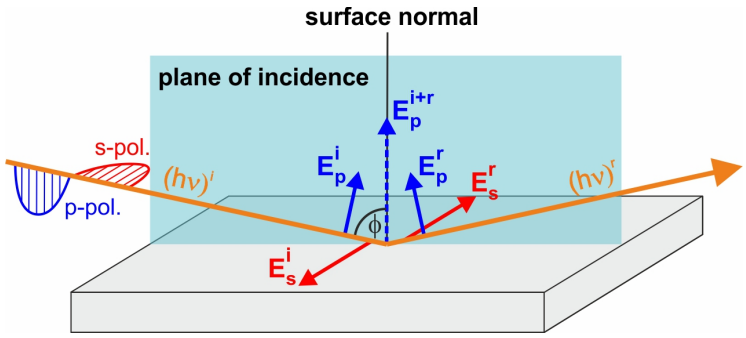

Fig. 2.4: Reflection of IR light at a highly reflective metal surface: Orientation of s- and p-polarized light upon reflection and of electric fields of incident beam (E^i), reflected beam (E^r), and net electric field upon reflection (E^{i+r}).[65]

Parallel (or *p-polarized*) components of the IR light result in an electric field within the plane of incidence, whereas perpendicular (or *s-polarized*) contributions result in an electric field normal to the plane of incidence (see Fig. 2.4). Upon reflection, the IR light undergoes a phase shift depending on its polarization, angle of incidence and frequency (see Fig. 2.5a). Upon reflection, s-polarized light will undergo a phase shift close to 180° for all angles of incidence. With that, the electric field of the reflected beam, E_s^r, will always be directly opposed to the electric field of the incident beam E_s^i. The two opposing electric fields cancel each other out, so that the net electric field E_s^{i+r} is close to zero at the surface. In consequence, s-polarized light cannot excite adsorbate vibrations.
For p-polarized light, in contrast, the phase shift is highly dependent on the angle of incidence. At grazing incidence, p-polarized light will undergo a phase shift close to 90°. The electric field of the resulting reflected beam, E_p^r, will still be oriented within the plane of incidence. More than that, the combination of the electric fields of incoming and outgoing wave will result in an increased electric field E_p^{i+r} normal to the surface. This surface-normal electric field may interact with IR-active adsorbates. The intensity of p-light absorption, expressed by the

function $(E_p^{i+r}/E_p^i)^2 cos^{-1}\Phi$, peaks close to grazing incidence, which is why typically an incidence angle of 83° is used for IRAS measurements.

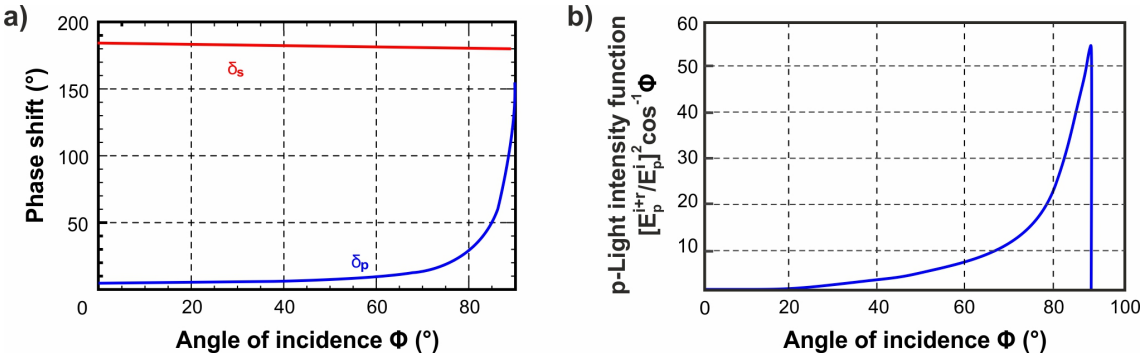

Fig. 2.5: Reflection of IR light on a highly reflective metal surface: a) Phase shift for s-polarized light (δ_s) and p-polarized light (δ_p) as a function of angle of incidence, b) intensity function (i.e. measure for adsorption intensity) for p-polarized light on the surface as a function of angle of incidence. Adapted from [58, 60, 64].

However, p-polarized light does not excite entirely surface-parallel vibrations due to the opposing orientation of the net electric fields of the IR light and the vibrational dipole. In consequence, IRAS can only detect vibrations with a surface-normal contribution to the dynamic dipole moment. This effect is called the IRAS *Surface Selection Rule*:

$$\boxed{\left(\frac{d\mu_\perp}{dQ_k}\right) \neq 0} \tag{2.16}$$

When IRAS is performed on a metal surface, the *Metal Surface Selection Rule* applies in addition. Any dipole moment of an adsorbate on the metal surface will induce an image dipole in the underlying metal (see Fig. 2.6). Dipole moment contributions that are surface-parallel will be canceled by the metal image dipole and may therefore not interact with incoming light. Dipole moment contributions that are surface-normal, on the other hand, will be reinforced by the image dipole. In consequence, the probability for a vibrational transition increases (see eqs. 2.9 and 2.10) and the resulting IR band will gain in intensity.

IR Spectroscopy of Adsorbed Species

IR spectra of adsorbed molecules often differ substantially from spectra of molecules in the gas phase. This section gives a short overview of adsorption-related effects.

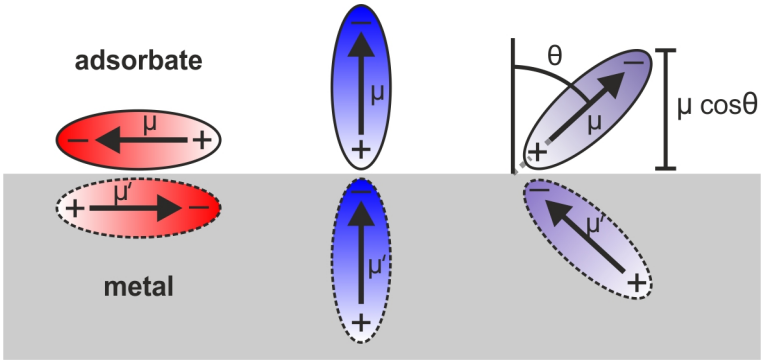

Fig. 2.6: Illustration of the Metal Surface Selection Rule. The surface-parallel contributions to the adsorbate dipole $\vec{\mu}$ are canceled by the image dipole $\vec{\mu'}$ induced in the metal, whereas surface-normal contributions are reinforced. Adapted from [66].

Additional vibrational bands. Upon adsorption, the newly formed adsorbate-substrate bond will hinder translations and rotations of the molecule. To compensate for the reduced number of degrees of freedom, new vibrational features arise for adsorbed species, so-called *frustrated* translations and rotations. Furthermore, adsorption on a surface changes the symmetry of the adsorbing molecule. This may turn gas phase IR-inactive vibrations into IR-active vibrations, if a non-zero dynamic dipole moment is generated (see eq. 2.15).

Frequency shift of an isolated adsorbate. Vibrational frequencies may change upon adsorption through various mechanisms:

"Wall" effect. In a simplified picture, adsorption of a diatomic molecule onto a surface will change its reduced mass in the mechanical mass-spring model. Theoretical calculations predict a shift of the vibrational frequencies upon adsorption of up to $+50$ cm^{-1}.[58] In practice, vibrational frequencies usually shift to lower wavenumbers upon adsorption, which can be explained by additional frequency shift effects (see below).[67]

Image dipole coupling. The interaction between the dynamic dipole of the adsorbed molecule with the mirror dipole in the metal typically results in a shift of vibrational frequencies to lower wavenumbers.[68, 69] For an isolated CO adsorbate, this shift is estimated at -10 cm^{-1}. [68]

Charge transfer. The vibrational frequency of an adsorbed molecule may shift strongly when charge transfer happens between substrate and adsorbate. This charge transfer results in a change of the electronic structure of the adsorbate and

may thereby change its vibrational frequencies. A prominent example for this is the charge transfer from metal substrates to adsorbed CO molecules, which is considered in the *Blyholder model*.[67, 70] The charge transfer (and thereby the frequency shift) is strongly dependent on the environment of the adsorbate. Comparing frequency shifts, especially of adsorbed CO as a probe molecule, is a valuable tool to characterize adsorption sites on surfaces.[58, 71–74]

Frequency shift due to adsorbate-adsorbate interactions. Further frequency shifts may arise due to the interaction between adsorbates at higher coverages:

Dipole-dipole coupling. With increasing coverage, and thus decreasing distance between adsorbates, coupling of the adsorbate dipole with neighboring dipoles becomes important. Dipole-dipole coupling may happen with the dipoles of neighboring adsorbates and with neighboring mirror dipoles in the metal.[68, 69]

Competition for charge transfer. With an increased number of molecules adsorbed on the surface, less charge may be transferred between the substrate and the individual adsorbate as compared to the case of an isolated adsorbate. In consequence, changes in the electronic structure of the individual adsorbate will not be as considerable, which will result in a less pronounced frequency shift.[68, 70]

Intensity effects.

Adsorbate geometry. The IRAS Surface Selection Rule (see 2.16) only allows the excitation of vibrations with a surface-normal contribution to the dynamic dipole moment. If a molecule adsorbs on the surface in a preferential geometry, the band intensity of vibrations with mostly surface-normal contributions will be larger than the intensity of vibrations with mostly surface-parallel contributions. If adsorbates change their adsorption geometry, e.g. through self-assembly effects at high coverage, the intensity ratio of the vibrational features will change accordingly.

Dipole strength. After Fermi's Golden Rule (eqs. 2.9 and 2.10), the probability of a transition (and thereby the intensity of an IR band) depends strongly on the strength of the respective dipole. In consequence, the intensity of vibrational bands of differently strong dipole absorbers does not directly translate to a difference in their respective coverages.

Depolarization. At large coverage, dipole-dipole interactions between adsorbates may cause depolarization of the individual adsorbate. This results in smaller

intensities of the IR bands of the individual adsorbate compared to an isolated adsorbate.[68]

Intensity borrowing. If adsorbates in close proximity vibrate with similar frequencies, intensity of the low-frequency vibration may be transferred to the high-frequency vibration through dipole-dipole coupling.[75]

2.2.3 X-Ray Photoelectron Spectroscopy (XPS)

X-Ray Photoelectron Spectroscopy (XPS) is a quantitative, surface-sensitive technique to characterize the electronic structure of substrate and adsorbates. In XPS, X-ray radiation induces the emission of photoelectrons from the sample. By analyzing the binding energy of these photoelectrons, alongside with other peak characteristics (e.g. intensity, peak width), XPS provides valuable information on

1. electronic structure and elemental composition of substrate and adsorbates (qualitatively and quantitatively),

2. chemical state (and local environment) of substrate and adsorbate species, and

3. variations of the above in different probing depths.

The practical strengths of XPS lie in its wide range of applicability (all elements apart from H and He can be traced) and its underlying solid theoretical basis. A practical challenge to XPS is the need for a high vacuum environment to ensure an undisturbed trajectory of the photoelectrons from sample to analyzer. Instrumental developments in the past decades have made it possible to perform XPS in high pressure environments; this technology, however, involves complex setups and is not yet the experimental standard. Since XPS involves an electronic probe, it is restricted to conductive samples (including thin non-conductive films on metal substrates) to avoid charging effects.

Working Principle and Instrumentation

A typical XPS setup is shown schematically in Fig. 2.7a. X-rays (emitted from an X-ray source) irradiate the sample and thereby cause emission of photoelectrons from the electronic core levels of the sample atoms. This phenomenon is called the *Photoelectric Effect*.[76]

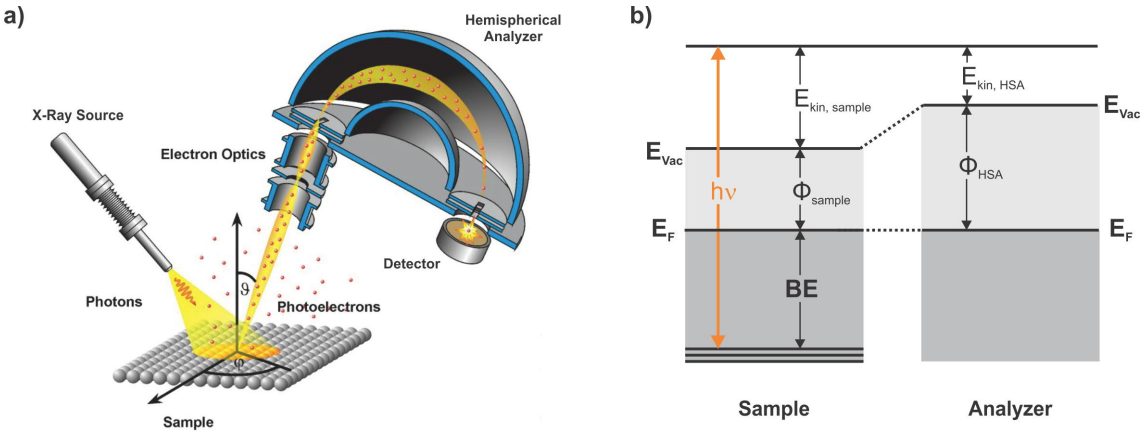

Fig. 2.7: Typical XPS setup: a) Instrumentation and measuring geometry, adapted from [77], b) relevant energy levels for BE measurements.

The emitted photoelectrons are filtered according to their kinetic energy in a hemispherical analyzer (HSA). The HSA consists most basically of two stacked hemispheres onto which different potentials may be applied. Photoelectrons, as they are emitted from the sample, enter into the space between the hemispheres through a set of electrostatic lenses. There, depending on their kinetic energy, the electrons will follow different trajectories. At specific potentials applied to the hemispheres, only electrons with a specific kinetic energy will be able to pass the HSA without colliding with the walls. Tuning the HSA potentials allows for an energy filtering of the electrons, which are finally collected at an electron detector.
Sample and analyzer are electrically connected to the same ground, which causes their Fermi energy levels (E_F) to align (see Fig. 2.7b). Knowing the energy of the exciting X-ray radiation $h\nu$, the work function of the analyzer, Φ_{HSA}, and the kinetic energy of the electrons in the analyzer, $E_{kin,HSA}$, allows to calculate the binding energy (BE) of the core electrons:[78]

$$\boxed{BE = h\nu - E_{kin,HSA} - \Phi_{HSA}} \tag{2.17}$$

Peak Intensity

To quantify the intensity of photoemission features, an often made approximation is to neglect elastic collisions of the photoelectrons. The current of photoelectrons generated by emission from electronic level j of atoms i is then expressed as follows:[79, 80]

$$I_{ij} = C \cdot M \cdot \sigma_{ij} \cdot L_{ij}(\gamma) \cdot T(E_{kin}) \cdot \int x_i(z) exp\left(\frac{-z}{\lambda(E_{kin}) cos\Theta}\right) dz \tag{2.18}$$

where C includes all experimental constants, such as incident X-ray flux, analyzed area, analyzer acceptance angle, and detector efficiency. Other parameters are defined as follows:

M	total atomic density
σ_{ij}	photoionization cross section for emission from specified energy level
L_{ij}	angular asymmetry factor for emission from specified energy level
γ	angle between X-ray direction and direction of analyzer
$T(E_{kin})$	transmission function of analyzer
E_{kin}	kinetic energy of photoelectrons
$x_i(z)$	concentration of element i in depth z
$exp\left(\frac{-z}{\lambda cos\Theta}\right)$	attenuation of electrons emitted from depth z (see 'Probing Depth')
$\lambda(E_{kin})$	inelastic mean free path
Θ	angle of emission with respect to surface normal

The intensity of an XPS feature will be largely determined by the photoionization cross section σ_{ij}. σ_{ij} is the transition probability (per unit time and incident flux) for excitation from the initial state Ψ_i to the final state Ψ_f. Considering the X-ray radiation as a time-dependent perturbation, σ_{ij} is given by Fermi's Golden Rule:

$$\sigma_{ij} \propto |M_{i\to f}|^2 \tag{2.19}$$

$$\sigma_{ij} \propto |\langle\Psi_f|\vec{p}\vec{A}|\Psi_i\rangle|^2 \tag{2.20}$$

where $\vec{p}$ is the momentum operator and $\vec{A}$ represents the electromagnetic field of the radiation. Therefore, theoretically speaking, σ_{ij} is a measure of the overlap between the initial and final state of the system's wave function under the influence of the incident X-rays.

Quantification of XP spectra aims at calculating x_i from the measured electron current I_{ij} (in practice the integrated area of an XPS peak). Ultimately, this is only possible when all contributions of the experimental setup are known. Most often, however, the calculation of the *relative* atomic concentrations is sufficient. In this case, the constant contributions of the experimental setup cancel each other out. Furthermore, when photoemission signals at similar BE are considered for quantification, the energy-dependent terms may be approximated as equal. Assuming further that the different types of atoms are equally distributed in the volume of the sample, and considering spectra obtained at the same angle Θ, one obtains the relative atomic concentration of i as a fraction of all considered types of atoms k:

$$x_i = \frac{I_{ij}/(L_{ij}\sigma_{ij})}{\sum_{k=1}^{n} I_{kj}/(L_{kj}\sigma_{kj})} \tag{2.21}$$

Probing Depth

The photoelectron's escape depth from a sample is finite due to inelastic and elastic scattering events with surrounding atoms. The inelastic scattering in the solid is predominantly determined by the electron's kinetic energy and largely independent of the sample material. It is quantified by its *inelastic mean free path* λ, i.e. the average length the electron may travel without experiencing inelastic collisions. The intensity decay due to inelastic scattering is given in first approximation as:

$$I(z) = I(0) \cdot exp\left(\frac{-z}{\lambda(E_{kin})cos\Theta}\right) \tag{2.22}$$

where $I(z)$ is the intensity contribution from sample depth z and $I(0)$ is the unattenuated intensity contribution. Empirical values of λ in various elements are summarized in the so-called *Universal Curve* (see Fig. 2.8).[81]

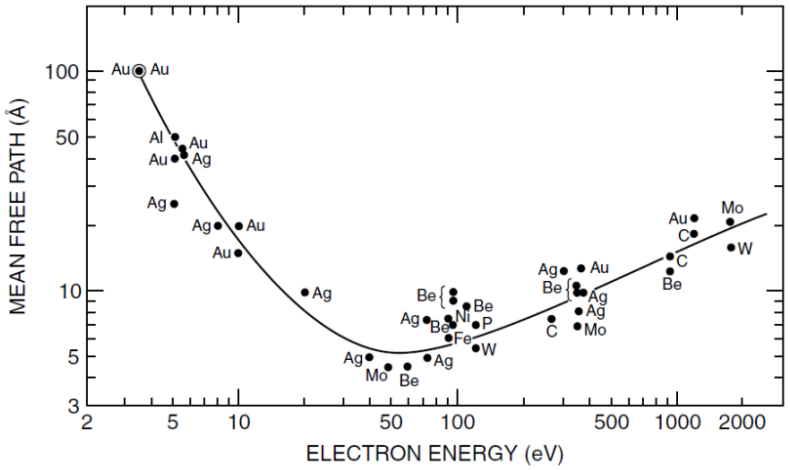

Fig. 2.8: Universal curve for various elements, showing the dependence of the inelastic mean free path λ on the electron's kinetic energy.[82]

In a rough approximation, the probing depth in normal emission (Θ=0) is estimated to be $\sim 3\lambda$. The kinetic energies of photoelectrons in XPS (when using AlK_α or MgK_α radiation, as in typical lab setups) are in the order of $10^2 - 10^3$ eV, which results in an attenuation length of several nanometers. The surface sensitivity may be increased in *grazing emission geometry*, i.e. if the sample is tilted with respect to the analyzer. Due to the tilting, emitted photoelectrons have to travel longer distances to escape the sample, which ultimately decreases the effective probing depth.

Spectral Features

Fig. 2.9 shows a typical XP spectrum of a clean Ru(0001) single crystal over the whole photoelectron energy range (excitation by Al K_α radiation, 1486.6 eV). In the following, an overview of the most common spectral features in XP spectra shall be given. For more detailed information, please refer to references [78, 83, 84].

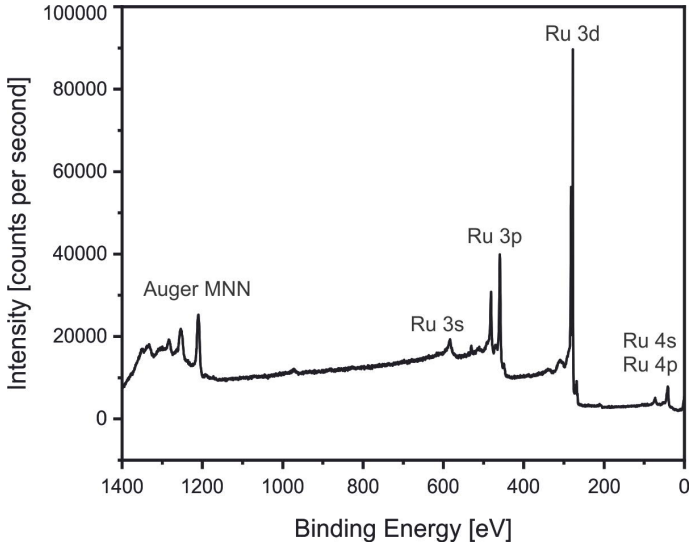

Fig. 2.9: Full energy range XP spectrum of a clean Ru(0001) single crystal (AlK_α source, $\Theta = 0$).

Core level peaks. The most dominant peaks in XP spectra are caused by photoelectron emission from the sample atoms' core levels, which reach the analyzer without energy losses. The core level peaks provide qualitative and quantitative information on the sample's chemical composition, since (i) the BE of the core levels is unique to each element, and (ii) the area of each photoemission peak is related to the electron population of the corresponding energy state. Core level peaks are commonly denoted as nl_j after the quantum numbers n, l, and j associated with the initial state energy levels. Photoemission from energy levels with $l > 0$ (p,d,f-orbitals) gives rise to peak doublets due to coupling of spin and orbital angular momentum (*spin-orbit coupling*) within the single electron that remains in the orbital after photoionisation. The relative intensities of the spin-orbit split peaks is given as a ratio of the degeneracies $(2j + 1)$ of the states. The Ru 3d level, for example, is split into a $3d_{3/2}$ and a $3d_{5/2}$ state. In the XP spectrum, these states appear as a doublet around 280 eV BE, with a peak area ratio of $(2 \times \frac{3}{2} + 1)$:$(2 \times \frac{5}{2} + 1)$=2:3.

Even though the core level energies are a fingerprint structure for each element, slight shifts in the BE may happen in an individual sample due to interactions of the probed atoms with their chemical environment. The resulting relative differences in BE are referred to as *Chemical Shifts* and allow to distinguish the chemical state of the probed atom upon photoemission. Even though the chemical shift is largely determined by the initial state of the atom (before photoemission), final state effects, such as relaxations, might need to be taken into account in individual cases.

The peak width ΔE (defined as the full width at half maximum, FWHM) of a photoemission peak is determined in a first approximation by the contributions of natural line width ΔE_n, line width of the X-ray source ΔE_s, and the analyzer resolution ΔE_a:

$$\Delta E = \left(\Delta {E_n}^2 + \Delta {E_s}^2 + \Delta {E_a}^2\right)^{1/2} \tag{2.23}$$

The natural line width is associated with the core hole lifetime τ according to *Heisenberg's Uncertainty Principle* ($\Delta E_n = \frac{h}{\tau}$). It is determined by the nature of the core hole decay process: After emission of the photoelectron, the core hole will be refilled by an electron from a higher energy level. During that transition, the system may lose excess energy by emission of a photon (X-ray fluorescence) or by emission of a secondary electron (Auger process).
The natural line shape of a photoemission peak is a Lorentzian distribution. However, the passing of the electrons through the analyzer causes additional Gaussian broadening. In consequence, XPS peaks are typically fitted with a convolution of Lorentzian and Gaussian distribution, the so-called *Voigt profile.*[85]

Valence level peaks. At low BE, low intensity bands appear in the XP spectrum as a result of photoemission from valence levels. For metals, which have a filled continuous valence band, a (thermally broadened) Fermi step function can be fitted across the Fermi level and further used to calibrate the BE scale.

Auger Emission peaks. The decay of core holes by the Auger process is accompanied by the emission of secondary electrons, which show up as distinct peaks in the XP spectrum. The kinetic energy of the Auger electrons, in contrast to the primary photoelectrons, is independent of the photoemission excitation

energy. In consequence, Auger peaks may be identified as their apparent BE changes with the X-ray source excitation energy (e.g. AlK_α vs. MgK_α).

Satellites. Satellite peaks appear in the XP spectrum mainly through two events, *shake-up* and *shake-off* processes. In a shake-up process, the emission of a photoelectron simultaneously excites a valence electron to a higher, unfilled energy level. Similarly, in a shake-off process, a valence electron is excited and ultimately ejected as a secondary photoelectron. Both processes result in an energy loss of the primary photoelectron. Shake-up and shake-off features thus appear as satellite bands at the high BE site of the elastic photoemission peaks.

Multiplet splitting. The unpaired core electron remaining after photoionization may couple with unpaired electrons in the valence shell by *j-j-coupling*. This results in a variety of final states with different energies that show in the XP spectrum as multiple distinct photoemission peaks.

Plasmon losses. During photoelectron emission, surface or bulk plasmons (collective oscillations of the conduction electrons) may be excited. As a result, plasmon loss peaks of low intensity may arise at the high BE site of an elastic photoemission peak.

Background. XP spectra include background intensity, which is caused by the detection of photoelectrons that have lost energy on their way to the analyzer. This may happen through inelastic scattering of the photoelectrons in the sample material, causing an increase in the background at the high BE site of a core level peak. Furthermore, non-monochromatized X-ray sources will emit a continuous *Bremsstrahlung* radiation in addition to the characteristic X-ray lines, which will cause the sample to emit additional photoelectrons in a continuous energy range. To evaluate the photoemission peak intensity, the background is most commonly subtracted as a step-like Shirley function,[86] which is iteratively fitted to the data points.

2.2.4 Temperature Programmed Desorption (TPD)

Temperature Programmed Desorption (TPD) is a method of mass spectrometry which yields the partial pressure of individual compounds desorbing from a sample when it is heated at constant rate. TPD provides valuable information about desorption energies and desorption kinetics.

Working Principle and Instrumentation

In a typical TPD experiment, the sample is exposed to a controlled amount of gas molecules, which adsorb onto its surface. The sample is then heated at a constant rate in front of a mass spectrometer, which analyzes the desorbing molecules. TPD measurements require a well-defined heating rate, which is achieved by use of a feedback system within the heating setup, commonly in form of a proportional–integral–derivative (PID) controller.

Most TPD setups use a quadrupole mass spectrometer (QMS) for gas analysis, which allows for high sensitivity and time resolution while being very compact. In the first stage of the QMS, gas molecules are ionized by electron bombardment. Thereby fragmentation into lighter ions may occur especially for organic compounds, which should be taken into account for analysis. The single or multiply charged ions travel in a mass analyzer, which consists of four parallel, cylindrical rods, to which oscillating electric fields may be applied. For a given ratio of voltages applied to the rods, only ions with a specific mass-to-charge ratio are able to pass, while other ions collide with the analyzer walls. Passing ions are finally detected in an electron multiplier.
In order to suppress the detection of gas from the chamber background, a chemically inert cone may be placed around the ion source for isolation. A small opening in the cone close to the sample allows for desorbing gases to enter. The inside of the cone may be differentially pumped to minimize re-adsorption onto the sample surface.

Accessible Information

TPD may provide detailed insights into the thermodynamics and kinetics of desorption processes, especially when flat, homogeneous surfaces are analyzed. Its simple technical setup and low level of experimental complexity make TPD a popular tool to investigate the following:

Composition of desorbing species. The detected mass of desorbing species or their fragments allows to identify their chemical identity.

Estimation of surface coverage. The desorption peak area in TPD is proportional to the total number of desorbing species, so that quantitative studies are possible. A quantitative analysis of the peak area, calibrated by a known standard to account for ionization efficiency of the desorbing species, allows to determine surface coverages.

Determination of desorption energies and kinetics. Several analysis methods allow the determination of desorption energies and kinetics from TPD data (see 'Quantitative Analysis').

Dinstinction of adsorption modes and local environments. Multiple desorption peaks may indicate different possible binding modes of the adsorbate or desorption from different local environments on the sample surface.

Thin film characterization. TPD may be used in the characterization of thin (oxide) films grown onto metal substrates. If a particular molecule adsorbs only on the metal surface, but not on the thin film, a quantitative desorption experiment will show whether the substrate is completely covered by the oxide film.

Quantitative Analysis

The quantitative analysis of TPD is based on the *Polanyi-Wigner equation*, which describes the desorption rate r_{des} as the change in surface coverage θ of an individual adsorbate i over time:

$$r_{des} = -\frac{d\theta_i}{dt} = \nu_n \cdot {\theta_i}^n \cdot exp\left(-\frac{E_{des}}{RT}\right) \tag{2.24}$$

where ν_n is a pre-exponential factor, n is the desorption order, E_{des} is the activation energy for desorption, R is the ideal gas constant, and T is the temperature.

Fig. 2.10 shows calculated desorption rates for zero, first, and second order desorption processes. In *zero order* desorption (n=0), the desorption rate is independent of the coverage. This is the case, for instance, for desorption of homogeneous multilayer films. In *first order* desorption (n=1), the desorption rate is proportional to the coverage, which indicates that adsorbates desorb individually. The pre-exponential factor for first order desorption, ν_1, is assumed to be in the order of the vibrational frequency of the adsorbed particle on the surface ($\sim 10^{13}$ s^{-1}). In *second order* desorption (n=2), the desorption rate is proportional to θ^2. This is typically the case for desorption processes in which a recombination of two individual adsorbates happens before desorption, e.g. in the recombinative desorption of H_2O from surface OH groups. Complicated kinetic desorption processes might result in other, even fractional, desorption orders.

Since ν_n and E_{des} are functions of the coverage θ_i, the exact solution of the Polanyi-Wigner equation is complex. An often used simplification is to assume that ν_n and

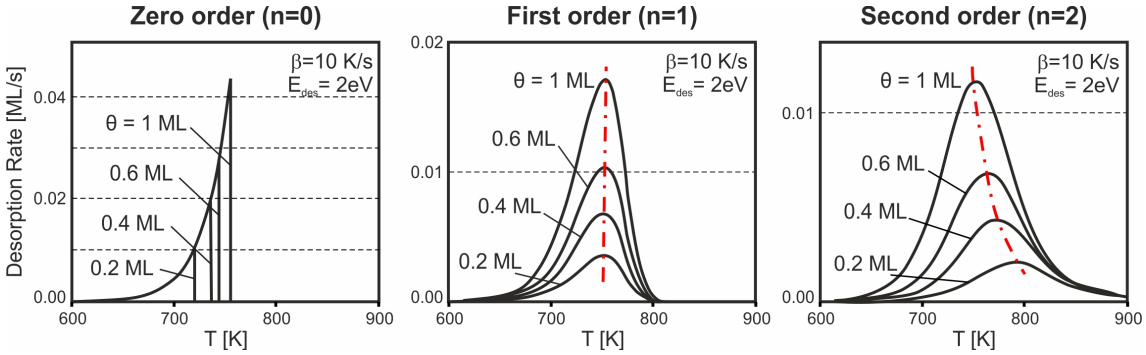

Fig. 2.10: Calculated TPD spectra for zero order, first order, and second order desorption processes at various initial coverages. ν_n and E_{des} are assumed to be independent of θ. Red curves indicate changes in desorption rate maximum of the peaks. Adapted from [57].

E_{des} are independent of θ_i. This is implemented in a *Redhead Analysis*[87]. Redhead's Analysis solves the Polanyi-Wigner equation for T_{max}, the temperature at which the desorption rate of an individual desorption peak is maximal ($-d^2\theta/dT^2 = 0$):

$$\frac{E_{des}}{RT_{max}^2} = \frac{n\nu_n}{\beta} \cdot \theta_{i,max}^{n-1} \cdot exp\left(-\frac{E_{des}}{RT_{max}}\right) \tag{2.25}$$

where $\theta_{i,max}$ is the coverage at the desorption maximum, and β is the heating rate ($T = T_0 + \beta t$).

For first-order desorption, $\theta_{i,max}^{n-1}$ equals 1, which further facilitates the equation. Solving 2.25 for E_{des} then yields:

$$E_{des} = RT_{max}\left(ln\frac{\nu_1 T_{max}}{\beta} - ln\frac{E_{des}}{RT_{max}}\right) \tag{2.26}$$

E_{des} increases approximately linearly with T_{max}, so that the last (small) term may be approximated:

$$E_{des} = RT_{max}\left(ln\frac{\nu_1 T_{max}}{\beta} - 3.64\right) \tag{2.27}$$

Another approach is the *Leading Edge Analysis*,[88] which assumes that the coverage is roughly constant in a small temperature window at the low-temperature side of a desorption peak ($\theta_i = \theta_{i,0}$). Furthermore, ν_n is considered constant.

$$lnr_{des} = ln\nu_n + nln\theta_{i,0} - \frac{E_{des}}{RT} \tag{2.28}$$

Using only the first data points of the desorption peak, lnr_{des} is plotted against $1/T$ in an Arrhenius plot. E_{des} is determined from the slope. $ln\nu_n + nln\theta_{i,0}$ may be

determined from the intercept. This method, however, requires high quality TPD data in order to yield reliable results.

In a more integral approach, E_{des} is extracted from TPD data following the *method of King*[89], also known as *complete analysis*. For this, TPD spectra are measured at various initial coverages. A specified surface coverage $\theta_{i,fix}$ is reached at different temperatures in the different TPD experiments:

$$lnr_{des} = ln\nu_m + mln\theta_{i,fix} - \frac{E_{des}}{RT} \tag{2.29}$$

By plotting lnr_{des} against $1/T$, E_{des} is determined from the linear slope. The intercept determines $ln\nu_n + nln\theta_{i,0}$.

2.2.5 Gas Chromatography (GC)

Gas Chromatography (GC) is a standard tool for qualitative and quantitative analysis of mixtures of gas or easily volatile compounds. Its technical simplicity, versatility, and high sensitivity make GC especially attractive to investigate the performance of gas-solid catalytic reactions. Detailed information on the technique may be found in reference [90].

Working Principle and Instrumentation

Fig. 2.11 shows a schematic representation of the system used in the following for catalyst performance tests. The system consists of a "high pressure" reaction cell, to which a commercially available gas chromatograph is attached. The reaction gas mixture to be analyzed (dissolved in a chemically inert carrier gas) is continuously circulated in the system via a circulation pump. After a programmed time interval, a section of the gas mix is injected into the gas chromatograph, where it travels through a column (or a system of multiple columns in series). The gas compounds spend an individual time traveling through the column and arrive at the detector separated by an individual time delay, depending on the strength of interaction with the column wall and the length of the column. Finally, a detector records the quantity of ejected compounds as a function of the total retention time.

The most commonly used GC detectors are thermal conductivity (TCD) and flame ionization detectors (FID). At the heart of a TCD is a heated filament wire, which changes its temperature (and thus its resistance) according to the thermal conductivity of a gas that is passed over it. This change in resistance is a quantitative probe

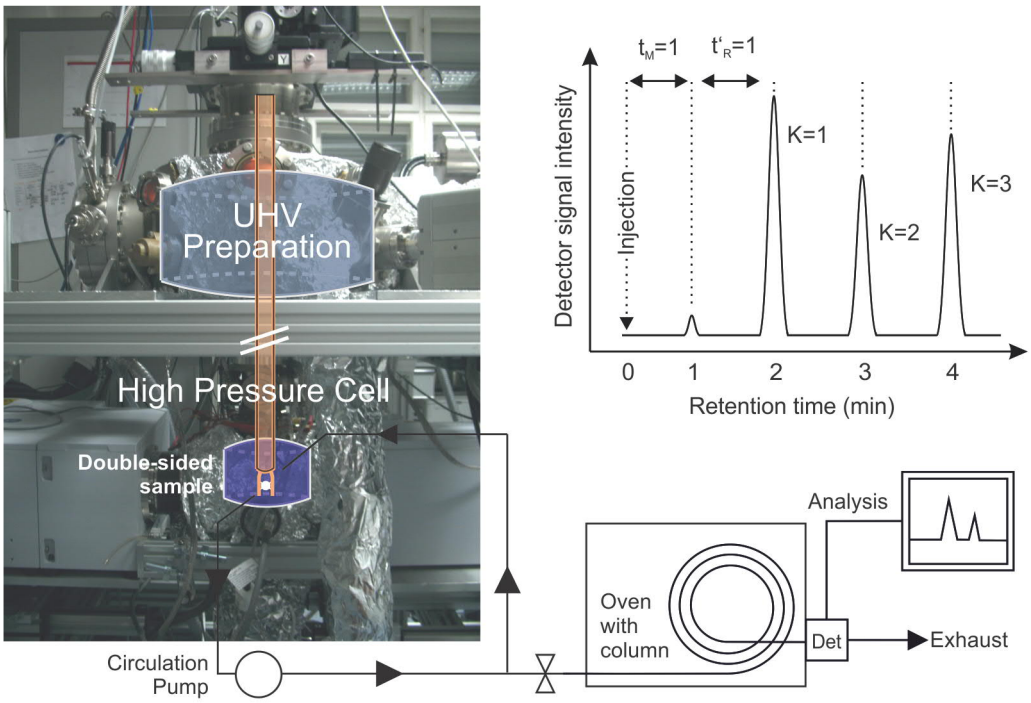

Fig. 2.11: Schematic representation of gas chromatography setup. Inset: Determination of t_M, t'_R, and retention factor K from GC output.

of the concentration of the respective gas. The practical strengths of a TCD are its technical simplicity and very reproducible response, while a practical weakness is its low sensitivity.

In an FID, organic compounds pass over a flame and thereby form ions, which are collected on a pair of charged electrodes. The amount of ions generated is compound-specific and depends on the number of carbon atoms and their respective oxidation state, which makes a calibration with a pure compound sample necessary. A practical strength of an FID is its high sensitivity, allowing to detect components even in the ppb range.

Compound Separation and Chemical Identification

For set column parameters, the retention time within the column is compound-specific and may serve chemical identification. The total retention time t_R that a compounds spends in the column may be expressed as:

$$t_R = t_M + t'_R \tag{2.30}$$

Here, t_M is the mobile phase residence time (i.e. the time spent in gas phase), which is determined by the carrier gas velocity and the column length, and thus is equal for all compounds. t'_R is the stationary phase residence time (i.e. the time the compound spends interacting with the column walls), which is individual for each compound due to its individual functionalities. The choice of column type is essential for the level of separation of the individual compounds, since the column's stationary phase material will determine its polarity, adsorbability, etc., and thereby the exchange equilibrium with the sample components in the gas phase. Comparison of the measured retention time of a compound with the retention time of pure reference compounds allows for chemical identification.

A simple value to compare the interaction strength of different compounds with the column is the retention factor K (see also Fig. 2.11):

$$K = \frac{t'_R}{t_M} \tag{2.31}$$

Compound separation might be difficult if multiple compounds show similar retention factors. In this case, the column temperature may be adjusted to increase t'_R for the individual compounds and thereby the separation on the retention time scale.

Quantitative Analysis

The peak signal in the recorded chromatogram may be treated in first approximation as a Gaussian line profile.[90] Analysis of the peak area (with calibration of the detector response, if necessary) gives the relative concentration of the individual compounds in the gas mixture.

2.2.6 Nuclear Reaction Analysis (NRA)

Nuclear Reaction Analysis (NRA) is a method to evaluate the near-surface depth distribution of a particular target element in a solid material. In NRA, the sample is irradiated with a high energy ion beam, which initiates a nuclear reaction with the target element and generates a nucleus in excited state. When decomposing, this nucleus emits ionizing radiation, which serves as a quantitative probe for the target element concentration.

This section gives an overview of a specific NRA method, $^{1}\mathrm{H}(^{15}\mathrm{N}, \alpha\gamma)^{12}\mathrm{C}$-NRA (H-NRA), which is used in the following to evaluate the depth distribution of H species

within solid samples. The H-NRA method is an indispensable tool for the analysis of solids towards their H content. Other methods of material characterization, like electron diffraction or photoelectron spectroscopy, are effectively blind to the H atom due to its light mass and small number of electrons.

H-NRA requires a UHV environment to ensure that no impurities accumulate on the surface during the measurement. It is a highly versatile method, given that it may be applied to any vacuum-compatible material with a smooth surface. Other strong features of the technique are its high sensitivity (∼100 ppm H) and its large probing depth range of at least 2 µm. Practical drawbacks of H-NRA are its insensitivity for the H species' chemical state, and - if used for the analysis of thin film model catalysts - its relatively broad depth resolution (1-3 nm). More detailed information and example studies of H-NRA may be found in references [91] and [92].

Working Principle and Instrumentation

^{1}H(^{15}N, $\alpha\gamma$)^{12}C-NRA probes the concentration of H nuclei by following a nuclear reaction:

$$^{15}\mathrm{N} + {}^{1}\mathrm{H} \xrightarrow{6.385\,\mathrm{MeV}} {}^{16}\mathrm{O}^{*} \longrightarrow {}^{12}\mathrm{C} + \alpha + \gamma \tag{2.32}$$

To induce the reaction, a beam of $^{15}N^{2+}$ ions is accelerated to the reaction's resonance energy (E_{res}=6.385 MeV) and directed onto the sample material. The acceleration of the beam to this high kinetic energy is essential for it to overcome the Coulomb barrier between the nuclei, and makes it necessary to perform the NRA experiment at a particle accelerator facility (single stage or tandem accelerator). When the ion beam hits the sample, the nuclear reaction takes place only if ^{1}H nuclei are present. ^{15}N and ^{1}H nuclei fuse to form an excited ^{16}O nucleus, which instantaneously decomposes into an excited ^{12}C nucleus by $\alpha(He^{2+})$-decay. The excited ^{12}C nucleus furthermore relaxes by emission of γ-radiation (4.43 MeV).
Finally, a scintillation detector outside the vacuum chamber records the intensity of the emitted γ-radiation. The detector response is calibrated by analysis of a sample with known H content to account for instrument-specific scaling effects.

Depth Profiling

The width of E_{res} in H-NRA is very narrow with respect to its total value (1.8 keV vs. 6.385 MeV) and the probability of a nuclear reaction happening off-resonance is about 4 orders of magnitude smaller than with a resonant beam. Probing the sample with a mono-energetic ion beam at E_{res} will cause a nuclear reaction only in close

proximity to the surface, since scattering of the beam inside the material causes a loss in energy large enough to make a nuclear reaction in deeper layers improbable. This phenomenon is exploited to acquire H concentration depth profiles.

The energy loss of the ion beam when entering the sample is proportional to the trajectory length z inside the sample:

$$\Delta E(z) = Sz \tag{2.33}$$

where S is the stopping power of the sample material (typically ∼1-4 keV/nm). With this, a trajectory path of a few atomic layers is already enough to shift the ion energy out of resonance.

The detection depth d (measured normal to the sample surface) may be calculated from z, knowing the sample geometry (the angle α between the surface normal and the incident $^{15}N^{2+}$ ion beam):

$$d = zcos\alpha \tag{2.34}$$

To obtain information from deeper layers, the energy of the incident ^{15}N ion beam, E_i, has to be chosen such that it reaches E_{res} only after scattering losses:

$$E_i = E_{res} + \Delta E(z) \tag{2.35}$$

Combining eqs. 2.33 and 2.34 gives the corresponding probing depth for any given ion beam energy:

$$d(E_i) = \frac{cos\alpha(E_i - E_{res})}{S} \tag{2.36}$$

To obtain a H depth profile of the sample, the ion beam energy is increased stepwise and the γ-ray response recorded for each energy (which translates to an individual probing depth). Finally, the experimental excitation curve, $Y(E_i)$, plots the detected γ-ray yield as a function of the incident ion beam energy, and thereby gives the H depth profile, which is convoluted with an effective instrumental function $F(E, E_i, z)$:

$$Y(E_i) = KN_i \int_0^\infty F(E, E_i, z) \circledast n_H(z) dz \tag{2.37}$$

where K is the instrument's γ-ray detection efficiency factor, N_i is the incident beam flux [$cm^{-2}s^{-1}$], and $n_H(z)$ is the H density [cm^{-3}]. $F(E, E_i, z)$ describes additional broadening of the function due to (i) the ion beam source's energy distribution, (ii) a Doppler effect coupling with the H-substrate vibration, and (iii) scattering of the $^{15}N^{2+}$ ions within the sample material (depending on the trajectory length z). The instrument function introduces broadening in shape of a Voigt function.

Radiation Effects

In comparison to other methods of concentration depth profiling (e.g. Secondary Ion Mass Spectrometry), NRA is classified as a non-destructive technique. However, depending on the sample material, radiation effects may need to be taken into account:

Residual ^{12}C. ^{12}C nuclei created by the nuclear reaction retain a large velocity in direction of the ion beam incidence. As a result, they are ultimately deposited far inside the sample bulk, in depths that are not accessible anymore with NRA. The sample alteration by this effect is negligible.

Sputtering of light elements. Permanent damage to the sample atoms by direct interaction with the $^{15}N^{2+}$ ion happens only in about 1% of the energy loss scenarios and is therefore negligible. Energy loss happens in the vast majority of cases by inelastic collisions with electrons in the sample material. This generates a large number of excited electrons for each incident $^{15}N^{2+}$ ion. In conductors, the surplus energy is quickly dissipated into the bulk. In non-conductive materials, loss of light elements (H, C, N, O) may occur.

The extent of radiation damage strongly depends on the sample material and may be tested in the individual case by comparing a series of H depth profiles (recorded in sequence on the same irradiation area) for consistency.

2.3 Main Experimental Setup

LEED, IRAS, XPS, TPD, and GC experiments were performed in a UHV system at the Fritz Haber Institute of the Max Planck Society in Berlin, Germany. Fig. 2.12 shows a schematic representation of the apparatus. The system, with a base pressure of $\sim 1 \times 10^{-10}$ mbar, consists of a preparation chamber and a high pressure cell.

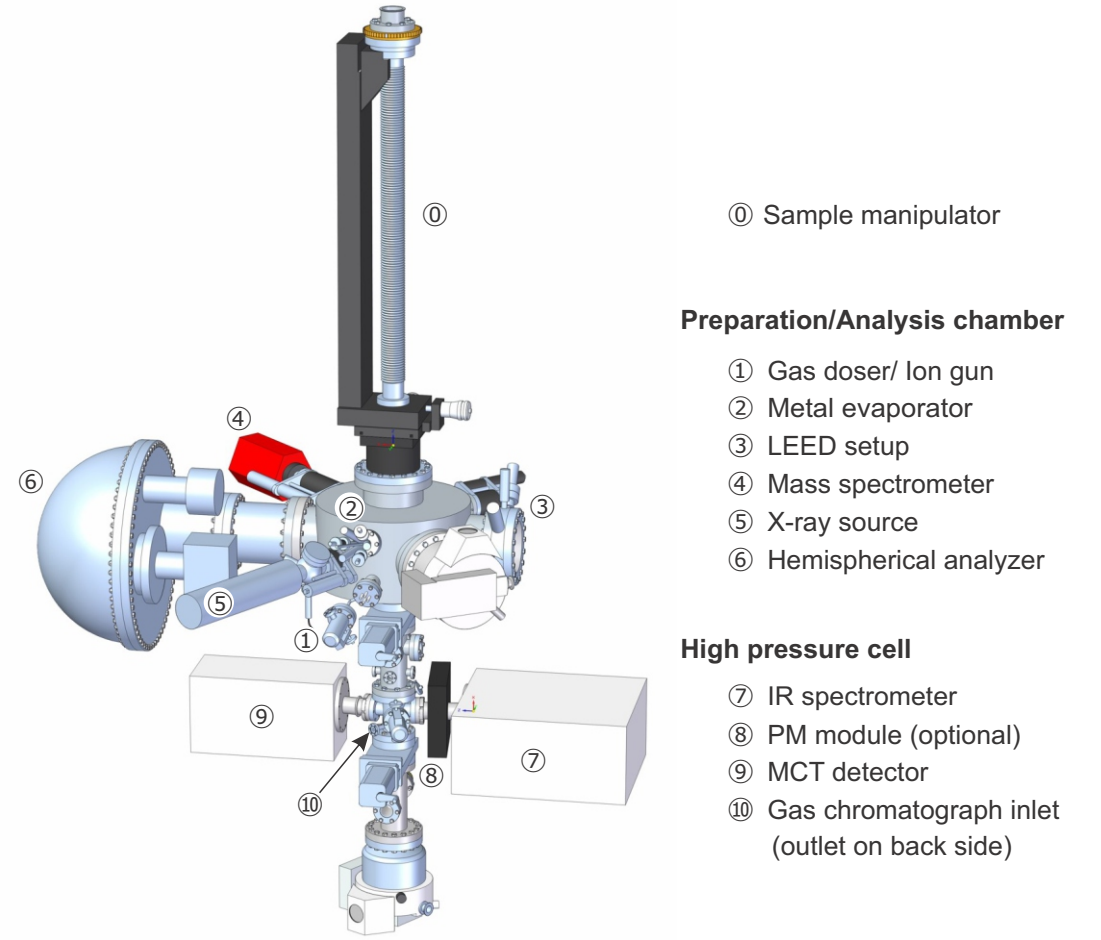

Fig. 2.12: Schematic representation of the main experimental chamber.

The preparation chamber is equipped with standard tools for crystal cleaning, thin film growth, and sample characterization. It contains a sputter gun (Specs IQE 11), an electron beam evaporator (Focus EFM 3T and EFM 3 used interchangeably), a LEED system (Specs ErLEED 1000-A), a differentially pumped quadrupole mass spectrometer (Hiden HAL 201-RC), and an XPS system (Specs XR 50, PHOIBOS 150 MCD). The outlet of the sputter gun (with the ion source deactivated) was used to dose gases into the chamber. The sample (cylindrical, 10 mm diameter,

2 mm thick) was mounted onto the manipulator via spot-weld Ta wires. It could be resistively heated to ∼1300 K and cooled to ∼90 K by filling the manipulator rod with liquid N_2. The sample temperature was determined by a K type thermocouple spot-welded onto the back or the edge of the sample.
LEED patterns were investigated at a screen voltage of 6 kV and a filament current of ∼2.35 A. XPS experiments were performed using an AlK_α source and a pass energy of 20 eV at the HSA. The XPS measuring geometry could be freely altered. Spectra were recorded in normal emission (Θ=0°) and grazing emission (Θ=60°). Calibration of the XPS setup was performed using the position of the Ru 3d peaks as a reference. Deconvolution and quantification of XP spectra was performed in the CasaXPS software package. TPD measurements were performed with a steady heating ramp of 2 K/s, controlled by a PID temperature controller.

The high pressure cell (380 cm^3 in volume) is equipped with a gas inlet, a GC setup, and an IRAS spectrometer (Bruker i66v) with a mercury cadmium telluride (MCT) detector. IRAS spectra were recorded at a spectral resolution of 4 cm^{-1}. With the sample in IRAS position, the chamber may be filled with gases up to a pressure of ∼1 bar, while still keeping the preparation chamber (sealed by spring energized Teflon O-rings) under high vacuum pressure. Furthermore, a gas chromatograph (Agilent 6890A, TCD and FID detectors) is connected to the chamber via an inlet and an outlet, allowing for the gas inside the chamber to be continuously circulated within the system by a membrane pump. This way, GC experiments were carried out with the high pressure cell serving as a batch reactor. Ar was used as a carrier gas for any GC experiment, ensuring a stable overall pressure of ∼1000 mbar. The gas was allowed to circulate for 5 min prior to the first GC analysis to ensure an equilibrated concentration of gas in the system. GC experiments were carried out in split-less mode on a HP-PLOT Al_2O_3 'KCl' column at 353 K.

2.4 Nuclear Reaction Analysis Setup

NRA was performed in a UHV system (base pressure ∼1×10^{-10} mbar) connected to the 1E beam line of the MALT ion accelerator at the University of Tokyo, Japan. The instrument is equipped with standard tools for sample preparation, as well as with a LEED and TPD setup for surface characterization. The sample may be heated to ∼1400 K by electron bombardment and cooled to ∼90 K by filling the manipulator rod with liquid N_2. The temperature was measured with a K type thermocouple spot-welded to the sample edge. For H depth profiling by NRA, the

sample was irradiated with an energy-filtered (ΔE = 3 keV) beam of $^{15}N^{2+}$ ions close to the resonance energy of the $^{1}H(^{15}N, \alpha\gamma)^{12}C$ nuclear reaction (E_{res}=6.385 MeV). γ-rays emitted in the reaction were detected using a γ-ray scintillation detector (BGO, Oken) located behind the sample. The setup was calibrated with a Kapton foil of known H content as a reference sample.

2.5 Materials

Chemicals were typically used as purchased. In the main experimental setup, all gases were supplied by a common gas line, in which a cooling trap (liquid N_2) could be inserted.

Chemical	Supplier	Purity
Ar	Linde	6.0 (99.9999%)
Ce foil	Alfa Aesar	3.0 (99.9%)
Ce rods	Alfa Aesar	3.0 (99.9%)
CO	Linde	4.7 (99.997%)
CO_2	Linde	4.5 (99.995%)
D_2	Linde	5.0 (99.999%)
H_2	Linde	6.0 (99.9999%)*
He	Westfalen	5.0 (99.999%)
O_2	Linde	5.0 (99.999%)
$^{18}O_2$	Aldrich Chemistry	2.0 (99%)
Propane	Aldrich Chemistry	3.5 (99.95%)
Propene	Linde	2.8 (99.8%)
Propyne	Linde	1.7 (97%)
Synthetic Air	Westfalen	5.0 (99.999%)

Table 2.1: Suppliers and purity of the chemicals used in the experiments.

*H_2 used for NRA experiments was further purified using a Pd membrane diffusion purifier (P+E 2001), resulting in ultra-pure H_2 (purity 9, 99.9999999%).

2.6 $CeO_2(111)$ and $CeO_{2-x}(111)$ Thin Films

2.6.1 Preparation

The $CeO_2(111)$ thin films used in the following experiments were prepared according to an established recipe,[93, 94] which was slightly adapted. Ru(0001) was used as a substrate for epitaxial growth, since this material sustains high temperatures and can be easily cleaned from impurities by repeated cycles of Ar^+ sputtering, oxidation in $\sim 1\times10^{-6}$ mbar O_2 at 1000 K, and annealing to 1250 K in UHV. To improve adhesion between $CeO_2(111)$ and the substrate, the Ru(0001) surface was exposed to $\sim 1\times10^{-6}$ mbar O_2 at 1000 K to form a $3O(2 \times 2)$ superstructure. Attempts to grow CeO_2 onto bare Ru(0001) often resulted in amorphous structures, which did not produce distinguishable LEED patterns.

The growth of $CeO_2(111)$ onto the $3O(2 \times 2)$-Ru(0001) surface proceeded in three steps. First, we evaporated Ce in an O-rich atmosphere ($\sim 1\times10^{-6}$ mbar O_2) onto the substrate kept at 100 K. This growth step at low temperature ensured that the film grew as a continuous layer. After the film was sufficiently thick (clear $CeO_2(111)$ spots visible in LEED), we continued evaporation in a second step while the sample temperature was raised from 100 K to 673 K (1 K/s). In a third step, we continued the growth at 673 K until we reached the desired film thickness. In between steps (or after max. 45 min of evaporation), we annealed the sample at 1000 K to smooth the $CeO_2(111)$ film and increase its crystallinity.

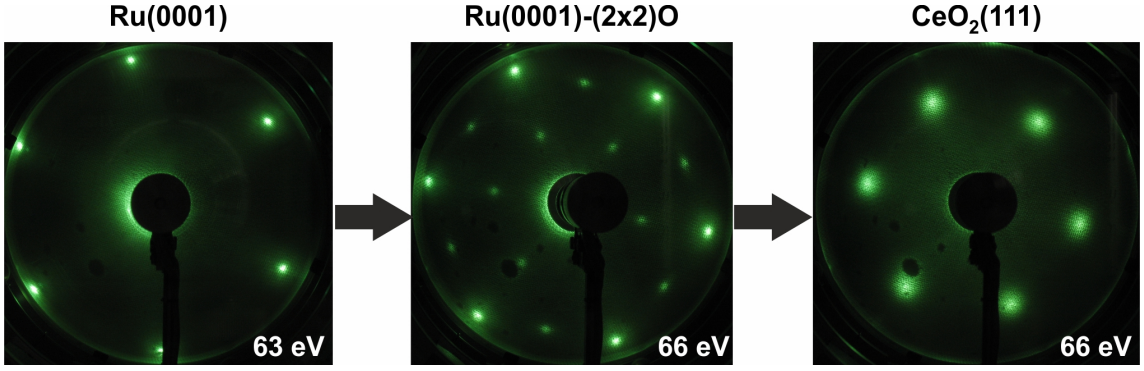

Fig. 2.13: LEED patterns obtained during different stages of $CeO_2(111)$ thin film growth. From left to right: clean Ru(0001), $3O(2\times2)$-Ru(0001), 4-6 nm thick $CeO_2(111)$ thin film on top of $3O(2 \times 2)$-Ru(0001).

To obtain reduced $CeO_{2-x}(111)$, we annealed the $CeO_2(111)$ film in UHV at 1200-1250 K for 20-40 min, depending on the film thickness. The reduction was fully

reversible when $CeO_{2-x}(111)$ was exposed to $p(O_2)=1\times10^{-6}$ mbar at 1000 K for 15 min.

2.6.2 Characterization

Representative LEED patterns and XP spectra of the $CeO_2(111)$ and $CeO_{2-x}(111)$ thin films are shown in Fig. 2.14.

$CeO_2(111)$ films showed a hexagonal LEED pattern, corresponding to a (1.4×1.4) lattice with respect to the (1×1) pattern of the Ru(0001) substrate. The pattern consisted of sharp spots in a low intensity background, indicating long-range order of the films. The absence of substrate spots shows that the $CeO_2(111)$ films are continuous and sufficiently thick, so that a large influence of the substrate on the reactivity of the oxide surface can be excluded. The continuity of the film was additionally probed with CO titration in IRAS, where (if not stated otherwise) no characteristic vibrational features of CO/Ru(0001) were apparent. The continuity of the films was repeatedly checked in between experiments.
Reduced $CeO_{2-x}(111)$ thin films showed a LEED pattern with $(\sqrt{7}\times\sqrt{7})$ reconstruction. We assign this structure to an ordered array of O vacancies on the $CeO_{2-x}(111)$ surface (see section 1.4).[23, 33, 34] The $(\sqrt{7}\times\sqrt{7})$ pattern was only visible on perfectly clean $CeO_{2-x}(111)$ surfaces and vanished when the sample was left in UHV for several hours, due to the adsorption of water from the UHV background. The presence of the $(\sqrt{7}\times\sqrt{7})$ pattern, which was verified before every experiment, was thus an indicator for the cleanliness of the surface.

XP spectra of the oxide films were recorded in normal emission geometry ($\Theta = 0°$) and grazing emission geometry ($\Theta = 60°$). The probing depth for CeO_2 is ∼3 nm in normal mode and ∼1.5 nm in grazing mode, estimated as 3λ (see section 2.2.3). The thickness of the films, estimated from the attenuation of the Ru 3d XP signal, is ∼4-6 nm. All observed features in O 1s and Ce 3d XP spectra are consistent with previous studies and typical for stoichiometric or reduced ceria surfaces.[25, 95–100] For a detailed overview of Ce 3d peak positions and fitting parameters, please refer to Table 7.1 in the Appendix.

For $CeO_2(111)$, XPS shows features in the same intensity ratio in both emission geometries, indicating that the chemical composition remains unchanged throughout the depth of the film. The Ce 3d spectra have a complex structure of six overlapping peaks, which are characteristic for Ce^{4+} ions. Due to spin-orbit splitting, the

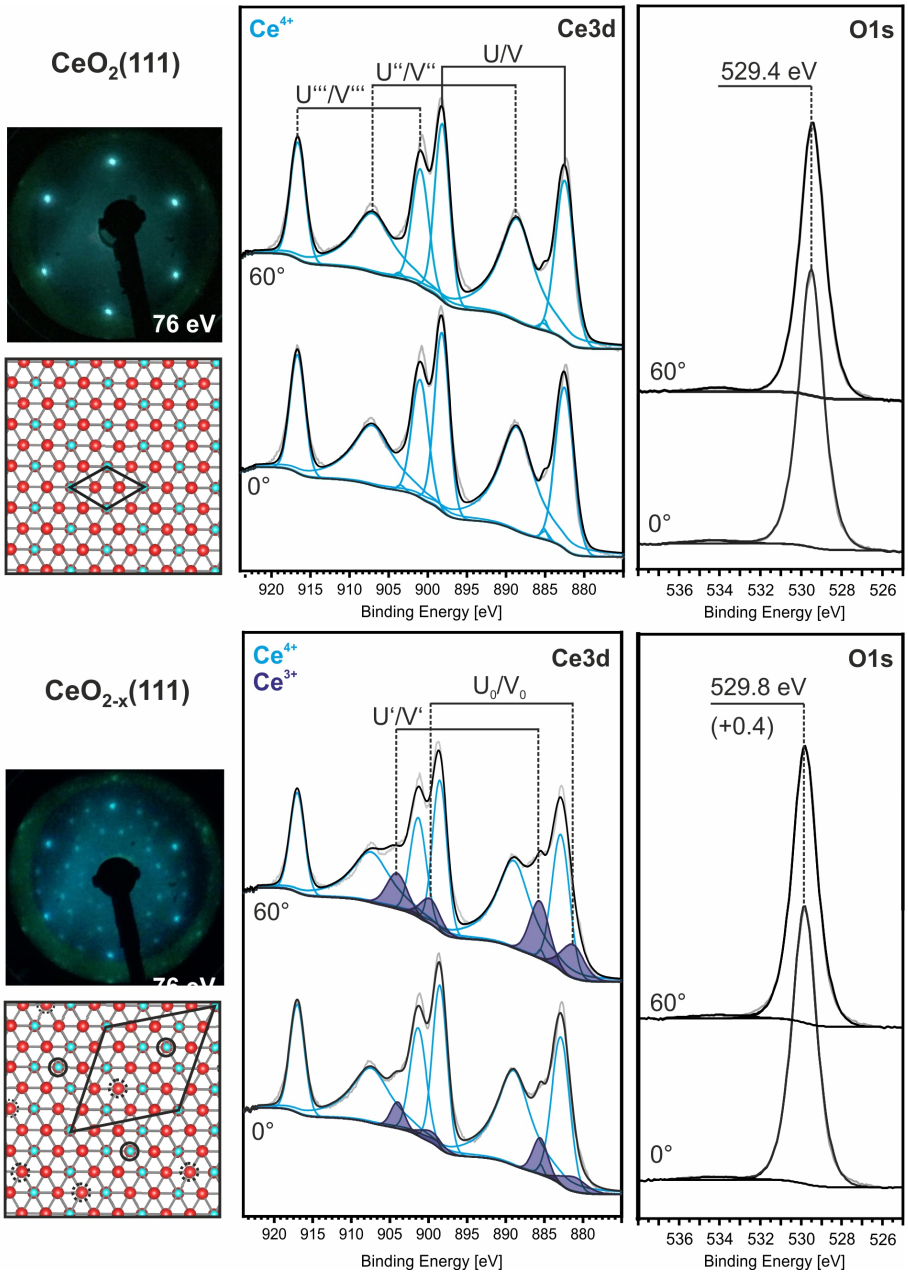

Fig. 2.14: $CeO_2(111)$ and $CeO_{2-x}(111)$ thin films: typical LEED patterns, corresponding surface structure (top view) with unit cell and O vacancies indicated, and typical Ce 3d and O 1s XP spectra (recorded in grazing emission (60°) and normal emission (0°), normalized to the total area under the curves).

3d core level gives rise to features of two different energies, i.e. the $3d_{3/2}$ and $3d_{5/2}$ states. Additionally, a strong interaction between Ce^{4+} ions and O^{2-} ions further splits these levels: In a 'shake down' process, electrons may be transferred from filled O 2p levels into the empty Ce 4f level, resulting in spin-orbit split pairs of three possible final states ($4f^0$, $4f^1$, $4f^2$).[101, 102] Peaks arise at binding energies of 916.7/898.2 eV (U"'/V"' after established nomenclature[95]), 907.1/888.7 eV (U"/V"), and 901.0/882.6 eV (U/V). The detailed assignment of these peaks to the final states is still under debate.[103, 104]
O 1s spectra were dominated by a main peak at ∼529.4 eV, which is assigned to O^{2-} ions in CeO_2. Occasionally, a very weak feature at ∼534 eV indicated the presence of few defective surface sites.[105, 106]

For reduced CeO_{2-x}(111), Ce 3d XPS featured peaks of Ce^{4+} and Ce^{3+} ions.[25, 95–97, 100] Comparable to the Ce^{4+} features, Ce^{3+} species give rise to two pairs of XPS peaks, due to spin-orbit splitting and possible electron transfer from the O^{2-} ions, at 904.1/885.6 eV (U'/V'), and 899.8/881.4 eV (U_0/V_0). The Ce^{4+} peaks were shifted to slightly higher binding energies (+0.3 eV) as compared to the spectra for CeO_2(111), while the Ru 3d peak, which was used as a reference, remained unchanged in BE. Spectra recorded in grazing emission geometry showed a larger contribution of Ce^{3+} features as compared to spectra in normal emission geometry, which indicates a larger density of Ce^{3+} ions close to the oxide surface. From the total area A of Ce^{4+} and Ce^{3+} species, we calculate the degree of reduction of the thin film according to the density of Ce^{3+} ions:

$$c(Ce^{3+}) = \frac{A(Ce^{3+})}{A(Ce^{3+}) + A(Ce^{4+})} \tag{2.38}$$

The density of Ce^{3+} ions varied from preparation to preparation, but was typically in the order of 20% in grazing emission mode and 10% in normal emission mode.
O 1s XPS showed the same features as for CeO_2(111), albeit with a slight shift of the main peak to higher binding energies (+0.4 eV), as it has been reported in previous literature.[107]

3 Hydroxylation of CeO_2(111)

Hydroxyl (OH) groups on CeO_2 are involved as intermediates in numerous catalytic reactions.[7, 10] Especially when CeO_2 is used as a catalyst in the selective hydrogenation of alkynes, OH groups are believed to play an essential role in the oxide's reactivity.[14, 108] To understand the catalytic performance of CeO_2, it is essential to understand the adsorption environment and stability of hydroxyl groups on the CeO_2 surface, which we investigate in the following.

3.1 Literature Survey

The formation of OH groups on CeO_2(111) is rather difficult under UHV conditions. While no hydroxyls are formed by exposure to molecular H_2 at low pressures,[27, 99, 109] hydroxylation of CeO_2(111) has been achieved via two approaches, i.e. (i) dissociation of water on reduced CeO_{2-x}(111)[98, 99, 110, 111] and (ii) adsorption of atomic H onto CeO_2(111).[52, 99] Results of previous experimental and theoretical studies are summarized in this section. For simplification, hydrogen of both isotopes (H and D) will be denoted as *H* in the following.

3.1.1 Dissociation of H_2O on CeO_{2-x}(111)

O vacancies on reduced CeO_{2-x}(111) strongly interact with H_2O, in contrast to the largely unreactive CeO_2(111) surface.[98, 99, 111–116] H_2O dissociates into an OH group (HO^w in the following, to mark its origin from water) that fills an O vacancy (□) and to a H species that forms an OH group by binding to a surface O ion. The oxidation state of the surface stays unchanged during this process:[111, 113, 116]

$$H_2O^w(g) + \square + O^{lattice} \longrightarrow HO^w_{ads} + HO^{lattice}_{ads} \tag{3.1}$$

Both hydroxyls are coordinated to three underlying Ce ions and have a surface-normal orientation (see Fig. 3.1).
When heated, surface OH groups recombine and desorb via two different pathways - by associative desorption as H_2O (eq. 3.2), or by production of H_2 (eq. 3.3). The oxidation state of the surface stays unchanged for the first desorption reaction, while it changes to a more oxidized state in the second:

$$2\,OH_{ads} \rightarrow H_2O\,(g) + \square + O^{lattice} \tag{3.2}$$

$$2\,OH_{ads} + 2\,Ce^{3+} \rightarrow H_2(g) + 2\,O^{lattice} + 2\,Ce^{4+} \tag{3.3}$$

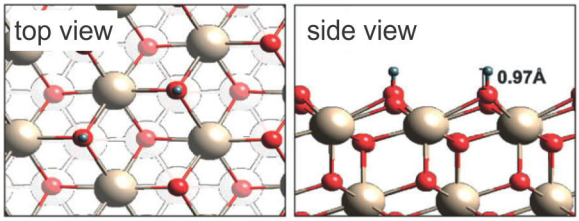

Fig. 3.1: Computed geometries of OH groups formed by dissociation of H_2O on $CeO_{2-x}(111)$ (top and side view). O shown in red, Ce in brown, H in gray. Reproduced from [113] with permission from the PCCP Owner Societies.

Desorption of OH takes place via both reaction pathways between 450 K and 650 K (see Fig. 3.2a+b).[99, 110, 112, 117] The desorption of OH as H_2, which partially re-oxidizes the oxide surface, is favored at high O vacancy densities.[99, 115, 117–119].

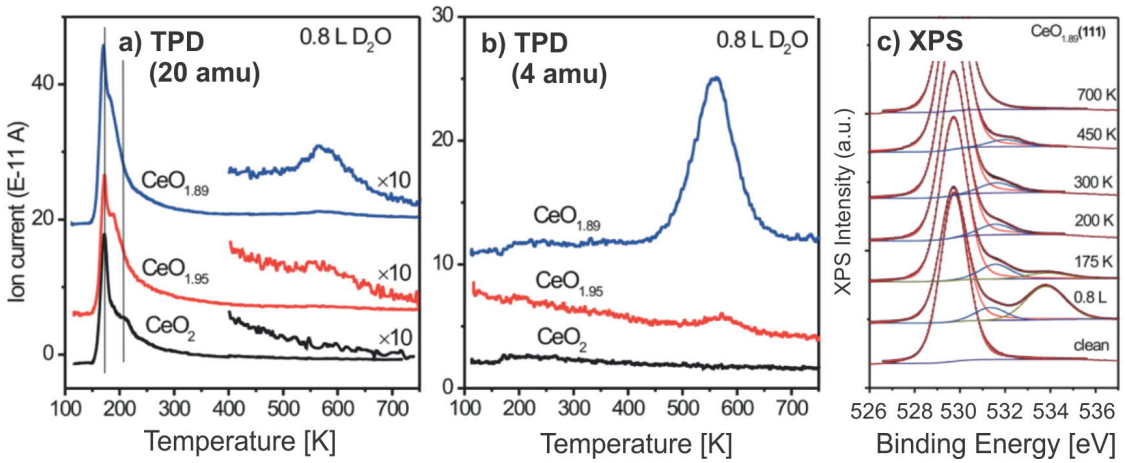

Fig. 3.2: a) D_2O- and b) D_2-TPD traces recorded after exposing $CeO_2(111)$ and $CeO_{2-x}(111)$ to 0.8 L D_2O at 115 K, c) O 1s XP spectra of $CeO_{2-x}(111)$ after exposure to 0.8 L D_2O at 115 K and subsequent annealing. Adapted with permission from [99]. Copyright 2013 American Chemical Society.

Water may also adsorb molecularly on top of Ce^{4+} ions. In contrast to $CeO_2(111)$, theoretical studies suggest that H_2O_{ads} species on $CeO_{2-x}(111)$ do not form H bonds to surface O ions, which results in a lowered adsorption energy.[99, 114]

O 1s XPS features at ∼531.4-531.5 eV and ∼533.8-534.0 eV (see Fig. 3.2c) have been assigned to surface hydroxyls and molecular H_2O_{ads}, respectively.

3.1.2 Atomic H on CeO_2(111) and CeO_{2-x}(111)

Since H_2 does not dissociate under low pressure conditions on CeO_2(111), the only other route to hydroxylation is the adsorption of atomic H species. Experimentally, dissociation of H_2 is realized by flowing H_2 gas through a heated capillary or over a glowing filament. Dissociation may lead to different H species, e.g. H^+ or $H^\bullet$, which are usually summarized under the term *atomic H*.

Atomic H on CeO_2(111)

The adsorption of atomic H onto CeO_2(111) results in the exothermic formation of surface hydroxyls (OH_{ads}). With every OH group forming, a single nearest neighbor Ce^{4+} ion is reduced to Ce^{3+}:[99, 120–122]

$$O^{lattice} + H(g) + Ce^{4+} \longrightarrow HO^{lattice}_{ads} + Ce^{3+} \tag{3.4}$$

OH groups formed by adsorption of H on CeO_2(111) are similar in structure and orientation to hydroxyls formed by water dissociation over O vacancies (see Fig. 3.1), with the added characteristics that the hydroxylated O atom protrudes outwards from its original lattice position.[52, 120–122] Scanning probe microscopy studies and theoretical simulations have reported that OH groups may be stabilized on the surface in trimers even at low coverages.[14, 52]

Identification of OH groups by vibrational spectroscopy is still controversial, since most experimental studies have been performed on ill-defined CeO_2 powder surfaces.[107, 123–128] Table 3.1 gives an overview of computationally predicted ν(OH) frequencies.

ν(OH) [cm^{-1}]	Reference
3627	Fabris et al., 2006[120]
3650, 3641	Lin et al., 2007[129]

Table 3.1: Computed OH stretching frequencies on CeO_2(111).

At high OH coverage, H_2O_{ads} species form in addition:[52, 99]

$$HO^{lattice}_{ads} + H(g) \longrightarrow H_2O^{lattice}_{ads} \tag{3.5}$$

OH groups on CeO_2(111) desorb preferentially as H_2O (see eq. 3.2) over a broad temperature range between 200 K and 650 K (see Fig. 3.3a).[99] This reaction produces an O vacancy on the surface and leaves the sample in a partially reduced state.

The ability of atomic H to remove O species from $CeO_2(111)$ surfaces by desorption of water has been verified computationally.[121, 122] Desorption of OH groups as H_2 (see eq. 3.3 and Fig. 3.3b) has been reported around ∼440 K, but to a much smaller extent. H_2O_{ads} is less stable and desorbs at ∼200 K.[99]

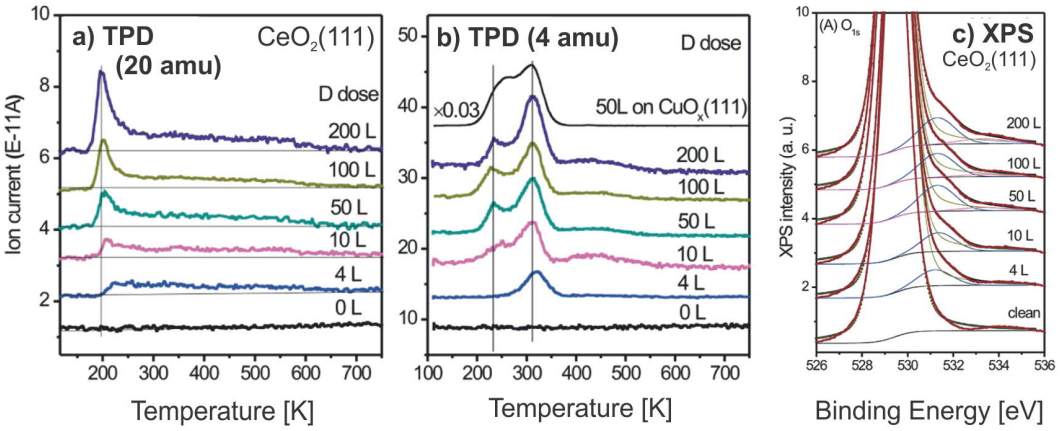

Fig. 3.3: a) D_2O- and b) D_2-TPD traces recorded after exposing $CeO_2(111)$ to atomic D at 115 K, c) O 1s XP spectra after exposure of $CeO_2(111)$ to atomic D at 115 K. Adapted with permission from [99]. Copyright 2013 American Chemical Society.

Atomic H on $CeO_{2-x}(111)$

As on $CeO_2(111)$, adsorption of atomic H onto reduced $CeO_{2-x}(111)$ leads to the formation of surface OH groups (however, in slightly smaller concentration). The formation of chemisorbed H_2O_{ads} species is largely suppressed.[99] Surface hydroxyls desorb as H_2O (see eq. 3.2) in a range between 200-450 K and around ∼575 K or as H_2 (see eq. 3.3) at ∼570 K.[99] The presence of O vacancies on the surface promotes OH desorption via the H_2 pathway, during which the surface is partially re-oxidized.

3.2 Atomic H/$CeO_2(111)$

To investigate the adsorption behavior of H on $CeO_2(111)$, we exposed the $CeO_2(111)$ thin film to H_2 gas, which was in part dissociated over a nearby glowing filament (thoriated W). No hydroxyls were formed up to H_2 pressures of 1×10^{-2} mbar when the filament was deactivated. The exact dissociation efficiency of the filament is unknown, but increases with the H_2 pressure (see Fig. 3.4), denoted as $p(H/H_2)$ in the following.

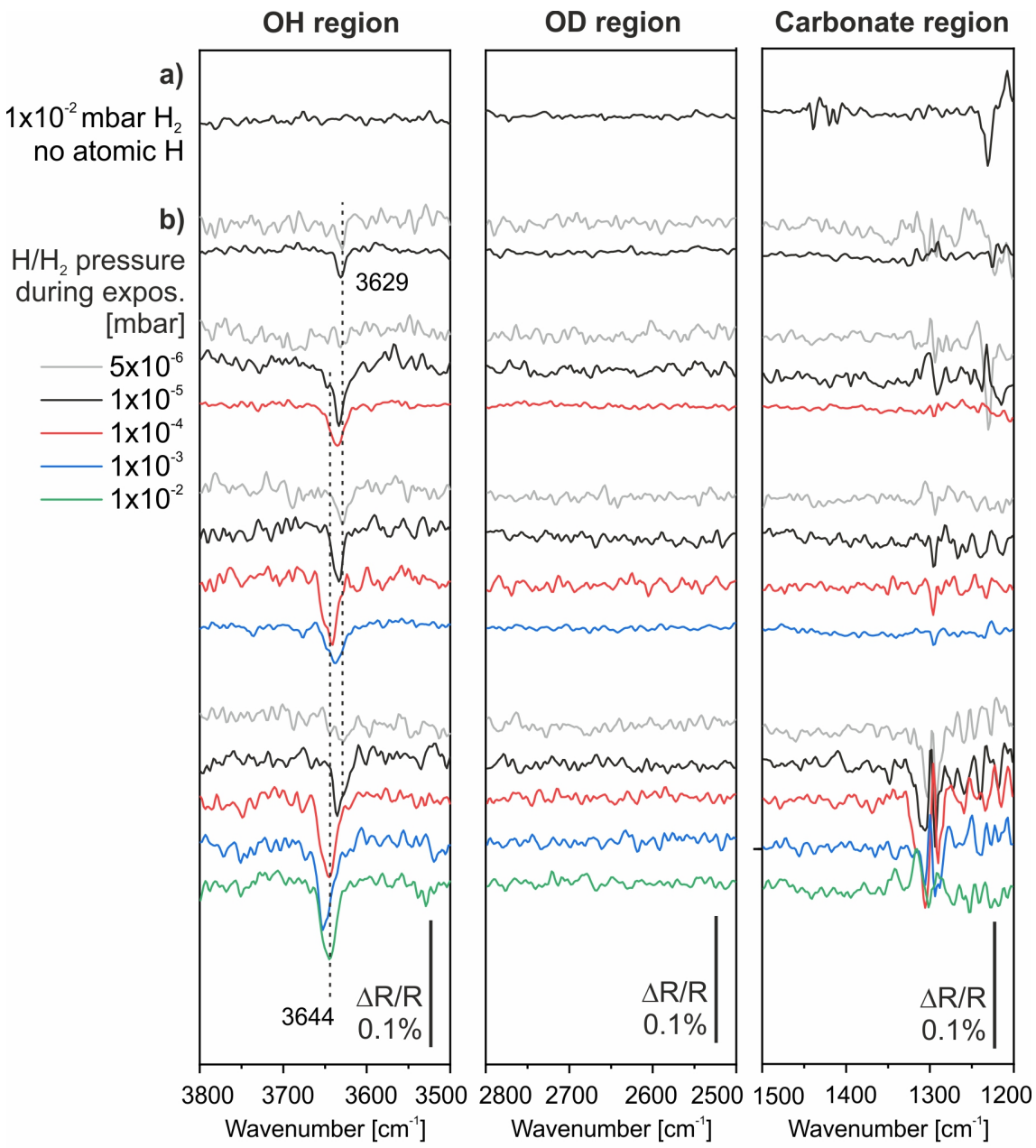

Fig. 3.4: IRAS spectra recorded at 473 K during exposure of $CeO_2(111)$ to a) 1×10^{-2} mbar H_2 (filament deactivated), b) various pressures of H/H_2 (filament activated).

3.2.1 Formation of OH

Fig. 3.4 shows IRAS spectra recorded during exposure of $CeO_2(111)$ to different pressures of H/H_2 at 473 K. With increasing pressure, vibrational features appear in the ν(OH) frequency region, indicating that hydroxyls form on the $CeO_2(111)$ surface. At low H/H_2 pressures up to 1×10^{-5} mbar, a single vibrational band at 3629 cm^{-1} arises. At higher pressures, the OH band shifts to a higher frequency of 3644 cm^{-1}. No other features appear in the spectrum, showing that the $CeO_2(111)$ surface stays clean of impurities.

The frequency of the ν(OH) vibration at low coverage (3629 cm^{-1}) is in almost perfect agreement with the theoretically predicted value of 3627 cm^{-1} for an isolated hydroxyl group on $CeO_2(111)$.[120] We thus assign this band to an OH group coordinated to a single Ce^{3+} and two Ce^{4+} ions ($OH(1Ce^{3+},2Ce^{4+})$). In the following, we will refer to this configuration as *OH(I)*. The shift of the OH band to higher frequencies (3644 cm^{-1}) at high coverage might be explained by an increasing concentration of Ce^{3+} when more and more OH groups or O vacancies are formed on the surface. Previous studies report a similar frequency shift at increasing O vacancy concentration.[39, 107, 118]

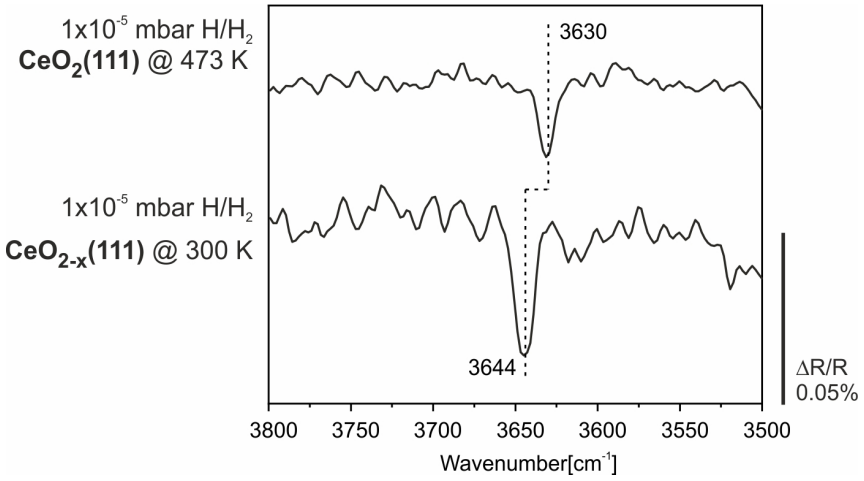

Fig. 3.5: IRAS spectra recorded during exposure of $CeO_2(111)$ (at 473 K) and $CeO_{2-x}(111)$ (at 300 K) to 1×10^{-5} mbar H/H_2.

We tested this hypothesis by exposing a reduced $(\sqrt{7}\times\sqrt{7})$-$CeO_{2-x}(111)$ film to low pressures (1×10^{-5} mbar) of H/H_2 (see Fig. 3.5). A sample temperature of 300 K was chosen to minimize the formation of additional O vacancies via water desorption. Indeed, upon H adsorption, the low-coverage OH band appears at higher frequency on $CeO_{2-x}(111)$ (3644 cm^{-1}), as compared to $CeO_2(111)$ (3629 cm^{-1}). We

assign the band at 3644 cm^{-1} to a hydroxyl group neighboring two Ce^{3+} species (OH($2Ce^{3+}$,$1Ce^{4+}$)), or *OH(II)*.

In the scope of our studies, Dr. Thomas Kropp, Dr. Joachim Paier, and Prof. Joachim Sauer at the Humboldt University Berlin performed DFT+U calculations on the vibrational stretching frequency of OH groups in different configurations. Details on the computational methodology may be found in reference [130]. In agreement with our results, they find that the stretching frequency of an OH group will increase with the number of Ce^{3+} ions in its vicinity (see Fig. 3.6).

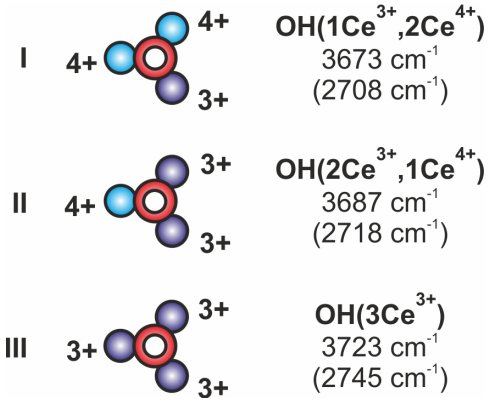

Fig. 3.6: Computed vibrational stretching frequencies (scaled) of isolated surface OH (OD) groups on CeO_2(111). H (D)=white, O=red, Ce^{4+} (Ce^{3+})=light (dark) blue. Adapted with permission from [130]. Copyright 2017 American Chemical Society.

3.2.2 OH Stability in UHV

To investigate the stability of the OH species in UHV, we cooled the sample to 200 K in H/H_2, and subsequently removed the H/H_2 gas phase. The temperature was chosen in order to prevent physisorption of water from the background onto the oxide surface. IRAS spectra recorded during this procedure are shown in Fig. 3.7.

For low exposure pressure (1×10^{-5} mbar H/H_2), the OH vibrational band at 3629 cm^{-1} is preserved. At intermediate pressures (1×10^{-4}-1×10^{-3} mbar H/H_2), the OH band shifts to 3629 cm^{-1} upon cooling and loses intensity in benefit of an arising feature at 3594 cm^{-1}. Subsequent removal of the H/H_2 gas has no additional effect. After high pressure exposure (1×10^{-2} mbar), the high frequency band at 3644 cm^{-1} stabilizes at 200 K with a shoulder on the lower frequency side. This shoulder gains in intensity and becomes distinguishable at 3629 cm^{-1} when the H_2 gas is pumped out.

During the cooling and pumping process, the $CeO_2(111)$ surface stays largely free of impurities. Only after exposure to 10^{-2} mbar H/H_2 are vibrational bands visible below 1500 cm^{-1}. These features indicate the presence of adsorbed CO_2 species, which may potentially interact with OH groups. A *reactive* interaction between OH and adsorbed CO_2 to form formates or bicarbonates can be excluded due to the absence of their characteristic vibrations (ν(C-H)=2950-2750 cm^{-1}, and δ(COH)=1250-1180 cm^{-1}, respectively).[131, 132] A more detailed investigation on the nature of adsorbed CO_2 may be found in chapter 5.

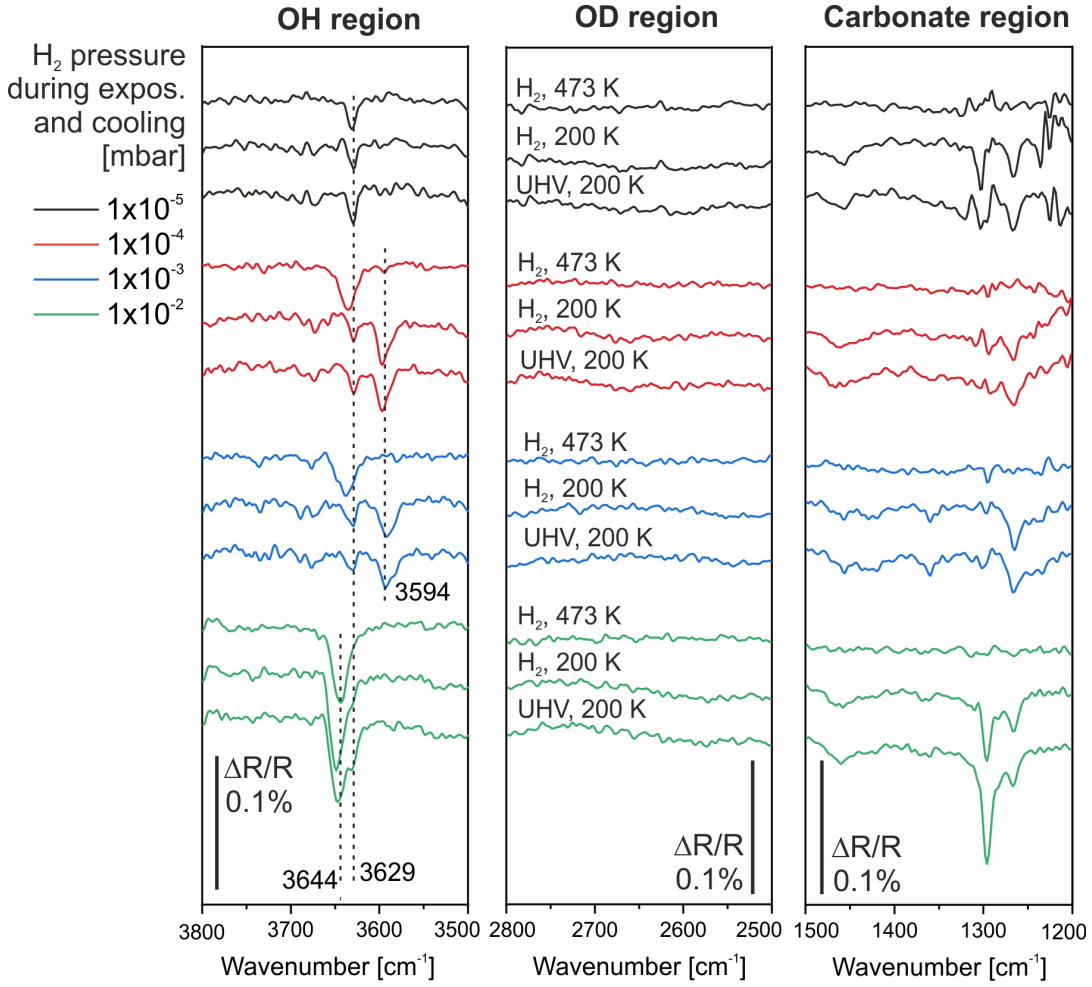

Fig. 3.7: Stability of OH species on $CeO_2(111)$: in H/H_2 at 473 K at different pressures, in H/H_2 at 200 K, in UHV at 200 K.

Applying the assignments made in the previous section, the OH(I) species (3629 cm^{-1}) persists on the $CeO_2(111)$ surface at 200 K in UHV. The stability of the OH(II) band (3644 cm^{-1}), however, seems to depend on the H/H_2 pressure during exposure. After intermediate exposure (1×10^{-4}-1×10^{-3} mbar), the OH(II) species vanishes, which causes an apparent frequency shift and intensity decrease of the OH signal (gener-

ated by the overlap of OH(I) and OH(II) features). At the same time, a new species with a vibrational frequency of 3594 cm^{-1} appears. Vibrational bands in this region are usually associated with H-bonded species,[133, 134] We therefore assign this band to weakly-absorbed H_2O_{ads}.
After exposure to 1×10^{-2} H/H_2, both OH(I) and OH(II) species are stabilized in UHV at 200 K. The simultaneous appearance of their vibrational features supports their assignment to two OH groups in different environments as opposed to a frequency shift caused by adsorbate-adsorbate interactions. The absence of the feature for H_2O_{ads} at 200 K may be explained by the presence of O vacancies on the oxide surface, which form if OH groups recombine and desorb as H_2O. O vacancies, as has been described previously, destabilize the chemisorbed H_2O_{ads} species and decrease their desorption temperature below 200 K.[99]

Indeed, a comparative experiment using D/D_2 shows that O vacancies are produced on the CeO_2(111) surface at 473 K (see Fig. 3.8). From an exposure pressure of 1×10^{-6} mbar D/D_2 on, a vibrational band arises at 2672 cm^{-1}, which we assign to OD($1Ce^{3+}$,$2Ce^{4+}$) (OD(I)) in agreement with the atomic H experiments. Similarly to the H/H_2 experiments, this band shifts to higher frequency (2683 cm^{-1}) with increasing exposure pressure. Starting from 1×10^{-4} mbar D/D_2 exposure, an additional weak OH band appears around ~3641 cm^{-1}. As soon as an exposure pressure of 1×10^{-2} mbar is reached, this band clearly gains in intensity, while the intensity of the OD band decreases. Since no atomic H is supplied here, the only possible way to form OH is dissociation of background water (H_2O) over O vacancies, which are created at high exposure pressure: OD species recombine or react with atomic D and subsequently desorb as D_2O, leaving behind O vacancies, which may then be filled by background H_2O. This phenomenon also explains the intensity decrease of the OD band at 1×10^{-2} mbar D/D_2 exposure.

XP spectra recorded at 200 K after exposure to H/H_2 (see Fig. 3.9) confirm the formation of hydroxyls on the surface as well as the formation of O vacancies at high exposure pressure. In the O 1s region, a shoulder to the main O^{2-} peak appears at ~531.7 eV, which can be assigned to OH species.[52, 99] The absence of a high BE signal, which would be expected to arise from chemisorbed H_2O_{ads}, may be attributed to the species' low concentration or to beam-induced desorption.
With increasing H/H_2 exposure pressure, the OH feature gains in intensity. This shows, in agreement with the IRAS data, that the OH density on the CeO_2(111) surface increases the more H is supplied. Following the same trend, the Ce^{3+} con-

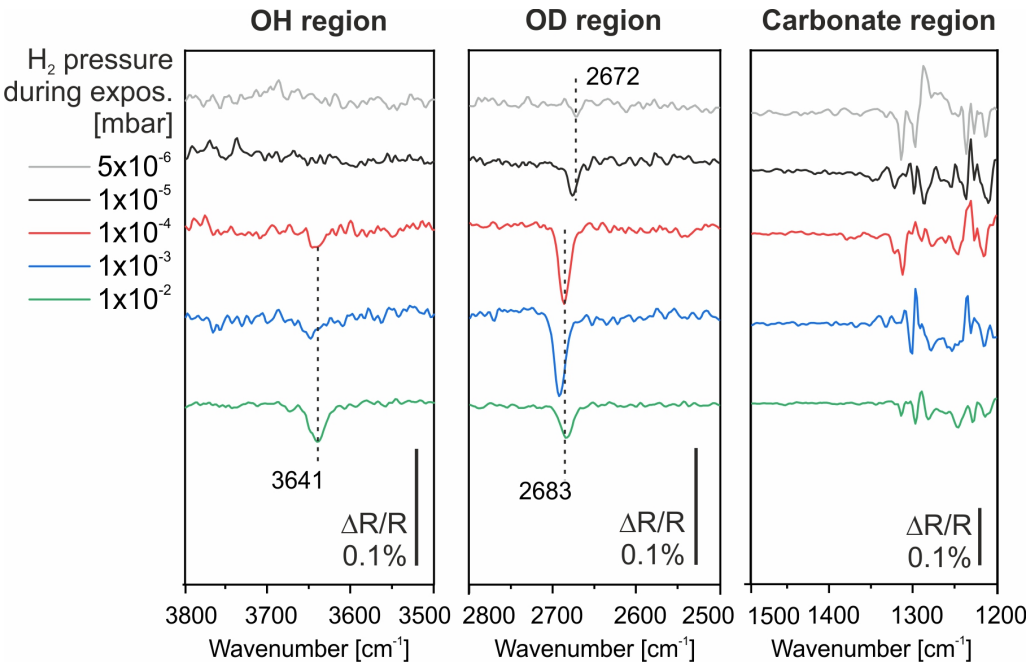

Fig. 3.8: Pressure-dependent formation of OD and OH species on $CeO_2(111)$ during exposure to D/D_2 at 473 K, followed by IRAS.

centration increases with the exposure pressure. For low exposure pressures, the concentration of Ce^{3+} species increases proportionally to the concentration of surface hydroxyls (see Fig. 3.9). After exposure to 1×10^{-2} mbar H/H_2, however, the increase in Ce^{3+} clearly surpasses the increase in OH signal, which is another indication for the formation of O vacancies.

3.2.3 Thermal Stability of OH

In further experiments, we investigated the thermal stability of OH groups by TPD, XPS, and temperature-programmed (TP-)IRAS.

TPD curves (Fig. 3.10) were recorded after exposure to H/H_2 (see Fig. 3.7). Desorption of H_2O occurs continuously over a broad temperature range between 200 K and 600 K. Three main desorption signals are distinguishable at ~260 K, ~330 K, and ~540 K. Weak desorption features of H_2 arise at ~330 K and ~560 K.
The H_2O desorption feature at 260 K is strongest in intensity after intermediate exposures, which links it to molecular H_2O_{ads}. This assignment is supported by the peak's narrow width, which points towards first-order desorption. A recent theoretical study identifies this band as desorption of H_2O from a (OH-H_2O) dimer structure.[135] Water desorption at higher temperature results from recombination of hydroxyls on the surface[99] (2^{nd} order desorption), which we assign to the features

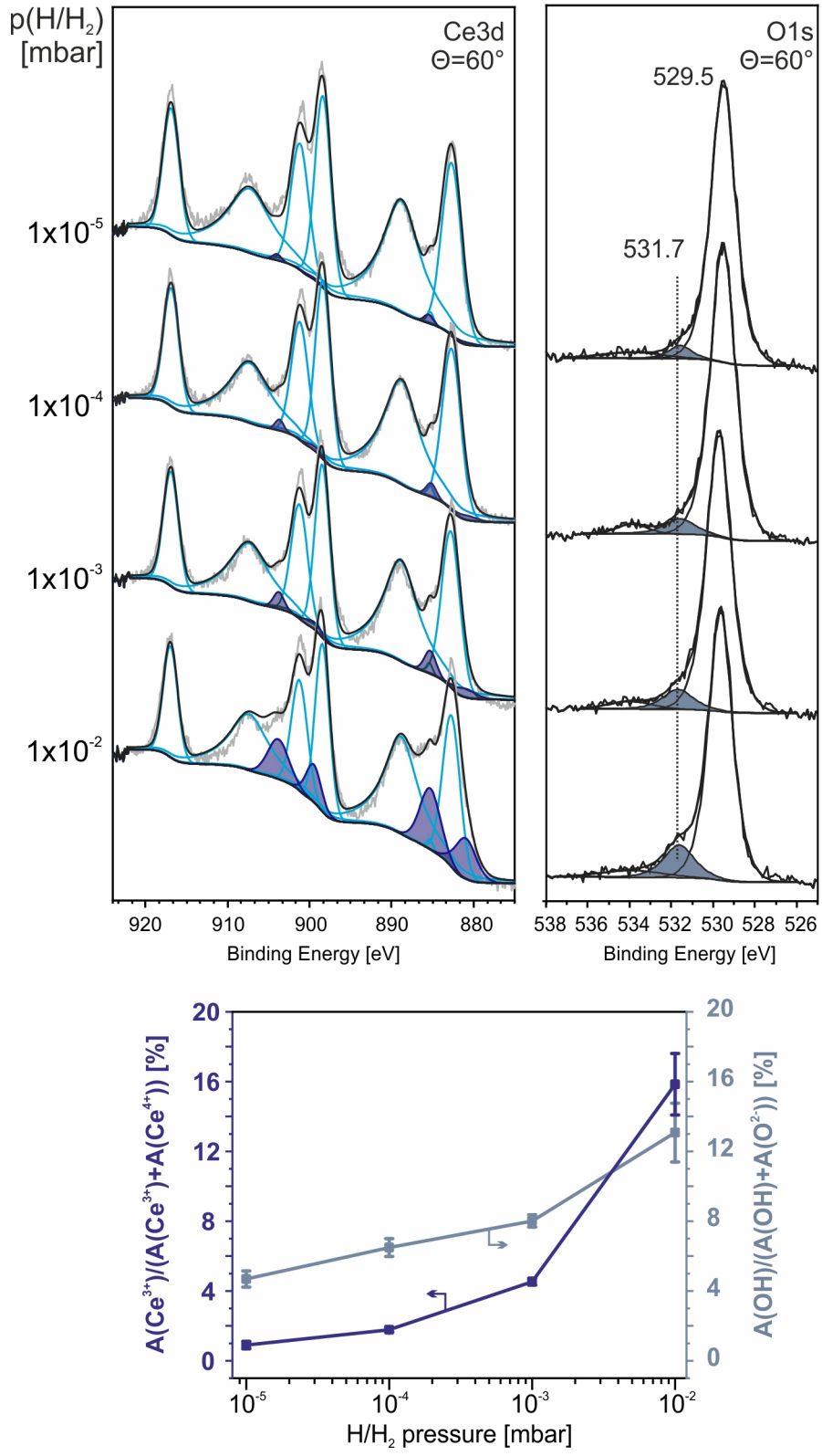

Fig. 3.9: Above: Grazing emission Ce 3d and O 1s spectra (200 K, $\Theta = 60°$) of $CeO_2(111)$ after exposure to different pressures of H/H_2. Below: Relative concentration of Ce^{3+} and OH as a function of H/H_2 exposure pressure.

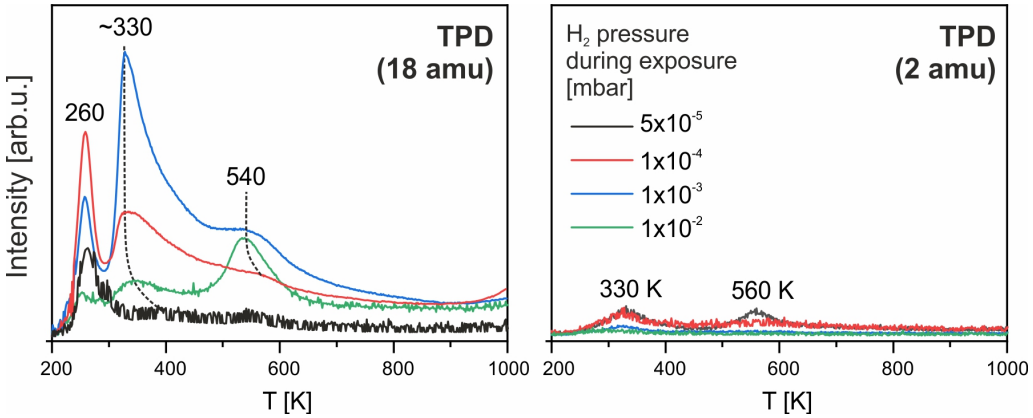

Fig. 3.10: TPD curves for 18 amu (H_2O) and 2 amu (H_2), recorded after exposure of $CeO_2(111)$ to different pressures of H/H_2 . Both spectra are shown with the same intensity scale.

at ∼330 K and ∼540 K. Both features are broad and exhibit a shift of the maximum desorption rate to lower temperature with increasing pressure, as expected for 2nd order desorption processes. In agreement with theoretical studies,[116] we explain the appearance of the high temperature desorption feature (∼540 K) by desorption of hydroxyls that are thermodynamically stabilized by O vacancies.

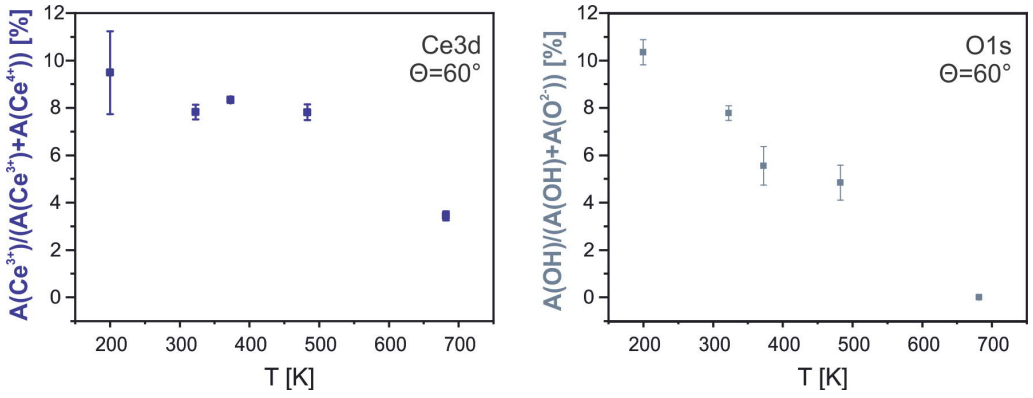

Fig. 3.11: Relative concentration of Ce^{3+} and OH on a hydroxylated $CeO_2(111)$ surface (exp. pressure 1×10^{-2} mbar) in between heating steps in UHV.

To confirms these assignments, we exposed the oxide film to 1×10^{-2} mbar H/H_2 at 473 K, removed the gas phase at 200 K, and subsequently collected XP spectra in grazing emission ($\Theta = 60°$) in between consecutive heating steps in UHV. Fig. 3.11 shows the relative concentration of Ce^{3+} and OH species.
Judging from the XPS data, the amount of hydroxyls is constantly decreasing over

a wide temperature range until it vanishes completely upon heating to 683 K. While the amount of hydroxyls decreases, the amount of Ce^{3+} species stays roughly constant between 200 K and 483 K. A decrease in Ce^{3+} species is only apparent after heating to 683 K. The fact that the concentration of Ce^{3+} species stays constant up to 500 K while the OH concentration decreases, confirms the conclusions drawn from the TPD experiments: OH groups on $CeO_2(111)$ desorb mainly as H_2O, leaving the surface reduction state widely unchanged. The decrease in Ce^{3+} species above 500 K may have various reasons that yet have to be investigated. One possible explanation would be the desorption of OH groups as H_2, which is expected to re-oxidize the oxide surface. TPD curves recorded under the same conditions, however, only show weak H_2 desorption. A different hypothesis has been suggested in a previous study,[99] which tentatively explains the re-oxidation of hydroxylated $CeO_{2-x}(111)$ by diffusion of O species from deeper oxide layers to the surface, which would result in a decreased O vacancy concentration at the surface, and thus apparent re-oxidation. Theoretical studies, however, have shown that O vacancies on $CeO_2(111)$ are more stable on the surface than in the bulk, which rules out this scenario.[38] Another possible scenario, which still needs experimental verification, is diffusion of H species into the CeO_2 film and further towards the Ru substrate, where H could be stabilized at the CeO_2/Ru interface.[136]

Fig. 3.12 shows TP-IRAS spectra recorded during constant heating of a hydroxylated $CeO_2(111)$ surface in UHV. Matching the TPD and XPS experiments, hydroxylation was performed by exposure to 1×10^{-2} mbar H/H_2 at 473 K. After cooling to 200 K, the vibrational bands for OH(I) (3629 cm^{-1}) and OH(II) (3644 cm^{-1}) are clearly distinguishable. A weak band at 1296 cm^{-1} indicates the presence of chemisorbed CO_2. This feature vanishes around 300 K, without changing the frequency of the OH groups, which suggests that OH and chemisorbed CO_2 do not interact strongly. The intensity ratio of the OH bands stays constant up to 313 K. Between 315 K and 373 K, the OH(I) band (3629 cm^{-1}) vanishes. We thus assign desorption of OH(I) to the desorption feature observed in TPD at ∼330 K. The feature for OH(II) at 3644 cm^{-1}, in agreement with the TPD and XPS data, disappears above 523 K, which we link to the TPD desorption peak at ∼540 K.

3.3 Conclusions

Upon exposure to atomic H, OH groups and H_2O_{ads} species form on the $CeO_2(111)$ surface. The amount of OH increases with increasing supply of atomic H. We identify

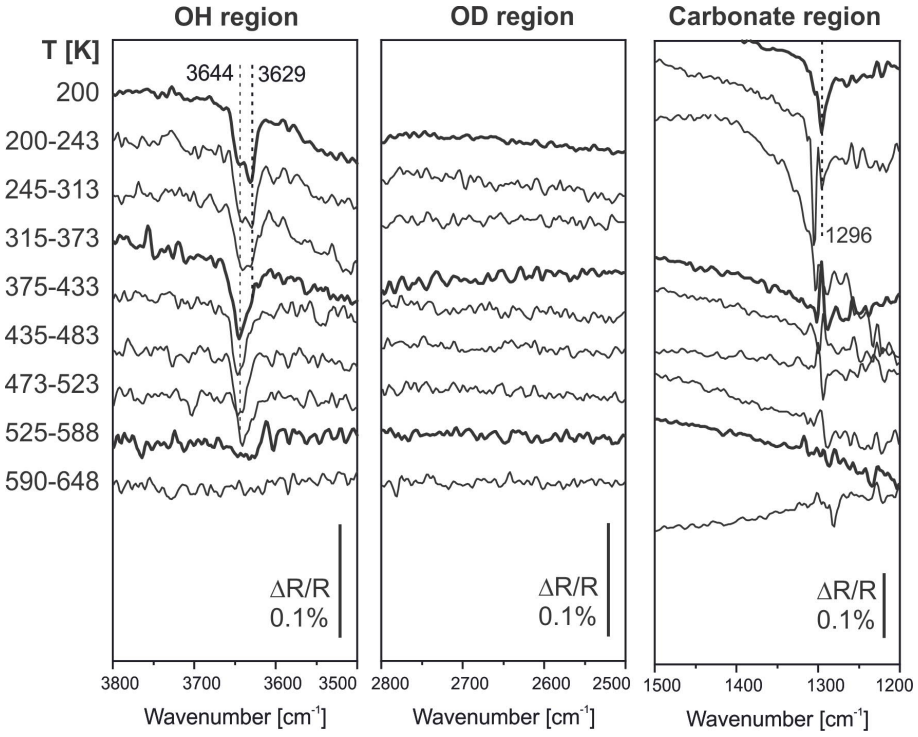

Fig. 3.12: TP-IRAS spectra obtained during heating of a hydroxylated $CeO_2(111)$ surface (exposure pressure 1×10^{-2} mbar H/H_2) in UHV.

the vibrational frequencies and individual stability of two types of surface hydroxyls, OH(I) ($OH(1Ce^{3+},2Ce^{4+})$) and OH(II) ($OH(2Ce^{3+},1Ce^{4+})$), which differ in their coordination environment. Furthermore, O vacancies that form at high OH coverage enable the dissociation of background water. The presence of these vacancies suppresses the formation of molecular H_2O_{ads}.

Surface Species	$\nu(OH)$ [cm^{-1}]	$\nu(OD)$ [cm^{-1}]	$\frac{\nu(OH)}{\nu(OD)}$	Desorption Product, Desorption T [K]
OH(I) ($OH(1Ce^{3+},2Ce^{4+})$)	3629	2672	1.36	H_2O, ~330 K
OH(II) ($OH(2Ce^{3+},1Ce^{4+})$)	3644	2683	1.36	H_2O, ~540 K
H_2O_{ads}	3594	2605	1.38	H_2O, ~260 K

Table 3.2: Summary of vibrational frequencies and desorption characteristics for species formed by exposure of $CeO_2(111)$ to H/H_2 (D/D_2).

4 Interaction of D_2 (H_2) with $CeO_2(111)$ and $CeO_{2-x}(111)$

While the hydroxylation of $CeO_2(111)$ by water or atomic H has been intensely investigated, only few studies have addressed the interaction of H_2 and $CeO_2(111)$. Only recently, fueled by the promising performance of CeO_2 as a catalyst in the selective hydrogenation reaction,[11–13] this research topic has attracted more attention in the scientific community. Understanding the key processes involved - H_2 dissociation on the oxide surface and H incorporation into the bulk - will advance our understanding of the limiting parameters in the selective hydrogenation reaction. This chapter gives an overview of the current state of research on the interaction of H_2 and $CeO_2(111)$ and summarizes our experiments, in which we assess the temperature dependence of the D_2 (H_2) dissociation reaction, the stability of the generated OD (OH) groups, and the role of O vacancies in the incorporation of D (H) species below the CeO_{2-x} surface.

4.1 Literature Survey

Recent theoretical studies have established that H_2 dissociates on the $CeO_2(111)$ surface via a heterolytic pathway.[39, 137–140] These recent results object theoretical studies in the past, which have predicted a homolytic dissociation mechanism,[129] as well as widely varying values for activation barriers, owed mainly to different computational methodologies.[138] The recently established standard method in the community is the so-called *DFT+U* approach, where a Hubbard-like U term is included in the DFT calculation to model the Coulomb interactions of the localized Ce 4f electrons. The exact value of the U term will strongly affect any simulations, and therefore needs to be carefully selected. As of now, an optimal U term of 4.0-4.5 eV has been calibrated with independent functionals.[138]

Fig. 4.1 shows the computed minimum energy path of the heterolytic dissociation reaction as well as atomistic representations along the reaction coordinate. In the course of the reaction, the H_2 molecule physisorbs on the $CeO_2(111)$ surface, which polarizes the H-H bond and thereby activates it for dissociation (state II). Dissociation proceeds on top of a Ce^{4+}-O unit functioning as a Lewis acid-base pair, while an electron of H_2 reduces a Ce^{4+} ion on the oxide surface to Ce^{3+}. The transition

state (III) of the heterolytic dissociation is an OH and Ce^{3+}-H pair. Finally, the H of the Ce-H group moves over to a neighboring O ion. Overall, the dissociation reaction yields two OH groups and two reduced Ce^{3+} species on the surface (IV):

$$H_2\,(g) + 2\,O^{\text{lattice}} + 2\,Ce^{4+} \longrightarrow 2\,HO^{\text{lattice}}_{\text{ads}} + 2\,Ce^{3+} \tag{4.1}$$

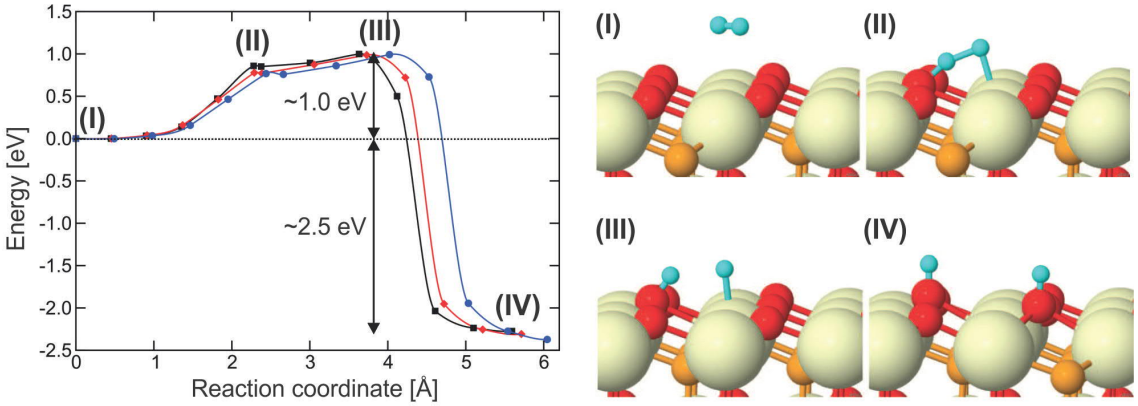

Fig. 4.1: Computationally assessed mechanism for heterolytic dissociation of H_2 on $CeO_2(111)$. Left: reaction energy path for three unit cells of different size (blue: (3×3), red: (2×2), black: ($\sqrt{3}$×1)), right: atomistic representation of the indicated states (1st layer O = red, 2nd layer O = orange, Ce = beige, H = blue). Reprinted from [138] with permission of AIP publishing.

The heterolytic dissociation proceeds through a high activation barrier of ∼1.0 eV per H_2 molecule[14, 137, 139] and is widely unaffected by the hydroxyl coverage or the presence of O vacancies. The net reaction is strongly exothermic.[14, 120, 139, 141]
Due to the large activation barrier involved, H_2 dissociation takes place only at elevated pressures and/or temperatures.[99, 109] Most experimental studies have been performed on ceria powders,[107, 123–128] showing that OH groups form by dissociation above 400 K ($p_{H_2} \geq 1$ bar). These studies, however, suffer from an essential conceptual drawback: powders consist of a complex arrangement of particles with irregular size, surface termination, and defect concentration, which makes it impossible to draw firm conclusions on the reaction mechanism on the atomic scale.

Indeed, studies on CeO_2 nanocrystals have shown that the surface morphology strongly affects the formation of OH groups and O vacancies.[118, 140] On $CeO_2(111)$, H_2 dissociation is a slow, activated process that takes place above 450 K.[118, 140, 142] At higher temperatures, OH groups recombine and desorb as H_2O and/or H_2. Elimination of water from the hydroxylated surface leads to O vacancy formation and

surface restructuring at high temperature. Reduced surfaces with periodic structure, such as CeO_{2-x}(111) in (3×3) and (4×4) periodicity, could be locally stabilized.[142]

The dissociation of H_2 over CeO_2 is a surface-limited process.[124–126, 128] However, H incorporation into the oxide bulk has been occasionally reported in cases where H_2 interacts with reduced CeO_{2-x}.[39, 123, 127]
The mechanism of H incorporation and its limitations have not yet been assessed by comprehensive studies. Among many open questions, the chemical nature of incorporated H remains unclear. Experimental studies have suggested bulk hydrides[123] or OH groups[107] as possible candidates. Computationally, spontaneous formation of bulk OH groups has been predicted in the past,[143] but not yet verified by state-of-the-art DFT+U calculations. A recent experimental study by Wu et al.[39] supports the hydride hypothesis using Inelastic Neutron Scattering (INS), whereby the authors identify surface and bulk Ce-H^- vibrations on CeO_{2-x}. A summary of vibrational features that have been associated with bulk H species is given in Table 4.1.

Bulk OH	Surface Ce-H	Bulk Ce-H	Reference
3414 cm^{-1}			Pennycook et al., 2001 (th)[143]
	650-400 cm^{-1}	1100-750 cm^{-1}	Wu et al., 2017 (exp/th)[39]

Table 4.1: Predicted (th) and experimentally observed (exp) vibrational frequencies of H species in CeO_{2-x}.

Even though the mechanism for H incorporation into bulk CeO_{2-x} remains unclear, the presence of O vacancies seems to be an essential prerequisite. Theoretical calculations have shown that hydrides, formed as intermediates in the heterolytic dissociation of H_2, might be stabilized by O vacancies within CeO_{2-x}.[39, 119] O vacancies might furthermore facilitate the diffusion of H species from the CeO_{2-x} surface into the bulk.[117, 136]

4.2 Dissociation of D_2 on CeO_2(111)

In a first set of experiments, we investigated the dissociation of D_2 on stoichiometric CeO_2(111). In any catalytic reaction involving hydroxyls, choosing the right reaction temperature is key to optimize the catalyst's performance. This is especially important for CeO_2, on which high temperatures lead to the formation, but also the elimination of hydroxyl groups and eventually to the formation of O vacancies. With our experiments, we aim to gain insights into the temperature dependence of (i) the

D_2 dissociation reaction and (ii) the O vacancy formation by recombinative desorption of hydroxyls as water. In order to do so, we exposed CeO_2(111) to 10 mbar of D_2 in a high pressure cell at different temperatures. We follow the dissociation reaction in situ by monitoring OD vibrations with IRAS. As shown in Chapter 3, the use of D_2 allows us to track the possible formation of O vacancies: IR signals in the OH stretching region indicate that H_2O from the background gas dissociates over O vacancies. In addition, we characterized the hydroxylated surfaces by XPS.

Fig. 4.2 shows IRAS spectra recorded in situ during exposure of CeO_2(111) to 10 mbar D_2 at different temperatures, and after removal of the D_2 gas phase at 200 K. For better comparison, the same spectra are replotted in Fig. 4.3, where they are grouped according to the three subsequent stages of each experiment: (a) during exposure of CeO_2(111) to 10 mbar D_2 at the specified temperature (total exposure time 15 min), (b) after cooling to 200 K in D_2, and (c) in vacuum at 300 K after pumping out the D_2 gas phase.

Comparing the spectra of the individual treatments in Fig. 4.3 reveals a clear effect of the sample temperature. During D_2 exposure, vibrational bands of surface OD groups appear in different intensity and frequency depending on the applied temperature (see Fig. 4.3a). Between 300 K and 500 K, the intensity of the OD band increases from nearly indiscernible features to a sharp, intense band at ~2695 cm^{-1}. At 600 K, this band is shifted to 2685 cm^{-1} and appears in reduced intensity. The absence of other features shows that the oxide surface is free from impurities in all experiments.
The appearance of OD bands in these spectra clearly indicates that D_2 dissociates on the CeO_2(111) surface. Since hydroxyl groups on CeO_2(111) are oriented almost perfectly upright on the surface, we assume that the intensity of the OD band scales with the OD concentration. Hence, between 300 K and 500 K, more OD groups are formed with increasing temperature. In previous experiments with D/D_2, we attributed different vibrational frequencies to OD groups in different local environments, i.e. 2672 cm^{-1} to OD($1Ce^{3+}$,$2Ce^{4+}$) (or OD(I)), and 2683 cm^{-1} to OD($2Ce^{3+}$,$1Ce^{4+}$) (OD(II)). Following this trend, the OD band appearing at ~2695 cm^{-1} during D_2 dissociation at 400 K and 500 K might correspond to OD in an even more reduced environment. Such a highly reduced environment may form when hydrogen diffuses on the surface to form hydroxyl clusters, such as trimers.[14, 52]
The vibrational band that appears during exposure at 600 K corresponds to OD(II) species. The reduced intensity of the band as compared to exposure at 500 K indi-

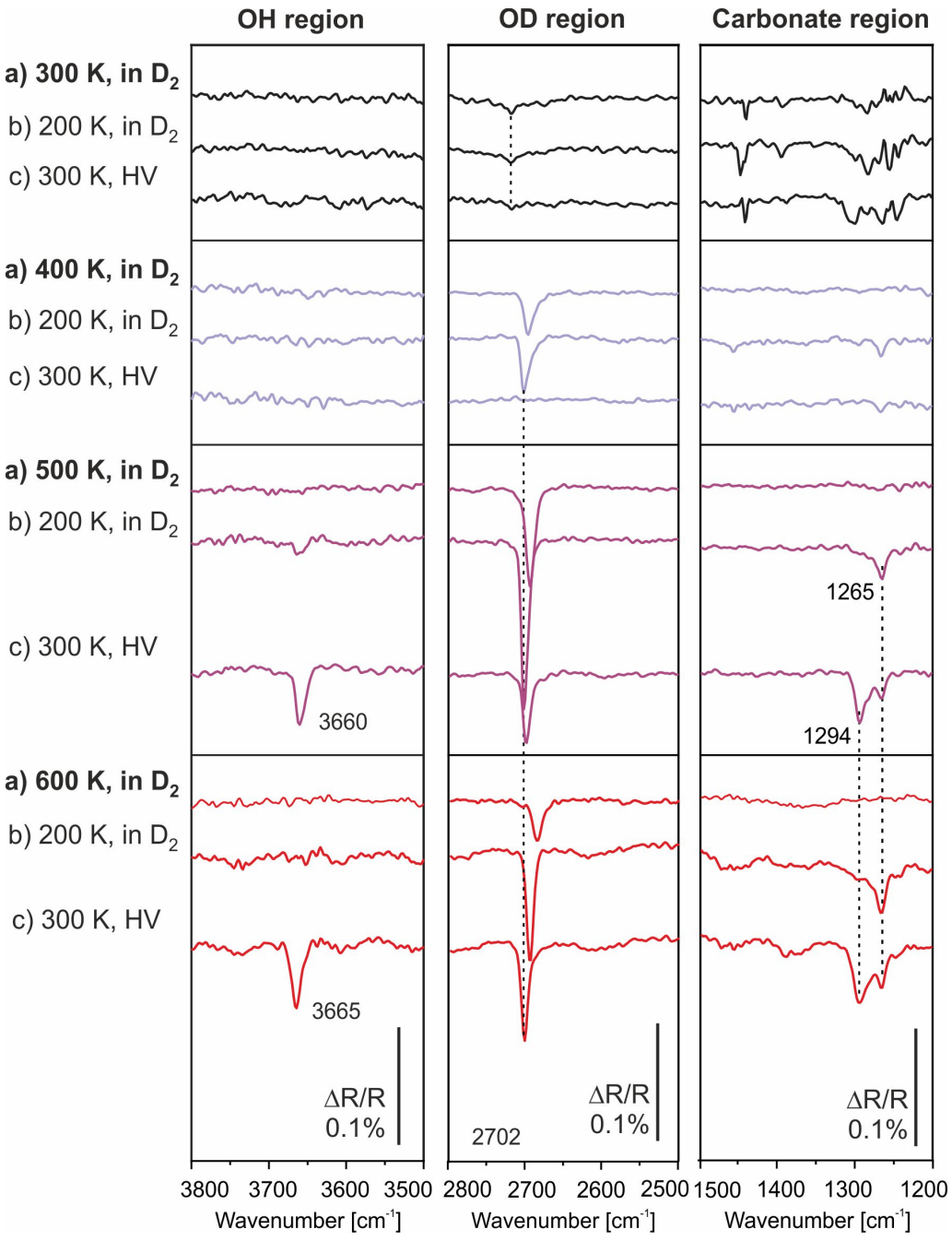

Fig. 4.2: Temperature-dependence of D_2 interaction with $CeO_2(111)$, followed by IRAS. Spectra of the same color are taken subsequently in a single experiment: a) during exposure to 10 mbar D_2 at indicated temperature (t=15 min), b) cooled to 200 K in D_2, c) in high vacuum (HV) at 300 K after pumping out D_2.

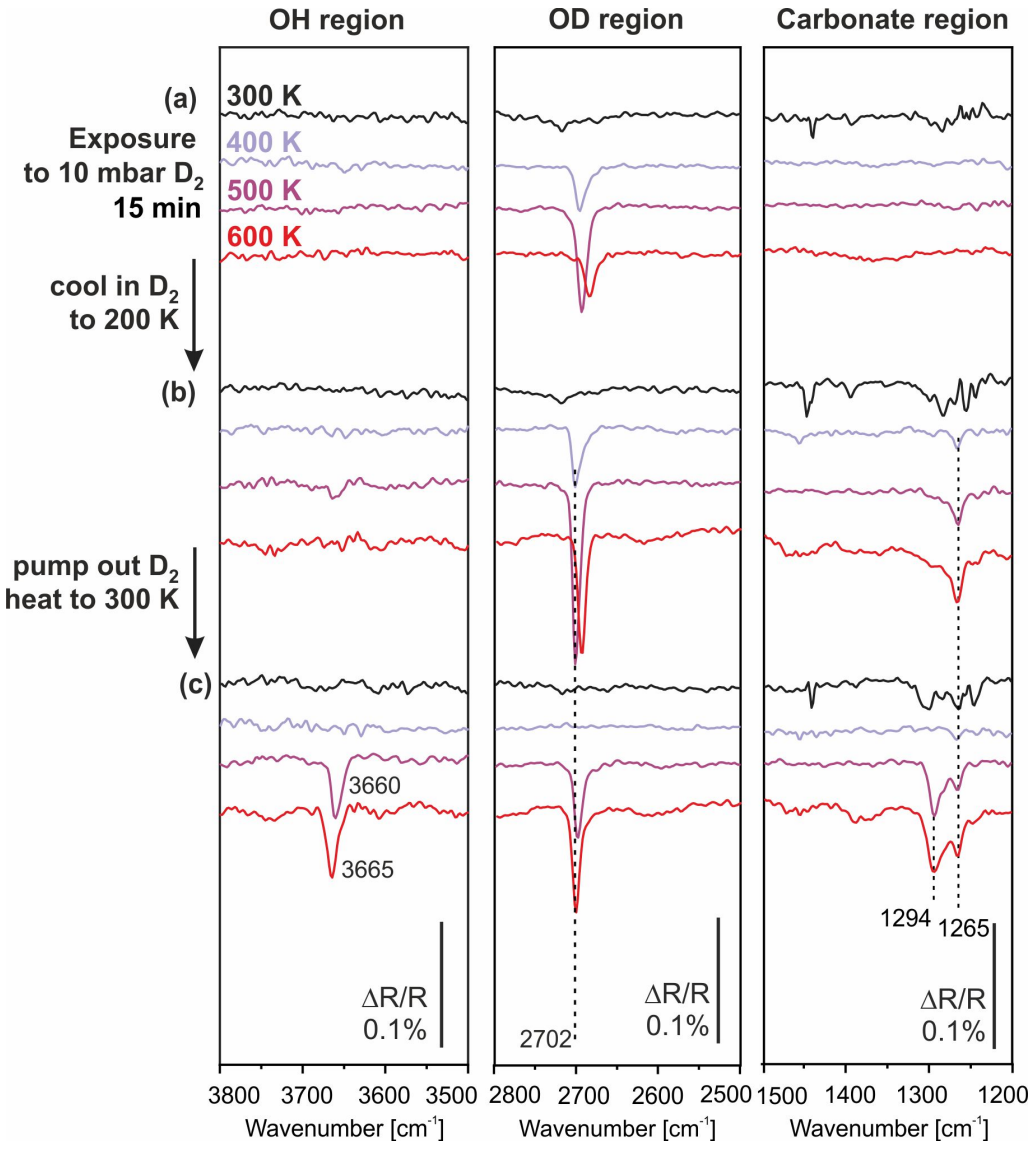

Fig. 4.3: Replot of Fig. 4.2, grouped by individual stages of the experiments: a) during exposure to 10 mbar D_2 at 300-600 K (t=15 min), b) cooled to 200 K in D_2, c) in high vacuum at 300 K after pumping out D_2. Spectra of the same color were recorded during one experimental sequence a→b→c.

cates that less OD remains on the surface at 600 K, possibly due to recombinative desorption as D_2O. This process leads to the formation of O vacancies, and thus reduces the oxide surface.

Subsequent cooling of the hydroxylated $CeO_2(111)$ surface (see Fig. 4.3b) shifts the OD bands to slightly higher frequencies in all experiments. After exposure at 400 K and 500 K, the OD band shifts to 2702 cm^{-1}. At the same time, the width of the OD band significantly decreases for exposure temperatures of 500 K and 600 K, which indicates a higher uniformity in the local environments of the respective OD groups. Given its high frequency and narrow width, we assign the band at 2702 cm^{-1} to OD($3Ce^{3+}$) (OD(III)), i.e. OD in a highly reduced environment that may form by clustering of the hydroxyl groups.[14, 52] Apart from OD features, vibrational bands appear at 1265 cm^{-1} after sample treatment at 500 K and 600 K, indicating a small concentration of chemisorbed CO_2. We investigate the chemical nature of these species in chapter 5.

In the last stage of the experiment (see Fig. 4.3c), we assess the stability of the OD groups in vacuum at 300 K. Interestingly, the OD groups formed at 400 K seem to disappear already at this relatively low temperature. On the same note, the OD band intensity decreases after treatment at 500 K and 600 K, while a new band appears in the OH region at 3660-3665 cm^{-1}. Given the results on thermal stability of hydroxyl groups on CeO_2 (see Chapter 3), we attribute this decrease in OD intensity at 300 K to the desorption of OD from slightly reduced environments (OD(I)) as D_2O. D_2O desorption creates O vacancies on the surface, which in turn may serve as dissociation sites for background H_2O traces, generating surface OH groups, as described in the following equations:

$$2\,\mathrm{OD_{ads}} \rightarrow \mathrm{D_2O\,(g)} + \square + \mathrm{O^{lattice}} \tag{4.2}$$

$$\mathrm{H_2O^{\mathit{w}}(g)} + \square + \mathrm{O^{lattice}} \rightarrow \mathrm{HO^{\mathit{w}}_{ads}} + \mathrm{HO^{lattice}_{ads}} \tag{4.3}$$

Obtained subsequently in UHV from the same samples, Fig. 4.4a shows corresponding grazing emission XP spectra. After exposure at 400 K, only very weak Ce^{3+} features appear in the Ce 3d spectrum, in agreement with the small concentration of OD observed in IRAS. Furthermore, O 1s XPS verifies that no hydroxyl groups remain on the surface after removal of the D_2 phase. In contrast to this, clear hydroxyl features arise in the O 1s spectra alongside intense Ce^{3+} features in the Ce 3d region after D_2 treatments at 500 K and 600 K. As observed on clean $CeO_{2-x}(111)$ (see section 2.6.2), the O 1s main peak in these spectra is shifted to higher BE with

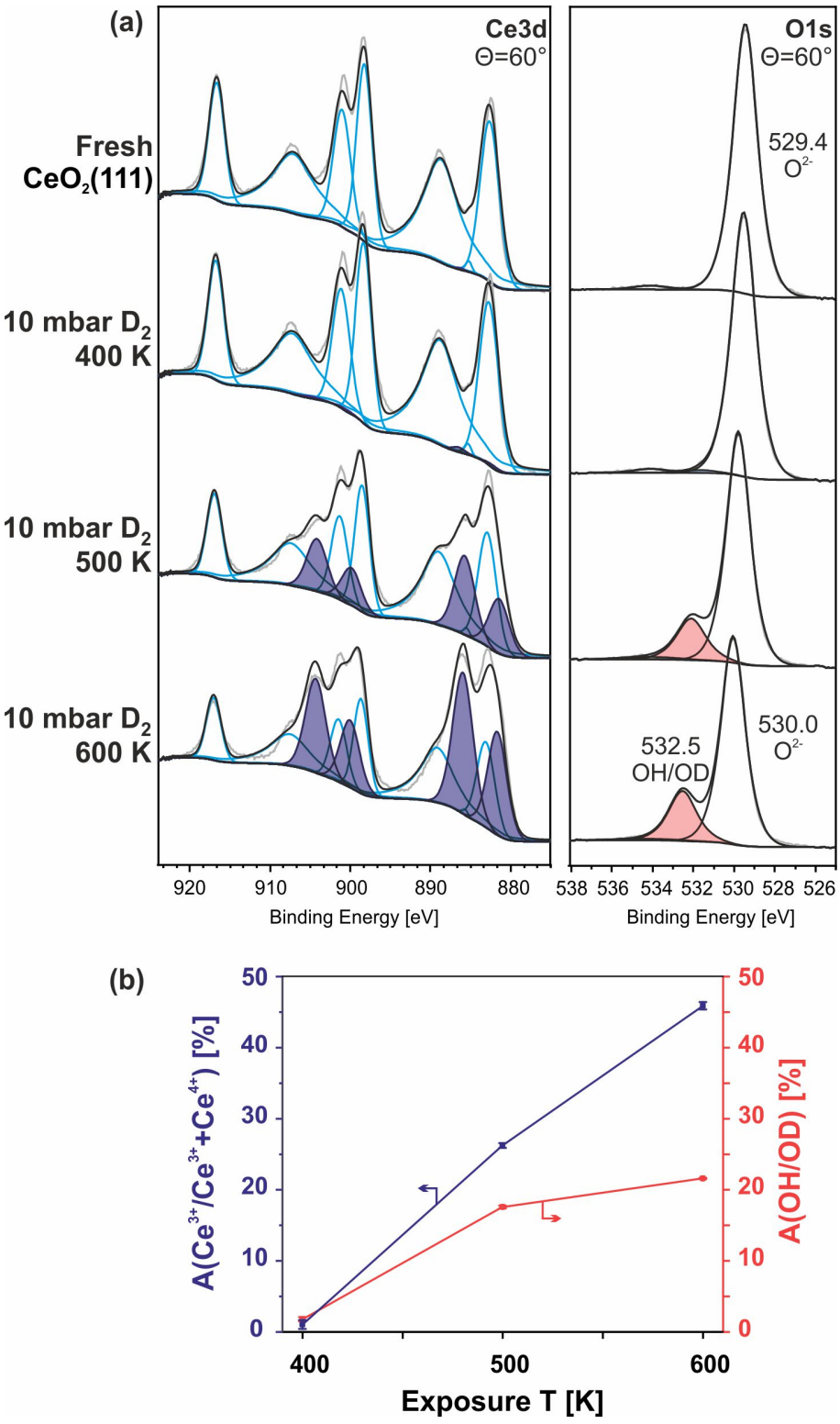

Fig. 4.4: a) Grazing emission Ce 3d and O 1s XP spectra recorded at 300 K after exposure of $CeO_2(111)$ to 10 mbar D_2 at specified temperatures. Spectra were recorded at 300 K and are equivalent to the sample state in Fig. 4.3c. b) Relative concentrations of Ce^{3+} and OH as a function of exposure temperature.

increasing reduction state of the surface.
Comparing the Ce^{3+} and hydroxyl concentration on $CeO_2(111)$ after D_2 exposure (see Fig. 4.4b) reveals a clear effect of the exposure temperature: The higher the temperature, the more hydroxyl groups and Ce^{3+} species are generated. However, after exposure at 600 K, the concentration of Ce^{3+} increases considerably, while the amount of surface hydroxyls stays almost unchanged in comparison with the experiment at 500 K. This discrepancy is a clear indication for the formation of O vacancies by elimination of water from the hydroxylated surface at 600 K.

To gain further insights into the H_2 dissociation reaction on CeO_2, Dr. Thomas Kropp, Dr. Joachim Paier, and Prof. Joachim Sauer of the Humboldt University Berlin performed complementary DFT+U studies. Their results shall be summarized in the following. Further details, also on the computational methodology, may be found in reference [130].

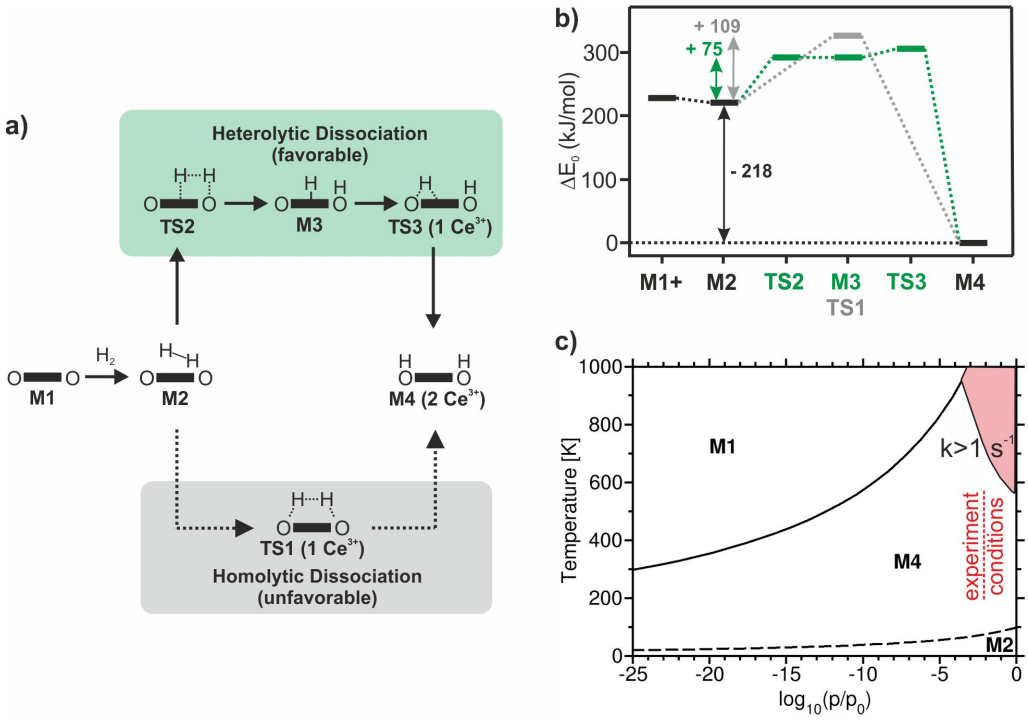

Fig. 4.5: DFT+U results (Th. Kropp, J. Paier, J. Sauer) for H_2 dissociation on CeO_2: a) intermediates and products via heterolytic and homolytic pathways, b) calculated energies of the reactions, c) phase diagram for heterolytic dissociation. The red line indicates the conditions used in the experiments described above. Adapted with permission from [130]. Copyright 2017 American Chemical Society.

In their studies, Kropp and coworkers re-investigated the energetics of a heterolytic versus a homolytic H_2 dissociation pathway on CeO_2(111), and could verify the heterolytic mechanism to be kinetically favorable due to its more stable transition states and overall lower activation barrier (see Fig. 4.5a+b). H_2 dissociation is initiated by weak molecular adsorption of H_2 onto the CeO_2(111) surface (state **M2**). The heterolytic dissociation pathway proceeds trough a transition state in which the H-H bond is coordinated to a Ce^{4+}-O^{2-} unit (**TS2**), and yields the weakly stabilized intermediate **M3**, which is an ensemble of a surface OH and Ce-H (hydride) group. From there, the H atom of the hydride group is transferred to a neighboring O ion of the lattice through **TS3**. Finally, the dissociation reaction yields **M4**, a stable ensemble of two OH groups neighboring two reduced Ce^{3+} species. The calculated large activation barrier corroborates our experimental result that D_2 dissociation is activated only at elevated temperatures.

Kropp et al. further computed the Gibbs free energy of species involved in the heterolytic dissociation to include pressure and temperature effects. The resulting phase diagram (which ignores the possibility of O vacancy formation) is shown in Fig. 4.5c. As a result of entropic effects, molecular adsorption of H_2 (**M1**→**M2**) is endergonic above 100 K, which disfavors the dissociation reaction. Fast hydroxylation of the surface ($k>1\ s^{-1}$, see section marked red in the phase diagram) may only be achieved at D_2 pressures of at least 0.1 mbar and temperatures above 600 K. The slow pace of the dissociation reaction at lower pressures explains why this reaction could not yet be observed within the UHV pressure limitations of common surface science studies.[27, 99, 109]

In summary, our studies on the dissociation of D_2 on CeO_2(111) show:

- D_2 dissociation is activated at $T \geq 400$ K ($p(D_2)$=10 mbar),
- D_2 dissociation at $T \leq 500$ K may yield OD groups in a highly reduced environment (OD($3Ce^{3+}$) or *OD(III)*, ν(OD)=2702 cm^{-1}) through formation of OD clusters,
- O vacancy formation by elimination of D_2O is pronounced at 600 K.

4.3 Formation of Hydrides in CeO_{2-x}

To assess the interaction of molecular hydrogen (D_2/H_2) and $CeO_2(111)$ beyond hydroxylation, we investigated whether D (H) species may be incorporated below the oxide surface. Previous studies on this topic came to contradicting conclusions, which is most likely owed to the fact that hydrogen below the surface is difficult to trace spectroscopically. Since most studies have reported on hydrogen incorporation in the case of reduced CeO_{2-x} samples, we focus our studies on the role of O vacancies in the possible stabilization of D (H) species within $CeO_{2-x}(111)$ thin films.

4.3.1 Hydride Formation at Room Temperature

To asses whether D incorporation below the $CeO_2(111)$ surface takes place when O vacancies are introduced, we performed a series of experiments in which we exposed thermally reduced, O vacancy-rich $CeO_{2-x}(111)$ to 10 mbar of D_2 at 300 K. The temperature of 300 K was chosen such that surface hydroxylation and additional formation of O vacancies by water elimination could be excluded (see section 4.2).

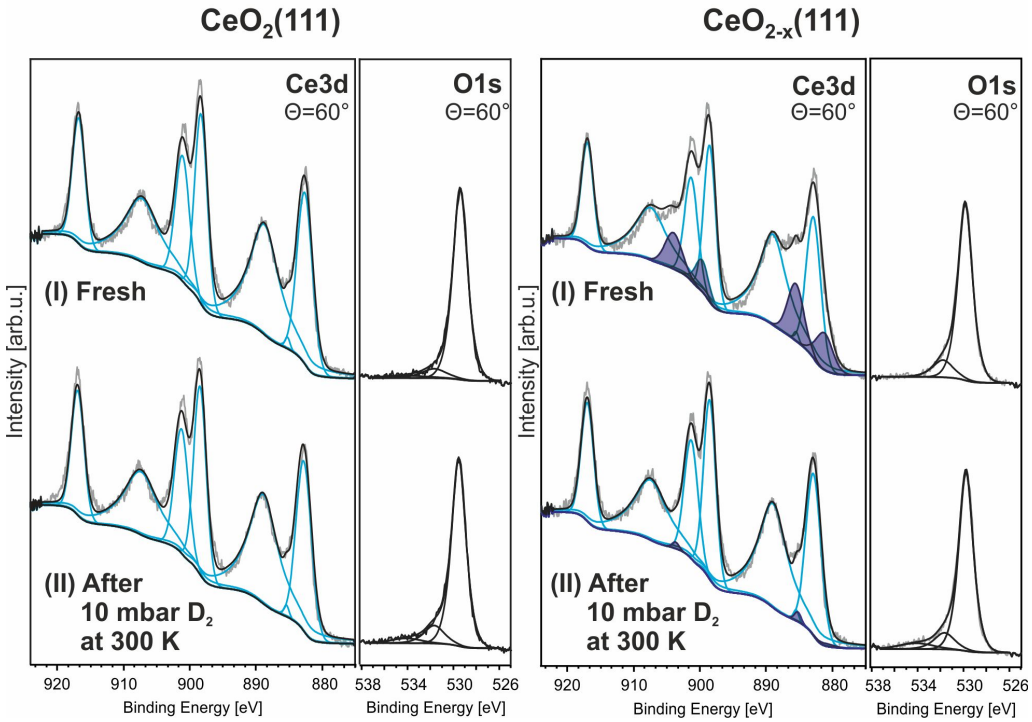

Fig. 4.6: Grazing emission Ce 3d and O 1s XP spectra of $CeO_2(111)$ (left) and $CeO_{2-x}(111)$ (right) before and after exposure to 10 mbar D_2 for 15 min at 300 K.

Fig. 4.6 shows XP spectra of stoichiometric $CeO_2(111)$ and reduced $CeO_{2-x}(111)$ thin films recorded before (I) and after (II) exposure to 10 mbar D_2 (t=15 min) at 300 K. While the XP spectrum for $CeO_2(111)$ is effectively unchanged after D_2 treatment, considerable changes occur on reduced $CeO_{2-x}(111)$.
Before D_2 exposure, $CeO_{2-x}(111)$ shows characteristic XPS features, most prominently intense Ce^{3+} components in the Ce 3d region. In the O 1s region, the main peak (lattice O^{2-}) shows the typical shift to higher BE and a high BE shoulder, which may be attributed to surface hydroxyls. The presence of these hydroxyls is not surprising given the affinity of background water to dissociate over O vacancies (see section 3.1) and may be further promoted by the presence of defects.
After exposure to D_2, the Ce^{3+} features of $CeO_{2-x}(111)$ diminish to a large extent, leaving the film almost completely oxidized. At the same time, no considerable changes in peak intensity or position occur in the O 1s region. The total intensity of the O 1s features is unchanged after exposure within the error margin of the XPS experiment, which excludes that the observed oxidation occurs by diffusion of lattice O to the surface or through incorporation of water.
In agreement with the barely changed O 1s XP spectrum, IRAS measurements during D_2 exposure at 300 K (see Fig. 4.7) show OD features in only very weak intensity on both the $CeO_2(111)$ and the $CeO_{2-x}(111)$ surface. These weak features vanish when the D_2 gas phase is removed at 200 K (not shown).

Kropp and coworkers[130] predict the vibrational frequency of bulk OD within CeO_2 to be 2511 cm^{-1}. The absence of such a feature in our IRAS spectra does not necessarily indicate that no bulk hydroxyls are present, but might result from a largely surface-parallel orientation of subsurface OD groups. Unfortunately, the frequency range below 1200 cm^{-1} is not accessible with our IRAS setup, so that we cannot assess previously predicted Ce-H frequencies (1100-750 cm^{-1} and 650-400 cm^{-1}).[39, 143]

The changes in oxidation state of $CeO_{2-x}(111)$ upon exposure to D_2 may be linked to a possible incorporation of D species below the oxide surface. To assess this hypothesis, we undertook Nuclear Resonance Analysis (NRA) measurements on $CeO_2(111)$ and $CeO_{2-x}(111)$ thin films after exposure to H_2 under similar conditions ($p(H_2)$=10 mbar, t=15 min, T=300 K). Please note that resonant H-NRA is only sensitive to the ^1H nucleus, not to its ^2D isotope. To investigate the stability of detected H species, and to exclude beam damage to the oxide lattice, we performed two subsequent NRA measurements on each sample.

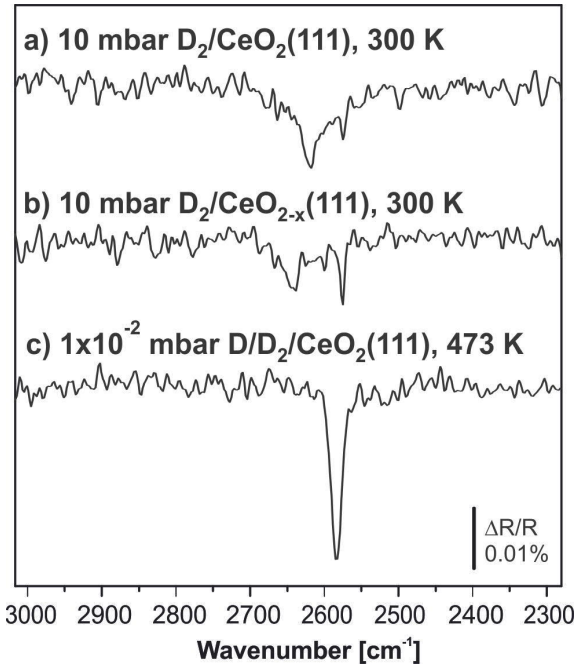

Fig. 4.7: IRAS spectra recorded during exposure of (a) $CeO_2(111)$ and (b) $CeO_{2-x}(111)$ to 10 mbar D_2 at 300 K. (c) $CeO_2(111)$ during exposure to 1×10^{-2} mbar D/D_2 at 473 K for comparison.

Fig. 4.8 shows H depth profiles of stoichiometric $CeO_2(111)$ and reduced $CeO_{2-x}(111)$ after exposure to H_2. On $CeO_2(111)$, the profile shows a feature at $\sim E_{res}$, which translates to an occurrence of H species on the $CeO_2(111)$ surface, or possibly in the first few atomic layers below. The peak area of this feature amounts to an estimated H coverage of 0.5 ± 0.1 ML (where 1 ML is the H concentration on a fully hydroxylated $CeO_2(111)$ surface). We tentatively assign this feature to OH groups formed by dissociation of H_2 on defective surface sites. The XPS and IRAS experiments above did not show any features of hydroxyls. However, it should be noted that these have been recorded on a different $CeO_2(111)$ thin film and in a different UHV chamber. Even though the same growth procedure was followed to prepare the $CeO_2(111)$ film, differences in surface roughness may have occurred due to different instrumentation. A subsequently recorded H depth profile shows the same characteristics and thereby suggests that the NRA ion beam does affect neither the integrity of the oxide film nor the concentration of the hydroxyl groups.

The H depth profile obtained after exposing the reduced $CeO_{2-x}(111)$ film to H_2 shows a feature of similar intensity at E_{res} (hence, at the surface or just below). This feature, however, is not symmetrical as in the case of $CeO_2(111)$, but shows clear tailing to higher ion energies, which we assign to H species incorporated be-

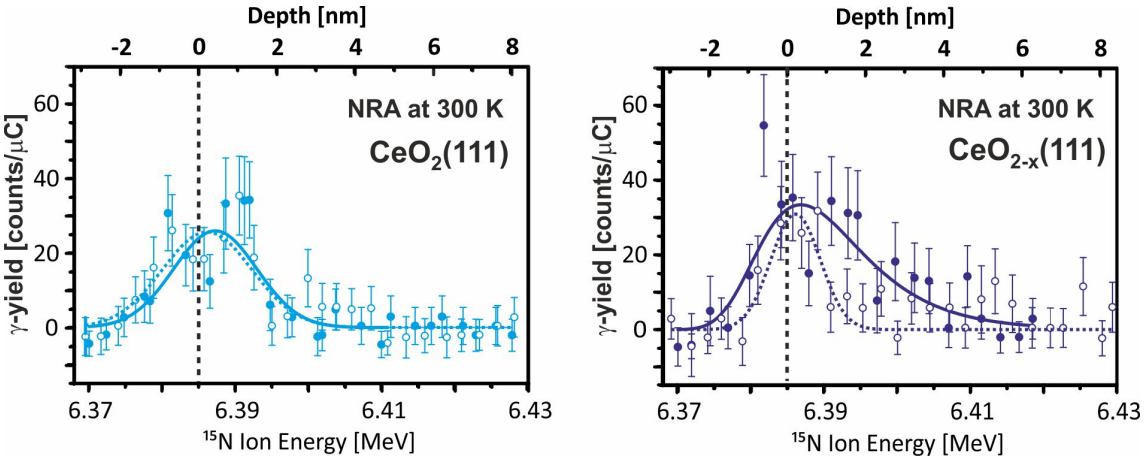

Fig. 4.8: NRA H depth profiles recorded on $CeO_2(111)$ (left) and $CeO_{2-x}(111)$ (right) after exposure to 10 mbar H_2. On each surface, two profiles have been recorded subsequently to explore beam effects. The first profile is shown in a bold, the second in a dashed line. Adapted with permission from [130]. Copyright 2017 American Chemical Society.

low the oxide surface, in a depth of up to ∼2 nm. The total extent of detected H amounts to 0.8 ML ± 0.1 ML. A subsequently recorded H depth profile still shows a feature at E_{res}, but lacks the tailing to higher energy, which suggests that the incorporated H species desorb during interaction with the high energy NRA ion beam.

The NRA studies show that H species may be incorporated at room temperature below the surface of $CeO_{2-x}(111)$, given that O vacancies are present in the material. As XPS shows, the incorporation of these species results in a change in the electronic structure of the oxide, re-oxidizing Ce^{3+} species to Ce^{4+}. This change in oxidation state, which is not related to a change of O distribution in the film, might be explained by the formation of a hydride species.

In collaboration with our group, Dr. Xiaoke Li, Dr. Joachim Paier, and Prof. Joachim Sauer at the Humboldt University Berlin investigated the stability of hydrides within $CeO_{2-x}(111)$ by DFT+U calculations. The results of their studies shall be summarized in the following. Details on the computational methodology may be found in reference [144].
In a first study, Li and colleagues investigated the energetics of hydride formation on a fully reduced $CeO_{1.5}(111)$ surface. Indeed, CeH_x layers form on $CeO_{1.5}(111)$ when H_2 is offered to the system. At the same time, Ce^{3+} ions in the layers below are largely re-oxidized to Ce^{4+}. The resulting CeH_x ad-layer models are shown in

Fig. 4.9, while their formation energies and predicted vibrations are summarized in Table 4.2.

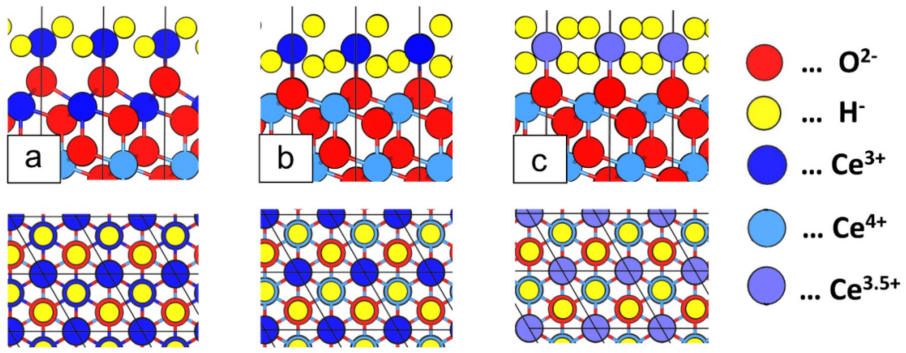

Fig. 4.9: DFT+U-calculated structures of surface hydride layers on $CeO_{2-x}(111)$: a) CeH_2, b) CeH_3, c) CeH_4. The 1st row shows a side view of the systems, the 2nd row a top view.[144]

Structure	Formation Energy [eV]		Vib. Frequency [cm^{-1}]	
	PBE+U	HSE	ν(Ce-H)	ν(Ce-D)
CeH_2	-1.85	-2.06	1278	902
CeH_3	-1.08	-1.41	1107	780
CeH_4	-0.37	-0.57	967	680

Table 4.2: Computationally predicted formation energies of various surface CeH_x layers and corresponding computed ν(Ce-H) or ν(Ce-D) frequencies (PBE+U, unscaled). The formation energies of CeH_x layers are calculated based on the following equation (n=2,3,4):[144] $4\,CeO_{1.5}(111) + {}^{x}/_{2}\,H_2 \longrightarrow CeH_x \cdot 3\,CeO_2(111)$.

The formation of all investigated ad-layers is exothermic. An increase in the amount of hydrides in the ad-layer, however, is linked to a decrease of the ad-layer stability. Vibrational frequencies of hydrides in the ad-layer, ν(Ce-H) and ν(Ce-D), are predicted to be 1278-967 cm^{-1} and 902-680 cm^{-1}, respectively. In the IRAS experiments with D_2 (described above), we observed no signal of a ν(Ce-D) surface vibration, possibly due to its low expected frequency. However, our $CeO_{2-x}(111)$ thin film also exhibits a lower degree of reduction than what was assumed in the ad-layer calculations, so that it is not clear whether hydrides may be stabilized on its surface.

To account for this, Li and coworkers furthermore investigated the formation energy of hydrides within several partially reduced $CeO_{2-x}(111)$ models. These models

incorporate either isolated O vacancies, O vacancy pairs, or clusters of four O vacancies. These three different types of defects, in turn, were incorporated either within the topmost layers or into the 'bulk' (10^{th} atomic layer) of a $CeO_2(111)$ model. A schematic illustration of the different types of investigated structures may be found in Fig. 4.10a. As an example, Fig. 4.10b shows $CeO_{2-x}(111)$ systems with an isolated O vacancy in the surface layer or in the bulk, and the structures resulting when a hydride is incorporated into these systems.

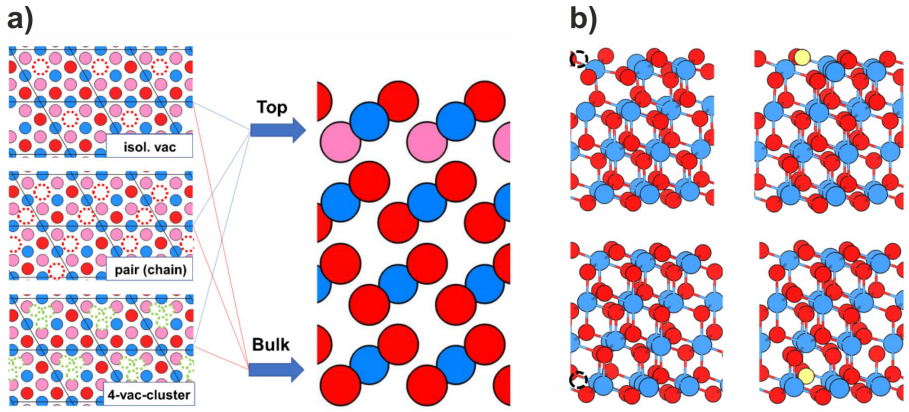

Fig. 4.10: a) Schematic illustration of $CeO_{2-x}(111)$ structures used to calculate hydride formation energies. Isolated O vacancies, O vacancy pairs and clusters of four O vacancies are placed on the surface or into the 'bulk' (10^{th} atomic layer) of the oxide. b) Structure of $CeO_{2-x}(111)$ with isolated O vacancy on surface and in bulk (left) and computed structure when isolated hydride is incorporated (right). O=red/pink, Ce^{3+}/Ce^{4+}=blue, H=yellow. Dashed circles indicate O vacancies.[144]

Structure	H^- Formation Energy [eV]	
	Surface	Bulk
Isolated O vac	+0.44	+0.01
O vac pair (chain)	+0.69	-0.39
Cluster (4 O vac)	+0.62	-0.83

Table 4.3: PBE+U-predicted hydride formation energies on $CeO_{2-x}(111)$ with various O vacancy structures on the surface or in the bulk.[144]

Table 4.3 summarizes the hydride formation energies computed on these various $CeO_{2-x}(111)$ structures. Judging from these values, hydrides are thermodynamically

unstable when O vacancies exist only on the $CeO_{2-x}(111)$ surface. Hydrides are stabilized, however, at O vacancies in the CeO_{2-x} bulk. The higher the density of O vacancies, the more thermodynamically favorable the formation of a hydride species becomes.

Though bulk hydrides are thermodynamically stable when clusters of O vacancies are present in the bulk, *hydroxyls* on the surface are predicted to be the thermodynamically most favorable species. For instance, on a $CeO_{2-x}(111)$ system with a cluster of four O vacancies in the bulk, the formation energy for a single H^- is calculated to be -0.83 eV, while the formation energy of a single OH species on the surface is -1.47 eV. The corresponding structures are shown in Fig. 4.11. Since the transformation of bulk H^- to surface OH requires the system to overcome an activation barrier, hydrides are expected to be kinetically stabilized within the bulk at low temperatures, but to transform to surface OH when the system is sufficiently heated.

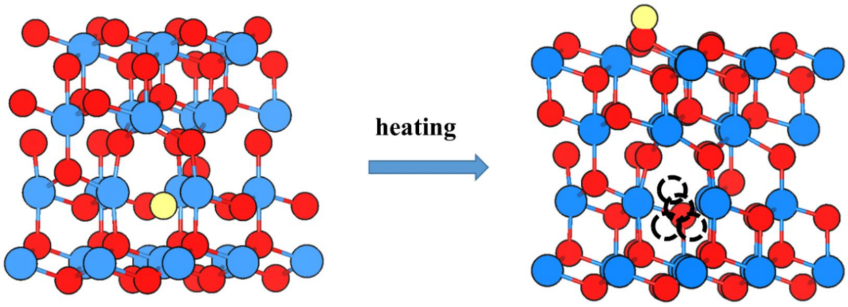

Fig. 4.11: OH formation from bulk hydrides at elevated temperature. DFT+U-computed structure of $CeO_{2-x}(111)$ (with bulk O vacancy cluster) with hydride in the bulk or hydroxyl on the surface. Dashed circles indicate O vacancies. O=red, Ce^{3+}/Ce^{4+}=blue, H=yellow.[144]

In summary, the computational studies by Li and colleagues clearly show that the formation of hydrides on $CeO_{2-x}(111)$ is thermodynamically feasible, and that hydrides form preferentially near O vacancies in the oxide bulk. Especially the presence of agglomerated O vacancies benefits hydride formation. Along with hydride formation, Ce^{3+} ions are re-oxidized to Ce^{4+}. These results fully support our experimental observation that $CeO_{2-x}(111)$ is re-oxidized when H species are incorporated below its surface.

4.3.2 Thermal Stability of Bulk D (H) Species

To gain further insights into the behavior of the incorporated species, we assessed their thermal stability by means of TP-XPS and TPD.

For the TP-XPS measurements, we exposed a reduced CeO_{2-x}(111) thin film to 10 mbar of D_2 at 300 K and subsequently characterized the system with XPS in grazing emission in between heating steps. Fig. 4.12 shows the concentration of Ce^{3+} as a function of the annealing temperature. Similar to the experiment discussed above, the relative concentration of Ce^{3+} decreases from 17±0.5% on freshly prepared CeO_{2-x}(111) to 3±0.1% after D_2 exposure. During subsequent heating in UHV, the original reduction state of the oxide film is recovered in two steps. Between 300 K and 450 K, the concentration of Ce^{3+} increases to ∼9%, and thereafter stays largely unchanged up to ∼800 K. Between 800 K and 900 K, the original reduction state before D_2 exposure is recovered.
TPD curves (see Fig. 4.13) recorded up to 800 K from an equivalently treated CeO_{2-x}(111) film show desorption of D_2 between 250 K and 400 K, hence in the same temperature region during which the low temperature increase in Ce^{3+} concentration takes place. No desorption of D_2O is observed over the whole temperature range. The observed desorption of D_2 corroborates the TP-XPS results and supports the hypothesis that re-oxidation of CeO_{2-x} is linked to the reversible formation of hydride species within the oxide bulk.
To quantify the amount of D_2 desorbing between 250 K and 400 K, we compare the D_2 TPD trace to the H_2 TPD trace obtained from a clean Ru(0001) sample after exposure to 10 mbar H_2 (see Fig. 4.13). The H_2/Ru(0001) desorption curve shows characteristic features of a saturated H monolayer on Ru(0001).[145, 146] This indicates that no H species are incorporated into the Ru bulk under the exposure conditions. By comparison of the peak areas of both curves, assuming that (i) H_2 and D_2 generate the same detector response, and that (ii) a full monolayer of H species desorbs from the Ru(0001) sample, we estimate the amount of D_2 desorbing from CeO_{2-x}(111) as equivalent to ∼0.3 ML H/Ru(0001).
CO adsorption experiments (not shown) verify that the CeO_{2-x}(111) film almost completely covered the Ru substrate. In consequence, we exclude that the large amounts of desorbing D_2 originate from D directly adsorbed onto Ru(0001). Interestingly, D_2 desorbs from CeO_{2-x}(111)/Ru(0001) within the same temperature range as it would from Ru(0001). This may indicate that small areas of uncovered Ru(0001) serve as a gateway for desorption of D species.

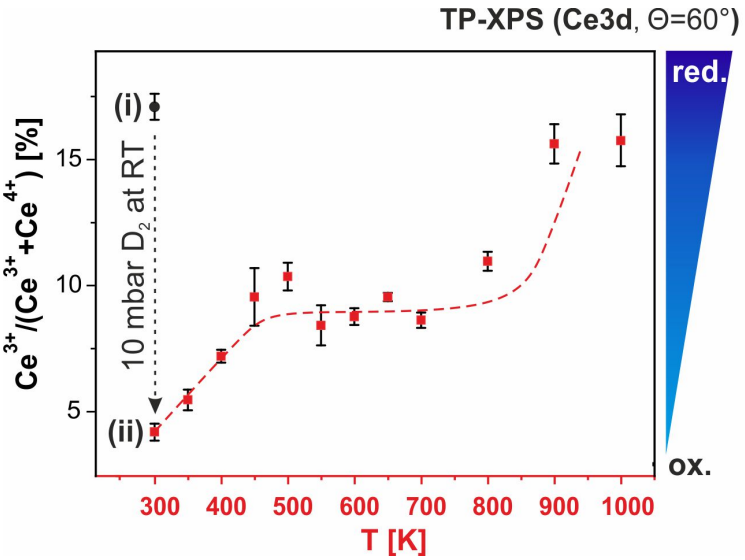

Fig. 4.12: Change in relative Ce^{3+} concentration on $CeO_{2-x}(111)$ after exposure to 10 mbar D_2, and during subsequent annealing in UHV to indicated temperatures, determined from Ce 3d XPS measurements in grazing emission. The dashed line serves as a guide to the eye.

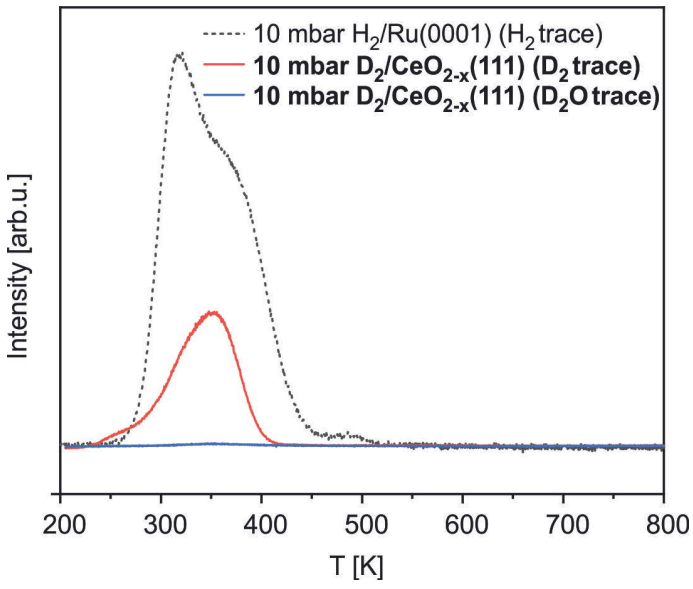

Fig. 4.13: TPD curves recorded after exposure of $CeO_{2-x}(111)$ to 10 mbar D_2 at 300 K, and H_2 TPD curve for a Ru(0001) surface exposed to 10 mbar of H_2 as comparison.

Equivalent TPD experiments on other $CeO_{2-x}(111)$ thin films did trace neither D_2 nor D_2O desorption, even though a re-oxidation of the oxide after heating was clearly apparent. In these cases, it is unclear how the hydride vanishes from the bulk. It is possible, however, that it diffuses towards deeper layers and eventually stabilizes at the CeO_2/Ru interface.

In summary, our studies on the interaction of D_2 (H_2) and $CeO_{2-x}(111)$ show:

- At 300 K, D is incorporated below the $CeO_{2-x}(111)$ surface as a hydride.
- The formation of this hydride species is strongly linked to the presence of O vacancies, and causes re-oxidation of Ce^{3+} species to Ce^{4+},
- The incorporation of hydride species, and the related electronic changes within the oxide, are thermally reversible. Upon heating to 400 K, a large fraction of the hydride species desorbs from the oxide as D_2.

4.4 Hydroxyl versus Hydride Formation on $CeO_{2-x}(111)$

From the results above, it is apparent that (i) D_2 dissociates on $CeO_2(111)$ to form hydroxyls at T$\geq$400 K, and that (ii) D species are incorporated as hydrides below the surface of reduced $CeO_{2-x}(111)$ at 300 K, which causes a re-oxidation of Ce^{3+}. The hydride formation is thermally reversible, and a partial recovery of the initial degree of reduction takes place when the thin film is heated to $\sim$450 K. To assess the interplay of hydroxyl and hydride formation, we investigated how D_2 interacts with reduced $CeO_{2-x}(111)$ at different temperatures.

Fig. 4.14 shows IRAS spectra recorded in situ during exposure of $CeO_{2-x}(111)$ to D_2 at different temperatures. In the first step of each experiment, freshly prepared $CeO_{2-x}(111)$ was exposed to 10 mbar D_2 at a specified temperature between 300 K and 600 K for 15 min (a). Subsequent spectra were recorded after the sample was cooled to 200 K in D_2 (b). Finally, the D_2 gas phase was removed and the film characterized in vacuum at 300 K (c). For clarity, these spectra are replotted in Fig. 4.15 according to the subsequent stages a$\rightarrow$b$\rightarrow$c for each individual experiment. For unknown reasons, the baseline of the experiment at 300 K was unstable below 1500 cm^{-1}, so that this region is omitted for better reading in Fig. 4.15.

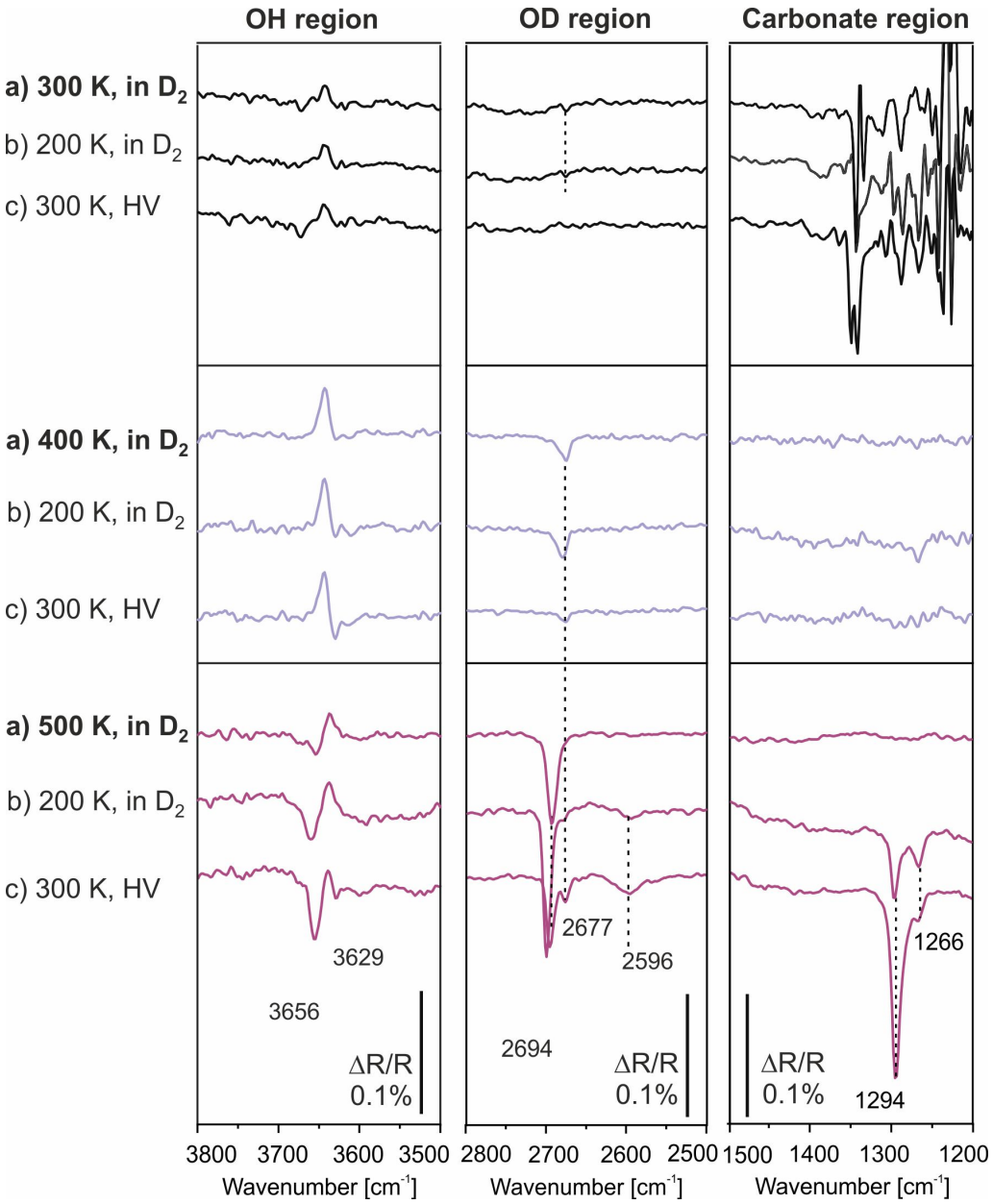

Fig. 4.14: Temperature-dependent interaction of 10 mbar D_2 with reduced $CeO_{2-x}(111)$, monitored by IRAS. Spectra of the same color are taken subsequently in a single experiment: a) during exposure to 10 mbar D_2 at indicated temperature (t=15 min), b) cooled to 200 K in D_2, c) in high vacuum (HV) at 300 K after pumping D_2.

As on $CeO_2(111)$, the hydroxylation of reduced $CeO_{2-x}(111)$ by dissociation of D_2 is a temperature-dependent process: As shown in Fig. 4.15a, vibrational OD bands increase in intensity with increasing exposure temperature. At 300 K, merely any OD features are observed. At 400 K, a weak band appears at 2677 cm^{-1}, which is tailing to larger vibrational frequencies. Finally, during exposure at 500 K, a strong OD feature arises at 2694 cm^{-1}, at a similar frequency as observed on $CeO_2(111)$.
An evident difference to the experiments on $CeO_2(111)$ is the negative vibrational band that appears in the OH region, which indicates that OH was present on $CeO_{2-x}(111)$ while the reference spectrum was recorded. This OH species vanishes during D_2 exposure. The presence of OH species before exposure may be easily explained by the large affinity of background H_2O to dissociate over O vacancies. The initially present OH groups appear at a vibrational frequency of ~3642 cm^{-1}, and therewith correspond to OH(II) (see section 3.3). During exposure to D_2, this species vanishes, which may indicate competing interaction of D_2 and background H_2O with O vacancy sites. During exposure at 500 K, an additional vibrational band appears in the OH region at 3656 cm^{-1}, hence at a similar frequency as an OH(III) species (see section 4.2).
No clear signs of adsorbed impurities (e.g. chemisorbed CO_2) are apparent during D_2 exposure at any temperature. It should be noted, however, that the IR baseline between 1500 and 1200 cm^{-1} was unstable during the experiment at 300 K, which makes analysis of this spectral region difficult.

When the $CeO_{2-x}(111)$ thin film was subsequently cooled to 200 K in D_2 (see Fig. 4.15b), OD and OH features widely remain unchanged after exposure at 300 K and 400 K. After exposure at 500 K and subsequent cooling, however, the OD band narrows and shifts to a slightly higher wavenumber, indicating a clustering of hydroxyl groups, as has previously been observed on $CeO_2(111)$ (see section 4.2). At the same time, a new band arises around 2600 cm^{-1}. While no further adsorbate bands appear after the 300 K and 400 K exposure experiments, weak bands below 1500 cm^{-1} indicate the presence of chemisorbed CO_2 after D_2 treatment at 500 K.

Finally, we removed the D_2 gas phase and heated the sample to 300 K (Fig. 4.15(c)). During this step, the intensity of the OD band decreases for all initial exposure temperatures. No hydroxyl groups remain after the treatment at 300 K, and only very weak OD and OH features are apparent after exposure at 400 K. Similar as on $CeO_2(111)$, the OD groups formed in D_2 at 400 K vanish almost completely during removal of the D_2 gas phase. OD groups formed at 500 K persist to a larger extent,

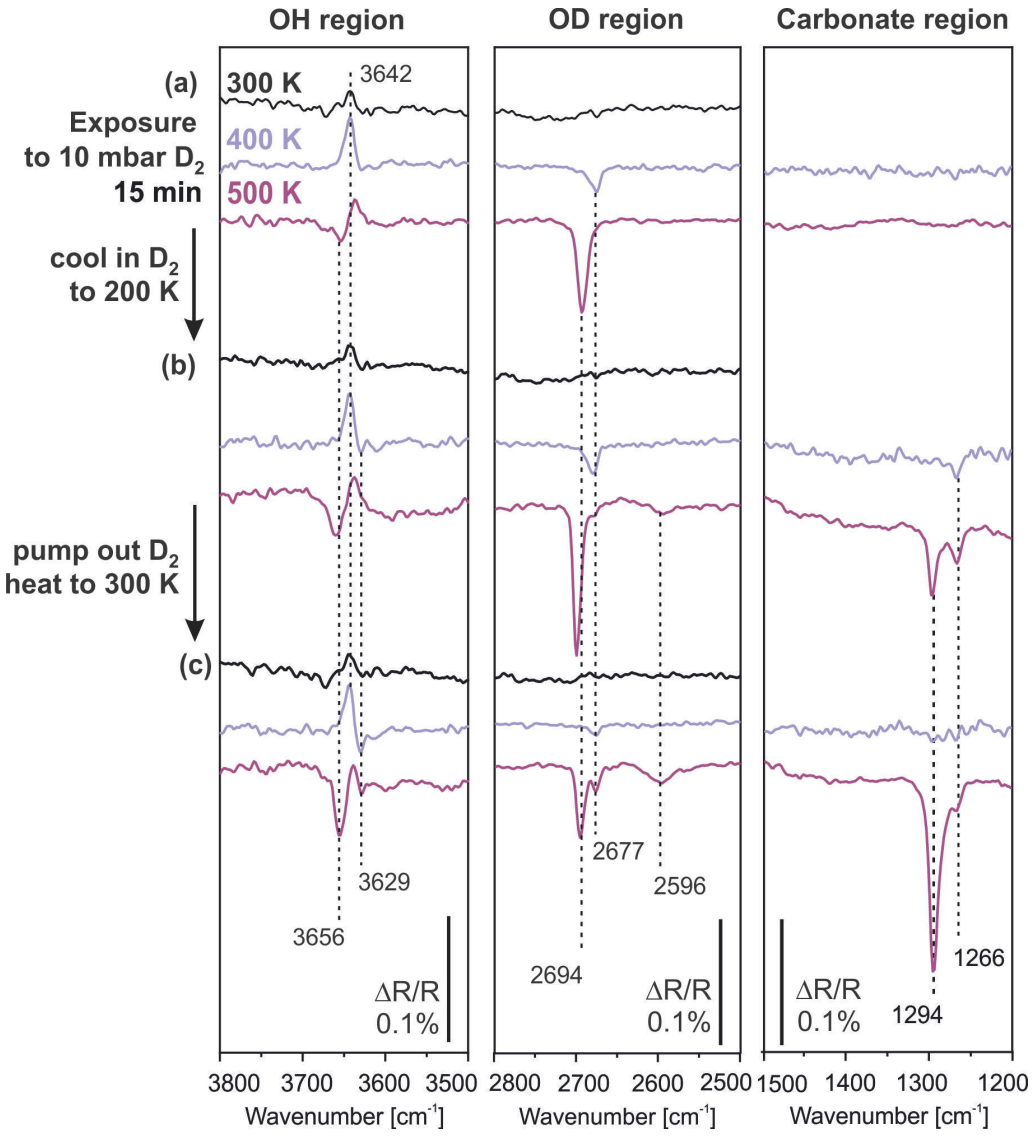

Fig. 4.15: Replot of Fig. 4.14, grouped by individual stages of the experiments: a) during exposure (t=15 min) to 10 mbar D_2 at 300-600 K, b) cooled to 200 K in D_2, c) in high vacuum at 300 K after pumping out D_2. Spectra of the same color were recorded during one experimental sequence a→b→c.

but lose intensity in benefit of the OH vibrational feature at 3656 cm^{-1} (OH(II)) and an additionally arising OH band at 2629 cm^{-1} (OH(I)). Furthermore, after exposure at 500 K, an additional feature arises in the OD region at ~2677 cm^{-1}, which we assign to OD(I) in consideration of the shifts summarized in section 3.3. Together with this feature, the yet unidentified vibrational band at 2596 cm^{-1} gains in intensity. Molecularly adsorbed water species are not stable on $CeO_2(111)$ at this temperature (see section 3) and can therefore be discarded as the origin of this feature. Its low frequency, however, is commonly associated with hydrogen-bonded hydroxyl groups, so that we tentatively assign it to hydroxyl groups formed in vacancies close below the CeO_{2-x} surface. As observed during the equivalent experiments on $CeO_2(111)$, vibrational bands appear in the region below 1500 cm^{-1} at this stage of the experiment. These bands may be traced back to chemisorbed CO_2 species, which we investigate further in chapter 5.

In addition to the IRAS measurements, we performed XPS analysis of the same $CeO_{2-x}(111)$ samples before and after exposure to D_2 (Fig. 4.16). The freshly prepared $CeO_{2-x}(111)$ thin films before exposure show characteristic XP features in the Ce 3d region, indicating a considerable concentration of Ce^{3+} species. The O 1s region is dominated by a single O^{2-} peak, while no further O-containing adsorbates, such as hydroxyls or carbonates, are detectable.

Exposure to D_2 at 400 K (see Fig. 4.16a) results in the almost complete conversion of Ce^{3+} to Ce^{4+} species, as has been observed before for exposure at 300 K (see section 4.3). Furthermore, in agreement to the IRAS measurements, only a very small amount of hydroxyls is detectable as a high BE shoulder to the O 1s main peak. The ensemble of IRAS and XPS measurements indicate, similar to the experiment at 300 K, the predominant formation of hydride species below the oxide surface. Also here, annealing to 1000 K in vacuum increases the concentration of Ce^{3+}, indicating a partial reversibility of the hydride incorporation.*
D_2 exposure at 500 K results in considerably different electronic changes (Fig. 4.16b). Here, the amount of Ce^{3+} features increases during exposure to D_2, while at the same time a clear hydroxyl peak appears at 531.9 eV in the O 1s region. Both observations indicate hydroxylation of the oxide surface. While hydride formation in the

*D_2 TPD curves obtained from this sample, as for higher exposure temperatures, exceed the expected amount of D_2 desorbing from the oxide film by 1-2 orders of magnitude. The origin of this immense D_2 feature is unknown, yet likely indicates D_2 desorption from the metal sample holder. It is not possible to differentiate between signals originating from sample or sample holder, so that these TPD curves are not included in the further experimental analysis.

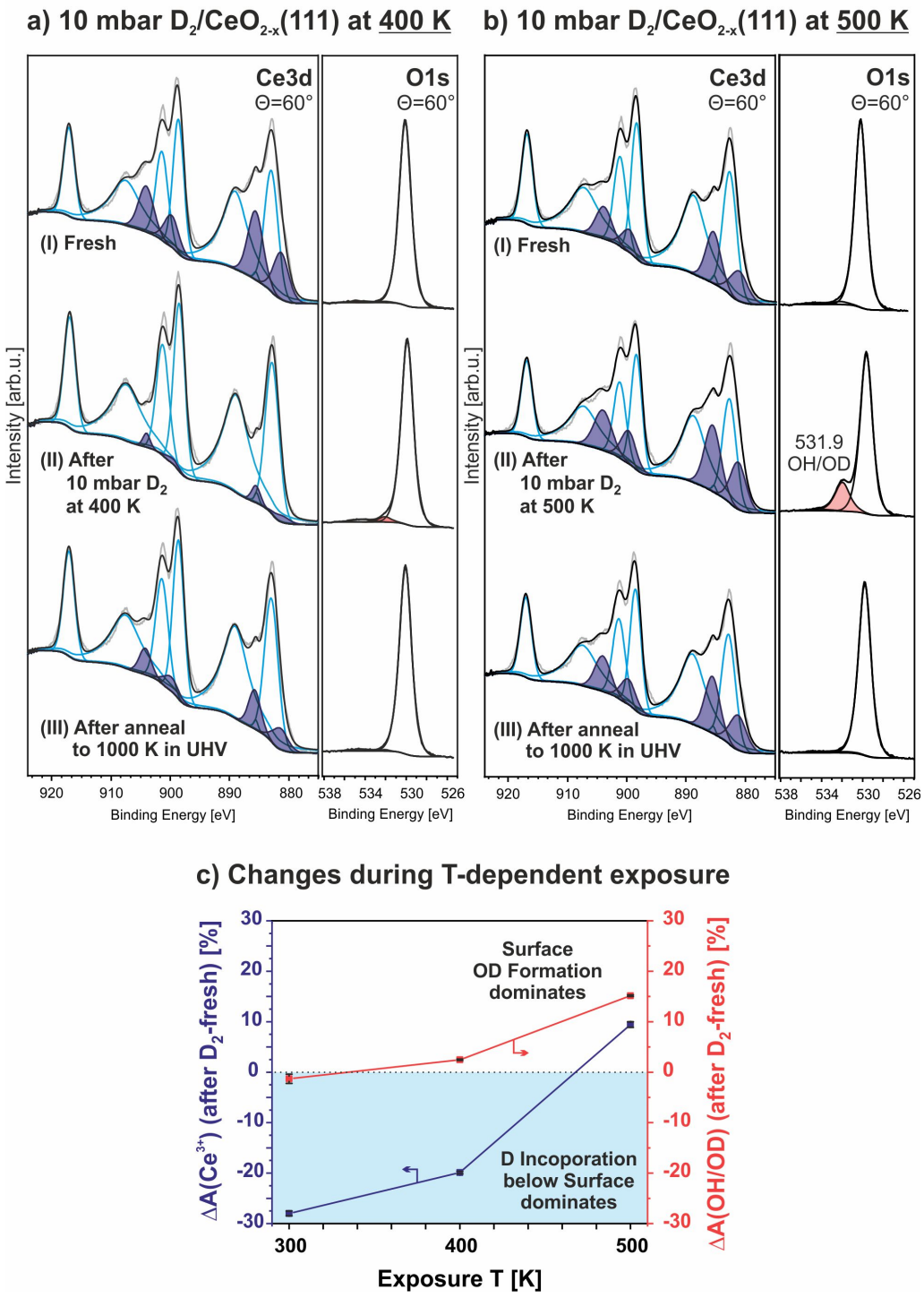

Fig. 4.16: a)+b) Grazing emission Ce 3d and O 1s XP spectra of $CeO_{2-x}(111)$ before exposure (a) and after exposure (b) to 10 mbar D_2 at indicated temperature. XPS was recorded at 300 K. Spectra (II) are equivalent to the sample state in Fig. 4.15c. c) *Changes* in relative concentration of Ce^{3+} and OD/OH after D_2 exposure as a function of exposure temperature.

CeO_{2-x} bulk cannot be excluded solely from the XPS measurements, it is obvious that the hydroxylation reaction dominates the interaction of D_2 and CeO_{2-x}(111) at this temperature.

Finally, Fig. 4.16(c) summarizes the *changes* in electronic structure observed on CeO_{2-x}(111) after exposure to D_2 between 300 K and 500 K. After D_2 exposure up to T≤400 K, hydrides are incorporated into the oxide, which results in a decrease of the Ce^{3+} concentration. At the same time, only small amounts of hydroxyls are formed. At 500 K exposure temperature, the oxide is further reduced, while hydroxyl groups are formed on its surface. These observations are in line with the computational predictions of Li and coworkers,[144] which predict hydrides within CeO_{2-x}(111) to be stable at low temperature, while they are transformed into thermodynamically favorable surface hydroxyl groups upon heating.

4.5 Conclusions

D_2 interacts with CeO_2(111) in a variety of reaction pathways, depending on the applied pressure and temperature, and, above all, on the presence of O vacancies within the oxide. On stoichiometric CeO_2(111), D_2 dissociates to form surface hydroxyls. On reduced CeO_{2-x}(111), additionally to surface hydroxyls, hydrides may form in O vacancies below the surface.

Dissociation of D_2 on CeO_2(111) is an activated process that occurs at elevated pressure and temperature. Too high temperatures, however, yield small hydroxyl concentrations due to recombinative desorption of hydroxyls as water. This leads to the formation of O vacancies and to a reduction of the CeO_2(111) surface.
Hydride formation within reduced CeO_{2-x}(111) occurs at temperatures up to 400 K and is thermally reversible. The extent of hydride formation may be traced following changes in the electronic structure of the oxide, since the reaction involves an electron transfer from Ce^{3+} towards a D species, re-oxidizing Ce^{3+} to Ce^{4+}.
Finally, both hydroxyl groups and hydrides may form when reduced CeO_{2-x}(111) is exposed to D_2. In this case, the dominant reaction is determined by the exposure temperature: at low temperatures, mainly hydride formation occurs, while elevated temperatures (T≥500 K) favor hydroxylation.

Our studies illustrate the vast complexity of the interaction of D_2 and CeO_2(111). A complete understanding of the interplay of hydroxyls, hydrides, and O vacancies,

however, may only be achieved by further thorough investigation of well-defined CeO_2 samples. In light of the promising applications for CeO_2 in catalysis, e.g. in hydrogenation and dehydrogenation reactions, a better understanding of these fundamental interactions is highly desirable.

5 $CO_2/CeO_2(111)$ and $CeO_{2-x}(111)$

The adsorption of CO_2 onto CeO_2 is part of many catalytic reactions.[6, 7, 10] In addition, CO_2 is often present as an impurity in the gas feed, from which it may adsorb onto the oxide surface and thus affect its reactivity. This is apparent, for example, in the H_2 adsorption experiments presented in chapters 3 and 4. This chapter aims at gaining further insights into the chemical nature of CO_2 adsorbates on $CeO_2(111)$, and particularly into their interplay with O vacancies.

5.1 Literature Survey

Theoretical studies on the adsorption of CO_2 on $CeO_2(111)$ identified three major adsorption modes (see Fig. 5.1, top): chemisorption as a 'mono'- or bidentate carbonate and physisorption of linear CO_2.[147–149] Of these, the monodentate carbonate binds strongly to a surface O ion, from which it accepts electron density. Since the distance in between surface O ions is large (∼3.8 Å), Ce ions from the second layer coordinate to the O atoms of the CO_2 entity, causing a planar tilting towards the surface.[147] The term 'monodentate' hence may be misleading, since this species is actually coordinated to three surface ions. Bidentate carbonates, which are less stable, bind to a surface O ion and coordinate only to one underlying Ce ion, resulting in a sideways tilted geometry.
The binding energy of CO_2 on $CeO_2(111)$ is predicted to depend crucially on the surface coverage.[147] Since the surface has limited capacity to donate electrons to the adsorbates, the stability of carbonates decreases with coverage. The most stable ensemble at higher coverage has been predicted as monodentate carbonates on one third of the surface, with additional physisorbed CO_2 present.

On reduced $CeO_{2-x}(111)$, computational studies predict stronger binding of CO_2 due to a larger electron density close to O vacancies.[148, 149] The presence of O vacancies also allows for other forms of CO_2 adsorption. Among the predicted adsorbates are carbonates, carboxylates, and bent $CO_2^{\delta-}$ species (see Fig. 5.1, bottom). A bent $CO_2^{\delta-}$ species which occupies the O vacancy with its C atom, is predicted to be the most stable adsorbate, followed by carbonates on O sites neighboring O vacancies.

Experimentally, various studies have investigated the adsorption of CO_2 onto CeO_2 *powders*.[151–155] They typically assign IR and XPS features of chemisorbed CO_2 to

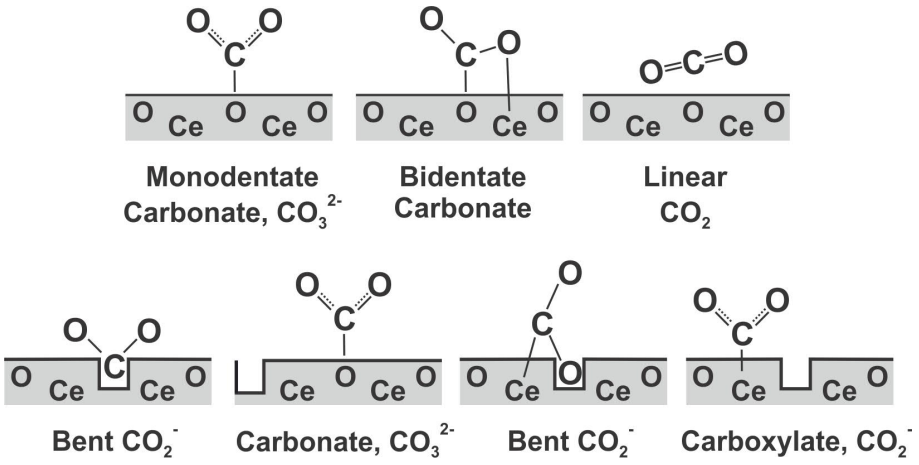

Fig. 5.1: CO_2 adsorbates proposed on $CeO_2(111)$ and $CeO_{2-x}(111)$.[147–150]

carbonate species. The observed signals, however, differ substantially between the studies. Since the morphology of the CeO_2 surface determines the type of adsorbates formed,[156] and since in these studies the surface morphology is largely unknown, we focus in the following on studies performed on well-defined $CeO_2(111)$.
On atomically well-ordered CeO_2 surfaces, only few experimental studies are available. From these, it is apparent that CO_2 interacts weakly with CeO_2 and predominantly physisorbs at low temperature.[150, 157] On $CeO_2(100)$ and reduced $CeO_{2-x}(100)$, Mullins et al. identify chemisorbed CO_2 as a tilted tridentate carbonate,[158] similar to the 'monodentate' carbonate proposed on $CeO_2(111)$.[147, 149] On $CeO_2(111)$, chemisorbed CO_2 species have been assigned to carbonates and carboxylates by photoelectron spectroscopy.[150, 157, 159–161] Ernst and coworkers[150] investigated the adsorption of CO_2 on stoichiometric $CeO_2(111)$ and reduced $CeO_{2-x}(111)$ surfaces by IRAS and assigned a vibrational feature at 1292 cm^{-1} on both surfaces to a carboxylate species formed close to an O vacancy. Overall, the controversy on the chemical nature of CO_2 adsorbates on $CeO_2(111)$ could not yet be resolved.

5.2 Adsorption of CO_2 on $CeO_2(111)$ and $CeO_{2-x}(111)$

To achieve better understanding of the adsorption behavior of CO_2, we first studied its adsorption onto stoichiometric $CeO_2(111)$. Fig. 5.2 shows IRAS spectra of $CeO_2(111)$ after exposure to various doses (0.1-1.0 L) of CO_2 at 90 K.

At a dose of 0.1 L CO_2, a strong band at 2356 cm^{-1} with a shoulder at 2340 cm^{-1} dominates the IRAS spectrum. Additionally, weak bands arise at 1291 cm^{-1} and 1377 cm^{-1}. All bands grow in intensity with increasing CO_2 dose. The band at 2356 cm^{-1} drastically gains in intensity and shifts to 2360 cm^{-1} at 1.0 L exposure. These results are very similar to the adsorption experiments by Ernst and coworkers.[150]
The bands at 2356 cm^{-1} and 2340 cm^{-1} are very close in frequency to the asymmetric stretch of the CO_2 molecule in gas phase.[131, 162] We therefore assign these bands to physisorbed CO_2. The observed shift of the 2356 cm^{-1} band at increasing dosage may be attributed to coverage effects.
Vibrations of CO_2 adsorbates below 1700 cm^{-1} are typical of chemisorbed CO_2.[131, 162] In this region, we observe two bands, one at 1291 cm^{-1}, and a weaker one at 1377 cm^{-1}. As can be seen from a plot of their respective integrated peak area (see Fig. 5.3), both peaks grow approximately linearly with increasing dosage. Since they arise at about the same coverage and grow in intensity at the same rate, these bands may arise from the same surface species.

CO_2 adsorption on reduced $CeO_{2-x}(111)$ yields very similar features (see Fig. 5.4, top). At 0.1 L CO_2 exposure, bands of chemisorbed and physisorbed CO_2 adsorbates are apparent (physisorbed region not shown). As on $CeO_2(111)$, a vibrational band arises at 1291 cm^{-1}, albeit in slightly smaller intensity. After 1.0 L CO_2 exposure, this band grows and slightly shifts to 1296 cm^{-1}, most likely due to adsorbate interactions at high coverage. Also here, a small vibrational feature arises at 1377 cm^{-1}. Different than on $CeO_2(111)$, a weak and broad band around 1600 cm^{-1} appears after 1.0 L CO_2 exposure. In addition, certain changes are apparent in the $\nu(OH)$ region. 'Negative' bands appear, which indicate that OH species were adsorbed in the reference spectrum before CO_2 exposure. With 1.0 L CO_2 dosage, hence by interaction with CO_2, these OH bands shift to lower wavenumbers. This shift generates an S-shaped feature, as it is visible in the IRAS spectra.

Comparing the vibrational bands of CO_2 adsorbates on stoichiometric $CeO_2(111)$ and reduced $CeO_{2-x}(111)$, the similarities between them are striking. The vibrational band at 1296 cm^{-1} is intense and sharp in both cases, and therefore very unlikely to originate from adsorbates on defects. The similar intensities of the band on $CeO_2(111)$ and $CeO_{2-x}(111)$ furthermore suggests that the origin of this band is not dependent on the presence of O vacancies.

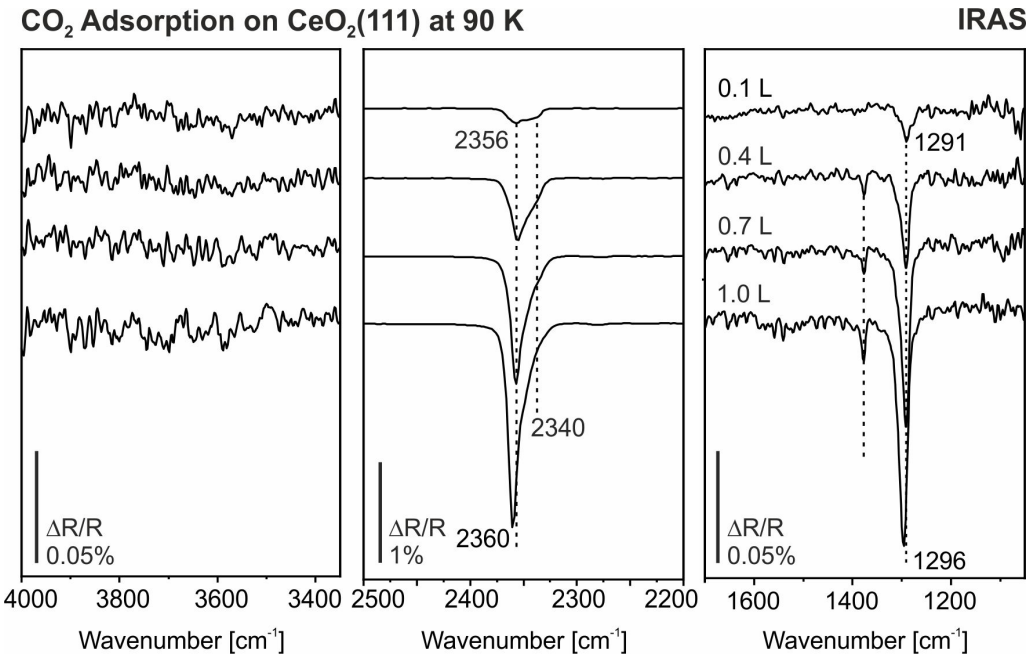

Fig. 5.2: IRAS spectra recorded upon adsorption of CO_2 on $CeO_2(111)$ at 90 K. Three regions are shown (from left to right: OH, physisorbed CO_2, and chemisorbed CO_2). Please note that the physisorbed CO_2 region (middle panel) is shown with a different intensity scale.

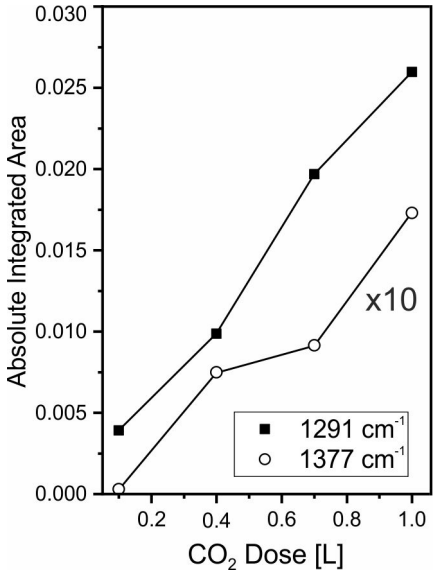

Fig. 5.3: Integrated area of vibrational bands at 1291 cm^{-1} and 1377 cm^{-1} (shown in tenfold intensity) as a function of CO_2 dosage. The integrated area was calculated from spectra shown in Fig. 5.4.

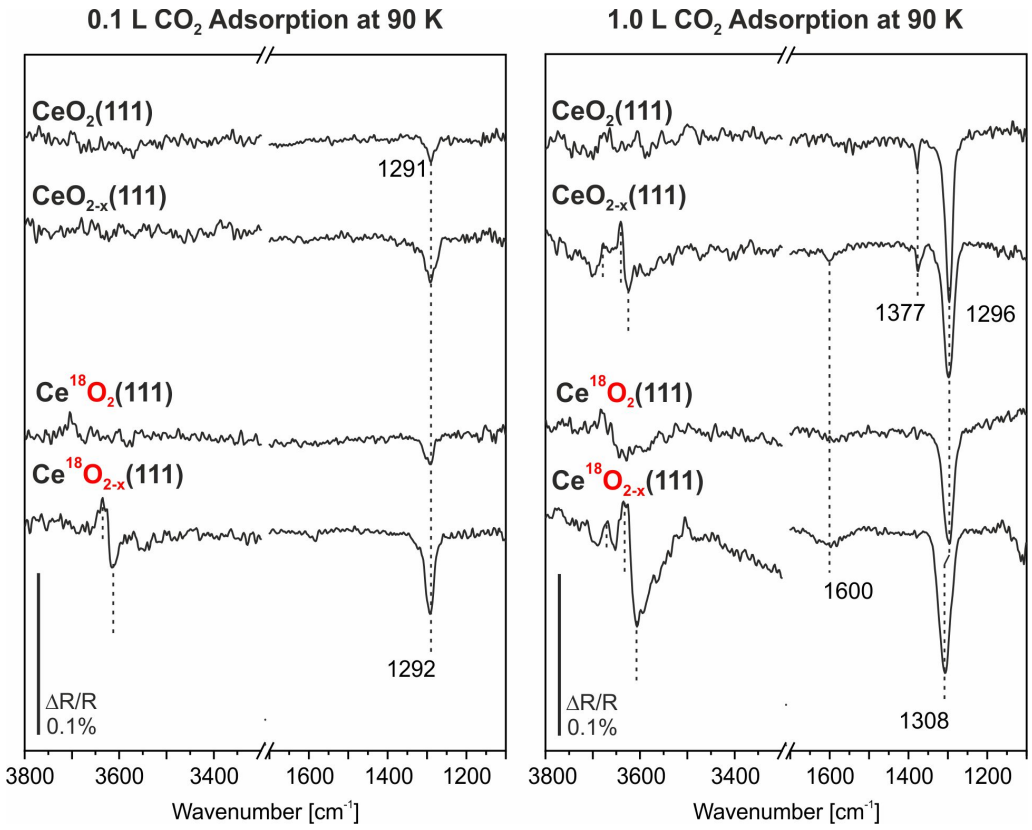

Fig. 5.4: IRAS spectra recorded after adsorption of 0.1 L (left) and 1.0 L CO_2 (right) on various $CeO_2(111)$ surfaces at 90 K. As typical for IRAS, the spectra are divided by a reference spectrum of the surface recorded before exposure.

Chemisorption of CO_2 on oxide surfaces results in most cases in the formation of carbonates (CO_3^{2-}) or bicarbonates ($CO_2(OH)^-$). On strongly basic or defective oxides, also carboxylate (CO_2^-) formation is possible.[131, 162] Differentiation between these species is often not trivial, since they give rise to similar vibrational bands. Since *carboxylate* formation involves charge transfer from Ce^{3+} to CO_2, which is not possible on stoichiometric $CeO_2(111)$, we exclude that the present vibrations are related to a carboxylate species. In the same way, we exclude the arising vibrational bands to originate from bent $CO_2^{\delta-}$ species (adsorbed into O vacancies) as they were proposed theoretically.[149]

A clear difference between the spectra on stoichiometric $CeO_2(111)$ and reduced $CeO_{2-x}(111)$ after exposure to CO_2 is the presence of OH bands only on the reduced surface, which agrees with our previous observations. In chapter 3, we showed that residual water easily dissociates at O vacancies. Here, the presence of OH groups on

reduced $CeO_{2-x}(111)$ as opposed to the OH-free $CeO_2(111)$ does influence neither the frequencies nor the intensities of the vibrational bands. Furthermore, we observed the same vibrational frequencies in another experiment, where CO_2 was dosed onto an OD-covered $CeO_{2-x}(111)$ surface (not shown). Based on this observation and similar results in comparative studies on other oxides,[133, 163] we conclude that no strong interactions take place between co-adsorbed hydroxyl groups and CO_2 adsorbates and consider *bicarbonate* formation on the $CeO_2(111)$ and $CeO_{2-x}(111)$ surfaces as unlikely.

Monodentate carbonate species on well-defined metal oxides give rise to a series of vibrational bands (see Table 5.1). The vibrational band at 1291 cm^{-1} corresponds to the carbonate's $\nu_s(OCO)$ vibration on other oxides (1370-1298 cm^{-1}). In the frequency region of the $\nu_{as}(OCO)$ vibration (~1600 cm^{-1}), we do not observe any feature on stoichiometric $CeO_2(111)$, but a broad and weak feature on reduced $CeO_{2-x}(111)$. The absence of this feature on $CeO_2(111)$ may be explained by the geometry of the 'monodentate' carbonate: The dipole vector of the $\nu_{as}(OCO)$ vibration is oriented parallel to the surface and thereby not detectable according to IRAS selection rules. On reduced CeO_{2-x}, a slightly inclined geometry of the carbonate, possibly due to the interaction with defects, may explain the appearance of the $\nu_{as}(OCO)$ vibrational band. The origin of the weak vibrational band at 1377 cm^{-1} remains unclear.

	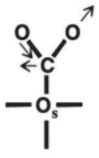 $\nu_{as}(OCO)$	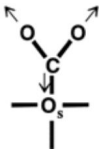 $\nu_s(OCO)$ $+\nu(CO^{surf})$	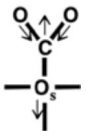 $\delta(OCO)$	
General Range	1530-1470	1370-1300	1080-1040	[164]
CO_2/CaO(001)	1520	1319-1298	991-985	[163, 165]
CO_2/OH-CaO(001)	-	1382-1366	1020	[163]

Table 5.1: Vibrational frequencies [cm^{-1}] of monodentate carbonate on well-ordered oxide surfaces.

To further investigate the interaction of CO_2 with $CeO_2(111)$, we performed equivalent exposure experiments on isotopically labeled $Ce^{18}O_2(111)$ and $Ce^{18}O_{2-x}(111)$ surfaces. The corresponding IRAS spectra are shown in Fig. 5.4. At a low exposure

of 0.1 L CO_2, the vibrational spectra on the isotopically labeled surfaces are very similar to the ones obtained on $Ce^{16}O_2$(111) and $Ce^{16}O_{2-x}$(111). On both isotopically labeled surfaces, a single peak of chemisorbed CO_2 arises at 1292 cm^{-1}.

On reduced $Ce^{18}O_{2-x}$(111), the vibrational band of pre-adsorbed OH shifts to lower wavenumbers with increasing dosage of CO_2. As for non-labeled $Ce^{16}O_{2-x}$(111) at high exposure, we attribute this phenomenon to the relocation of OH species towards less reduced sites upon interaction with CO_2. The fact that this takes place already at low exposure here may be explained by a slightly increased density of O vacancies on the $Ce^{18}O_{2-x}$(111) surface as opposed to $Ce^{16}O_{2-x}$(111), or a slightly increased dosage of CO_2 during the experiment. Please note that the OH vibrational frequencies here slightly differ from the values observed for OH formation on $Ce^{16}O_2$(111) in chapters 3 and 4, since here the (partially) contributing lattice O is isotopically labeled. The shift of the OH vibrational bands to lower frequencies verifies the isotopic nature of the $Ce^{18}O_2$(111) and $Ce^{18}O_{2-x}$(111) films.

After 1.0 L CO_2 exposure, the band at 1292 cm^{-1} increases in intensity and shifts to higher wavenumbers on both isotopically labeled surfaces. In comparison to the experiments on the non-labeled surfaces, the band appears broadened. In addition, especially on reduced $Ce^{18}O_{2-x}$(111), a band at 1600 cm^{-1} is apparent. Different to the non-labeled films, no band arises at 1377 cm^{-1}.
More intense bands in the OH region are apparent on reduced $Ce^{18}O_{2-x}$(111) as compared to reduced, but non-labeled $Ce^{16}O_{2-x}$, which we ascribe to slightly different O vacancy densities of the individual films before exposure.

In collaboration with our group, Olivier Matz and Prof. Monica Calatayud-Antonino of the Sorbonne Université Paris investigated the stability of various CO_2 adsorbates on stoichiometric CeO_2(111) and reduced CeO_{2-x}(111) by DFT+U calculations.[166]*

*For the theoretical studies, several different surface models have been investigated: stoichiometric CeO_2(111), a slightly reduced model ($CeO_{1.86}$(111)), an intermediate model ($CeO_{1.71}$(111)), and a fully reduced model ($CeO_{1.5}$(111)). CeO_2(111), $CeO_{1.86}$(111), and $CeO_{1.71}$(111) have been built by removing none, one, or two O atoms from a $(\sqrt{7}\times\sqrt{7})$R19.1° supercell. $CeO_{1.5}$(111) was built from a (4×4) supercell by removal of eight O atoms. Calculations were performed using the projector augmented wave (PAW) method, as it is implemented in the Vienna ab initio simulation package (VASP). The generalized gradient approximation was used with the Perdew-Burke-Ernzerhof (PBE) functional. The on-site Coulomb interactions of Ce 4f electrons were corrected by implementation of a Hubbard-like U term (U_{eff}=5.0 eV), following the approach of Dudarev et al.[167] Vibrational frequencies were calculated by diagonalization of the Hessian matrix, i.e. in the harmonic approximation.

The stability of the different species was calculated via their adsorption energy:

$$E_{ads} = E_{products} - E_{reactants} \quad (5.1)$$

$$E_{ads} = E_{CeO_{2-x},CO_{2(ads)}} - (E_{CeO_{2-x}} + E_{CO_{2(gas)}}) \quad (5.2)$$

The results of this study are summarized in Table 5.2. Computationally, the energetically most stable CO_2 adsorbate on stoichiometric CeO_2(111) is a tridentate carbonate (see Fig. 5.5a). In this configuration, CO_2 adsorbs as a carbonate with C on top of a surface O ion, while both O atoms of CO_2 coordinate to neighboring Ce species. This configuration is similar to the 'monodentate' carbonate species, which has been predicted as the most stable adsorbate in previous computational studies.[147, 149] A less favorable, but still thermodynamically stable configuration is a bidentate carbonate, in which C binds to a surface O atom, but only one O atom of the CO_2 entity coordinates to an underlying Ce species. Monodentate carbonates, in which the O atoms of the CO_2 entity do not coordinate to surface Ce ions, are not stable on CeO_2(111) and immediately evolve to bi- or tridentate carbonates. Carboxylates do not form on CeO_2(111).

Adsorbate	$E_{ads}(CO_2)$ [eV]			
	CeO_2(111)	$CeO_{1.86}$(111) (OV s/ss)	$CeO_{1.71}$(111)	$CeO_{1.5}$(111)
Linear CO_2	+0.09	+0.01/+0.28	-0.23	-0.24
Carbonate, mono-	evolves to bi-/tridentate carbonate			
Carbonate, bi-	-0.66	-0.82/-0.15	-0.35	-0.98
Carbonate, tri-	-0.94	-1.10/-0.58	-1.06	-1.60
Carboxylate, tri-	-	+0.56/-	+0.18	-0.17

Table 5.2: DFT+U calculated adsorption energies for selected CO_2 adsorbates on CeO_2(111) and CeO_{2-x}(111) surfaces with various O vacancy (OV) densities. s = surface, ss = subsurface, mono-/bi-/tri- = (mono-/bi-/tri-)dentate.[166]

Four prominent vibrational modes of the tridentate carbonate, as computed by Matz and Calatayud-Antonino, are shown schematically in Fig. 5.5a. The topmost plot of Fig. 5.5b displays a simulated IR spectrum on CeO_2(111).[166] The vibrations accessible with our IRAS setup are the antisymmetric (ν_{as}(OCO)) and symmetric stretching (ν_s(OCO)) vibrations of the CO_2 entity. They are predicted with frequencies of 1603 cm^{-1} and 1261 cm^{-1}, respectively. Since the dipole vector of the

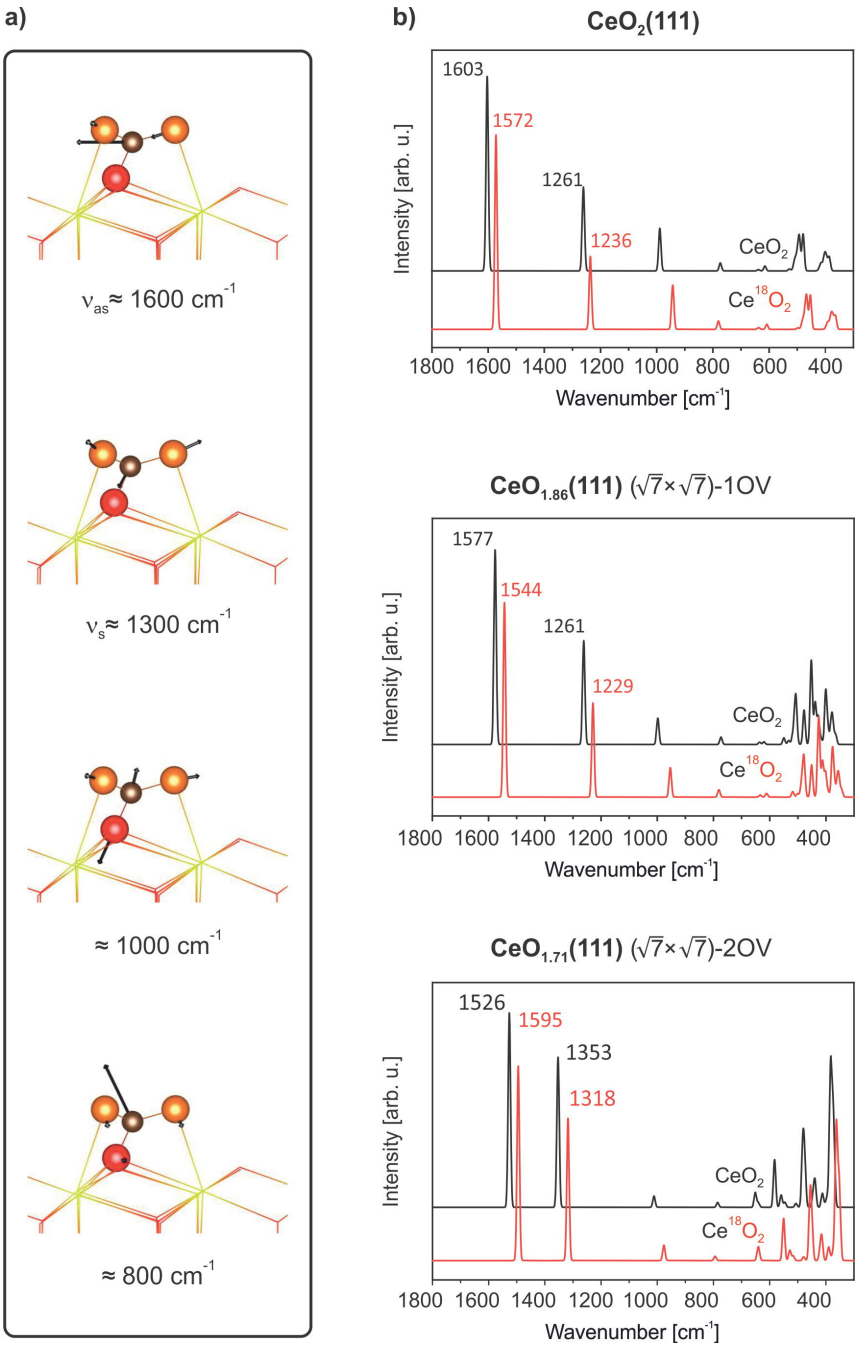

Fig. 5.5: a) Computed adsorption geometry and vibrations of tridentate carbonate on $CeO_2(111)$. For clarity, the majority of the $CeO_2(111)$ surface is represented as sticks with red (O) and yellow (Ce) crossings. The main species involved in carbonate bonding are shown as red (surface O), brown (C), and orange (O of CO_2). b) Simulated IR spectra of tridentate carbonate on $CeO_2(111)$, $CeO_{1.86}(111)$, and $CeO_{1.71}(111)$, consisting of ^{16}O and ^{18}O atoms, respectively.[166]

ν_{as}(OCO) vibration is oriented parallel to the surface, we expect this vibration not to be detectable by IRAS. Indeed, no vibration in this frequency region is apparent from the experimental spectra of Fig. 5.2. The symmetric vibration, ν_s(OCO), in contrast, displays a dynamic dipole moment with a large surface-normal contribution, and is thus expected to appear in relatively large intensity in the IRAS spectra. In agreement with these computational results, we tentatively assign the vibrational bands at 1600 cm^{-1} and 1292 cm^{-1} to the asymmetric ν_{as}(OCO) and symmetric ν_s(OCO) stretching vibration of a tridentate carbonate species. The shift of the ν_s(OCO) band to higher frequency at high exposure may be linked either to dipole-dipole interactions or to the theoretically predicted reduced electron transfer from the surface to the carbonate species at high coverage.[147]

The computational studies by Matz and Calatayud-Antonino further address the adsorption of CO_2 onto reduced $CeO_{2-x}(111)$ surfaces. The adsorption energies on reduced surfaces ranging from $CeO_{1.86}(111)$ to fully reduced $CeO_{1.5}(111)$ are shown in Table 5.2.
On reduced $CeO_{2-x}(111)$, as on stoichiometric $CeO_2(111)$, the most stable CO_2 adsorbate is predicted to be a tridentate carbonate species, which forms in close proximity to an O vacancy. Also here, the formation of bidentate carbonate is exothermic, even though not as favorable as the formation of a tridentate carbonate species. Monodentate carbonates are unstable and evolve to bi- and tridentate carbonates. The formation of carboxylates is only favorable on a fully reduced $CeO_{1.5}(111)$ surface. Even there, however, the tridentate carbonate is predicted to be much more stable. A common trend across all investigated adsorbate species is that the presence of O vacancies on the oxide *surface* stabilizes CO_2 adsorbates. The exclusive formation of O vacancies below the oxide surface (as tested for $CeO_{1.86}$), in contrast, destabilizes CO_2 adsorbates.

Computed IR spectra of the tridentate carbonate species on reduced $CeO_{1.86}(111)$ and $CeO_{1.71}(111)$ are shown in Fig. 5.5.[166] According to the calculations, the most O vacancy-sensitive vibration of the tridentate carbonate is the ν_{as}(OCO) vibration, which shifts to lower frequencies with increasing O vacancy density (-26 cm^{-1} for $CeO_{1.86}(111)$, -77 cm^{-1} for $CeO_{1.71}(111)$). The ν_s(OCO) vibration stays unchanged on $CeO_{1.86}(111)$ as compared to stoichiometric $CeO_2(111)$, but is predicted to shift by about +90 cm^{-1} on $CeO_{1.71}(111)$.

Matz and Calatayud-Antonino further computed the vibrational frequencies of the tridentate carbonate species on isotopically labeled $Ce^{18}O_2(111)$ and $Ce^{18}O_{2-x}(111)$.[166] The results of their study are summarized in Fig. 5.5b. On all studied surfaces, the replacement of surface ^{16}O with ^{18}O shifts the $\nu_{as}(OCO)$ and $\nu_s(OCO)$ vibrations by around -30 cm^{-1}.

Comparing these theoretical predictions to the experimental data reveals an apparent contradiction. Whereas theory predicts a shift in vibrational frequency of the tridentate carbonate $\nu_s(OCO)$ band on both isotopically labeled surfaces, no such shifts were observed experimentally. At this point, the disagreement between theory and experiment cannot be fully resolved and requires future careful investigations. Nevertheless, we consider the assignment of the observed vibrational bands to carbonate species as most likely.

5.3 Thermal Stability of Adsorbed CO_2 on $CeO_2(111)$ and $CeO_{2-x}(111)$

Next, we investigated the thermal stability of adsorbed CO_2 on $CeO_2(111)$. To do so, we heated the 1.0 L CO_2-exposed $CeO_2(111)$ surface (see Fig. 5.2) in UHV to temperatures between 200 K and 400 K. Fig. 5.6a shows IRAS spectra recorded at 90 K in between heating steps.

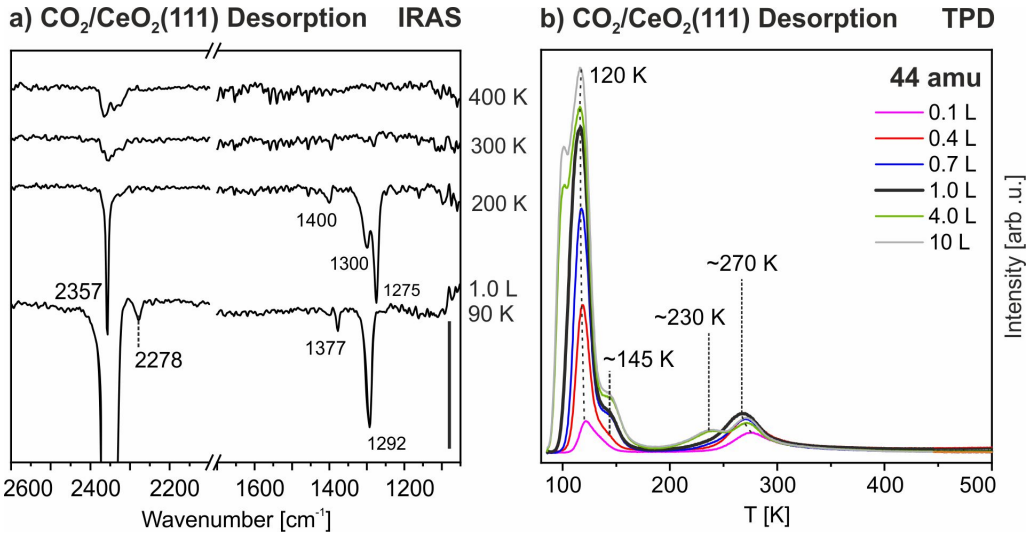

Fig. 5.6: a) IRAS spectra recorded at 90 K after adsorption of 1.0 L CO_2 on $CeO_2(111)$ and consecutive heating to indicated temperatures. b) 44 amu (CO_2-)TPD trace after adsorption of 0.1-10 L CO_2 on $CeO_2(111)$ at 90 K.

After heating to 200 K, almost all signal of physisorbed CO_2 disappears. A small band at 2357 cm^{-1} prevails, most likely due to re-adsorption of CO_2 from the UHV background upon cooling to 90 K. The vibrational band at 1292 cm^{-1} splits into two bands at 1300 cm^{-1} and 1275 cm^{-1}, while the band at 1377 cm^{-1} shifts to 1400 cm^{-1}. Both effects might be related to the desorption of physisorbed CO_2 and a possible rearrangement of carbonates in different chemical environments on the surface. After heating to 300 K, all vibrational bands on the surface disappear, which indicates complete desorption of CO_2 adsorbates.

In a complementary experiment, we exposed the $CeO_2(111)$ surface to various dosages of CO_2 (0.1-10 L) and followed desorption by TPD (see Fig. 5.6b). CO_2 desorbs in two temperature regimes at 110-150 K and 200-300 K, corresponding to the desorption of physisorbed and chemisorbed CO_2, respectively. Already for the smallest dose of 0.1 L, desorption of both physisorbed and chemisorbed CO_2 is apparent at 120 K and 270 K, respectively. After a 0.4 L dose, the peak area of the 270 K feature increases, indicating an increased amount of chemisorbed CO_2. The shift of this peak to lower temperatures with increasing exposure shows a decrease in stability of chemisorbed CO_2, which likely results from repulsive interactions between the adsorbates at high coverage.[147] At exposures of 4.0 L and 10.0 L, an additional desorption peak of a chemisorbed species arises at ∼230 K on the expense of the peak at 270 K. This may indicate that a fraction of the adsorbates is converted into another chemisorbed species at high coverage. In light of the DFT+U calculations, the adsorbates desorbing at ∼270 K and ∼230 K may be tentatively assigned to tri- and bidentate carbonates, respectively.
From a dose of 0.4 L on, a tail to the TPD feature for physisorbed CO_2 evolves at ∼145 K, which becomes more prominent at higher exposure. This feature may possibly be assigned to physisorbed CO_2, stabilized by interaction with chemisorbed CO_2,[147] which may also be the origin of a weak vibrational band at 2278 cm^{-1} in the IRAS spectra. From a dose of 4.0 L on, an additional desorption peak appears at 110 K, which we assign to CO_2 adsorbed in further physisorbed layers.

Adsorbed CO_2 on reduced $CeO_{2-x}(111)$ shows a different behavior upon heating. Fig. 5.7a compares CO_2 TPD traces on stoichiometric $CeO_2(111)$ and reduced $CeO_{2-x}(111)$ after exposure to 1.0 L CO_2 at 90 K.
The desorption of physisorbed CO_2 happens on both surfaces around the same temperature of 115-120 K. On reduced $CeO_{2-x}(111)$, however, the desorption peak is tailing to higher temperatures, which indicates the presence of more strongly

bound species, possibly by physisorption at defects. The desorption behavior of chemisorbed species is affected by the presence of O vacancies. Instead of a single desorption peak at ~270 K, as was observed on stoichiometric $CeO_2(111)$, two broad desorption peaks arise at ~260 K and ~320 K. The increased desorption temperature indicates an increased stability of chemisorbed species near O vacancies, as it has been proposed in the literature[147, 149, 155] and by the DFT+U studies of Matz and Calatayud-Antonino (see Table 5.2).[166]

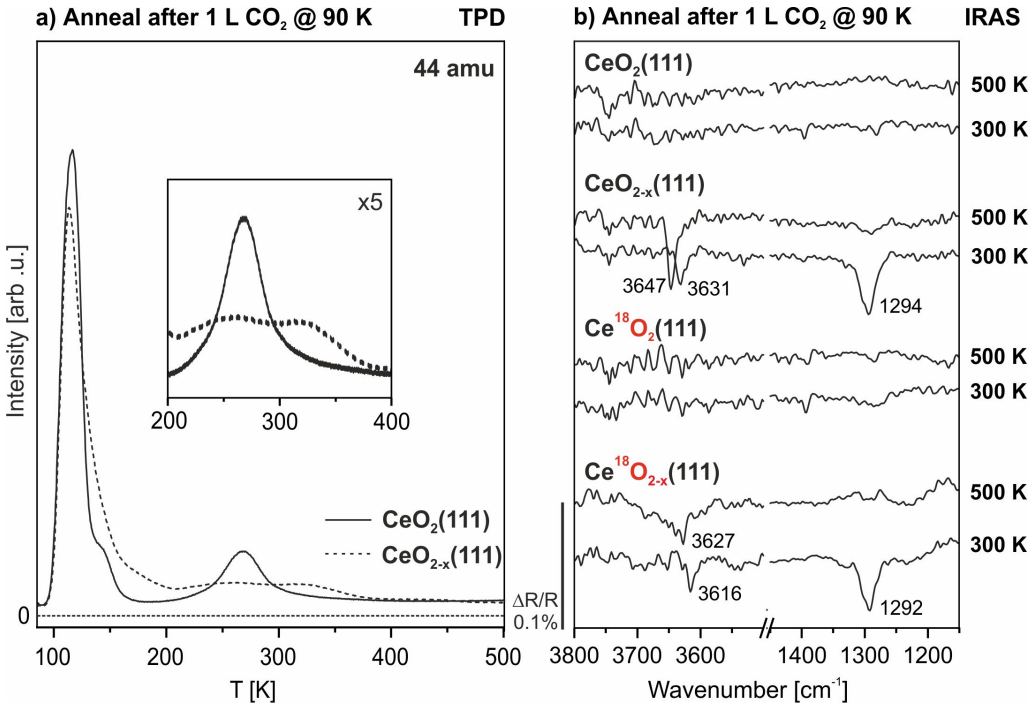

Fig. 5.7: a) 44 amu TPD traces recorded after exposure of stoichiometric $CeO_2(111)$ and reduced $CeO_{2-x}(111)$ to 1.0 L CO_2 at 90 K. The inset shows an fivefold magnified view of the temperature range 200-400 K. b) IRAS spectra recorded after heating various 1.0 L CO_2-exposed surfaces to 300 K and 500 K, respectively. IRAS spectra were recorded at 100 K after cooling the samples in vacuum. The employed reference spectrum was recorded before CO_2 exposure for each sample.

The increased stability of chemisorbed adsorbates near O vacancies is also apparent when comparing IRAS spectra of 1.0 L CO_2-exposed $CeO_2(111)$ and $CeO_{2-x}(111)$ surfaces upon heating (see Fig. 5.7b). While no adsorbate vibrations remain on stoichiometric $CeO_2(111)$ after heating to 300 K, a weak vibrational band at 1294 cm^{-1} persists on reduced $CeO_{2-x}(111)$.

In addition to CO_2 adsorbates, OH(I) groups (3631 cm^{-1}) are present on reduced $CeO_{2-x}(111)$ after heating to 300 K. We assign these to originate from residual H_2O that dissociates over O vacancies upon desorption of carbonates at 260 K.
After heating the reduced $CeO_{2-x}(111)$ film to 500 K, no carbonate vibrations remain, indicating complete desorption. At the same time, the OH bands increase in intensity and shift to a higher frequency, which points towards the relocation of OH to more reduced local environments.

The same trends are observable on the labeled $Ce^{18}O_2(111)$ and $Ce^{18}O_{2-x}(111)$ surfaces. Also here, all adsorbates desorb from stoichiometric $Ce^{18}O_2(111)$ upon heating to 300 K. On reduced $Ce^{18}O_{2-x}(111)$, a small fraction of carbonates is stable at 300 K, but vanishes at 500 K.

5.4 Conclusions

CO_2 interacts similarly with stoichiometric $CeO_2(111)$ and reduced $CeO_{2-x}(111)$. On both surfaces, CO_2 may adsorb strongly, with desorption temperatures up to 350 K. The vibrational structure of CO_2 adsorbates is identical on both surfaces. On reduced $CeO_{2-x}(111)$, however, chemisorbed CO_2 adsorbates are more strongly bound due to an interaction with O vacancies.

On the basis of our experiments and the DFT+U results of Olivier Matz and Monica Calatyud-Antonino, we tentatively assign the chemisorbed species to carbonates. In an attempt to verify the chemical identity of the carbonates, we followed the adsorption of CO_2 onto isotopically labeled $Ce^{18}O_2(111)$ and $Ce^{18}O_{2-x}(111)$ surfaces by IRAS. In contrast to the theoretical predictions, however, we observed no frequency shift of the presumed $\nu_s(OCO)$ vibrational band. This controversy between theoretical and experimental results may be cleared only by future investigations.

A summary of our adsorbate assignments, together with the attributed vibrations and desorption temperatures, is given in Table 5.3.

Surface Species	Associated vibrations [cm^{-1}]	Desorption T
CO_2 linear, 2^{nd}+ layer	2360 ν_{as}(O=C=O)	110 K
CO_2 linear, 1^{st} layer	2360 ν_{as}(O=C=O)	115-120 K
CO_2 linear/ad-species	2278 ν_{as}(O=C=O)	145 K
Chemisorbed CO_2 (possibly tridentate carbonate)	1600 ν_{as}(OCO) 1300-1291 ν_{s}(OCO)	270-320 K

Table 5.3: Summary of vibrational frequencies and desorption characteristics of CO_2 adsorbates on $CeO_2(111)$ and $CeO_{2-x}(111)$.

6 Interaction of Hydrogen and Propyne on CeO_2(111)

Recently, CeO_2 has been reported to act as a catalyst in the selective hydrogenation of alkynes to alkenes.[11–14] Not only is the catalytic activity of CeO_2 in the hydrogenation reaction unusual for an oxide, but even more so, CeO_2 has been reported to surpass the commercially used Pd catalysts in both activity and selectivity.[13] To gain further insights into the alkyne hydrogenation reaction, we investigate in the following how H_2 and propyne (C_3H_4) interact on an atomically well-defined CeO_2(111) surface.

6.1 Literature Survey

6.1.1 Adsorption of Alkynes on CeO_2

Theoretical studies on acetylene (C_2H_2)[14, 168] and propyne (C_3H_4)[15] adsorption on CeO_2(111) predict weak interaction of the alkynes with the oxide surface. The alkynes adsorb likely as a weakly stabilized π-complex on top of a lattice O ion.

When activated, strongest binding to the surface may be achieved by homolytic dissociation of the alkyne on top of two adjacent surface O ions, forming a hydroxyl group and an O-bound acetylide species (O−C≡C−R, with R=H/Me). At the same time, two Ce^{4+} ions are reduced to Ce^{3+}:

$$\mathrm{RC{\equiv}CH} + 2\,\mathrm{O^{lattice}} + 2\,\mathrm{Ce^{4+}} \longrightarrow \mathrm{R\text{-}C{\equiv}C\text{-}O^{lattice}_{ads}} + \mathrm{HO^{lattice}_{ads}} + 2\,\mathrm{Ce^{3+}} \qquad (6.1)$$

The redox-neutral heterolytic dissociation reaction, on the other hand, has been predicted to be endothermic:

$$\mathrm{RC{\equiv}CH} + \mathrm{O^{lattice}} + \mathrm{Ce^{4+}} \longrightarrow \mathrm{R\text{-}C{\equiv}C\text{-}Ce_{ads}} + \mathrm{HO^{lattice}_{ads}} \qquad (6.2)$$

Furthermore, adsorption is possible in form of a weakly bound β-C_2HR radical.[14] On reduced CeO_{2-x}(111), computational modeling predicts molecular adsorption of C_2H_2 to be substantially stronger than on CeO_2(111): In this case, one C atom of the alkyne occupies an O vacancy, while the neighboring C atom is coordinated to an adjacent Ce^{3+} ion.[168]

Only few experimental studies have investigated the interaction of alkynes with CeO_2, mostly focusing on the adsorption of C_2H_2 on CeO_2 *powders*.[14, 108, 168] Presumably, the O-bound acetylide (H-C≡C-$O_{ads}^{lattice}$) is formed upon adsorption at 300 K and shows vibrational features at 3318 cm^{-1} and 2180-2160 cm^{-1}.[14, 108] The Ce-bound acetylide (H-C≡C-$Ce_{ads}^{lattice}$), even though computationally predicted to be unstable, has been assigned to vibrational features at 3262 cm^{-1} and 2037 cm^{-1}. Further vibrational features have been attributed to a di-σ-bound molecular complex.[108] In a controversial study, no vibrational signals of adsorbed hydrocarbons were observed during C_2H_2 adsorption at 300 K.[168] Table 6.1 provides an overview of species associated with adsorbed alkynes and their assigned vibrations on various surfaces.

6.1.2 Selective Hydrogenation of Alkynes on CeO_2

In 2012, Vilé et al. were the first to suggest catalytic activity of CeO_2 in the selective hydrogenation of alkynes to alkenes:[11]

$$RC{\equiv}CH + H_2 \xrightarrow{CeO_2} RHC{=}CH_2 \tag{6.3}$$

The group reported optimal alkyne conversion (96% (86%)) and alkene selectivities (91% (81%)) for the hydrogenation of C_3H_4 (C_2H_2) at 523 K. At higher temperatures, conversion and selectivity decreased. The authors link the decreasing conversion to the formation of O vacancies on the oxide surface, while they assign the decrease in alkene selectivity to the formation of allenes and hydrocarbon oligomers. In consequence, they identified the following reaction conditions as essential for optimal catalytic performance:[11–14]

- high surface area of CeO_2,
- low density of O vacancies (therefore CeO_2(111) as most active surface),
- large excess of H_2 ($p(H_2)$:$p(RC{\equiv}CH)$=30:1),
- reaction temperature above 473 K.

A theoretical study on the hydrogenation of C_2H_2 over CeO_2(111) proposed a **Horiuti-Polanyi-like mechanism**.[14] Thereby, H_2 physisorbs on CeO_2(111), where it dissociates to form two OH species with adjacent surface O ions. C_2H_2 adsorbs on top of a surface O ion as a β-C_2H_2 radical. In a stepwise fashion, two H species are transferred to the adsorbed alkyne from neighboring OH groups. Finally, ethylene (C_2H_4) desorbs as the selective hydrogenation product. Since both the adsorption of H and C_2H_2 as a radical result in reduction of Ce^{4+} to Ce^{3+} species, the reversible

Species	Vib. band [cm^{-1}], assignment	Reference
Free C_3H_4 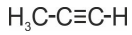	3334 ν(≡C-H)	[169]
	3008-2881 $\nu(CH_3)$	
	2142 ν(C=C)	
	1452 $\delta(CH_3)$	
π-bound complex (on O^{2-} or OH) 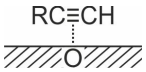	3260-3130 ν(≡C-H)	C_3H_4/ZnO,[170] C_2H_2/various oxides (SiO_2, TiO_2, ZrO_2, Al_2O_3, Sc_2O_3, La_2O_3, CaO, MgO)[171]
	2120 ν(C≡C)	C_3H_4/ZnO[170]
	∼1950 ν(C≡C)	C_2H_2/SiO_2, CaO[171]
di-σ-bound complex 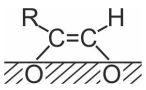	2978 ν(=C-H)	C_2H_2/CeO_2[108]
	1635 ν(C=C)	C_2H_2/CeO_2[108]
	1570-1297 ν(C-O)	C_2H_2/CeO_2[108]
	1437 δ(=C-H)	C_2H_2/CeO_2[108]
M-CH_2-C≡CH Propargyl species 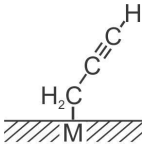	3280 ν(≡C-H)	Propargyl bromide/Ag(111)[172]
	3012 $\nu_{as}(CH_2)$	Propargyl bromide/Ag(111)[172]
	2964 $\nu_s(CH_2)$	Propargyl bromide/Ag(111)[172]
	2123 ν(C≡C)	Propargyl bromide/Ag(111)[172]
	1864 ν_{as}(C=C=C)	C_3H_4/ZnO[170]
	1422 $\delta(CH_2)$	Propargyl bromide/Ag(111)[172]
M-CH=C=CH_2 Allenyle species 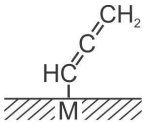	1812 ν_{as}(C=C=C)	Propargyl bromide/Ag(111)[172]
M-C≡C-H 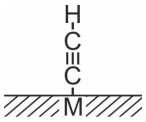	3302-3262 ν(≡C-H)	C_2H_2/CeO_2[108], Al_2O_3, La_2O_3, Ga_2O_3[171]
	2037-1890 ν(C≡C)	C_2H_2/CeO_2[14, 108], Al_2O_3, La_2O_3, Ga_2O_3, ZrO_2[171]
O-C≡C-H 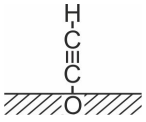	3318 ν(≡C-H)	C_2H_2/CeO_2[108]
	2180-2160 ν(C≡C)	C_2H_2/CeO_2[14, 108]
	1509 ν(C-O)	C_2H_2/CeO_2[108]

Table 6.1: IR signals of free C_3H_4 and chemical species associated with adsorbed alkynes on various surfaces. M=metal, ν=stretching mode, δ=deformation mode, as=asymmetric, s=symmetric.

and flexible redox chemistry of CeO_2 is believed to play a key role in the reaction. For the selective hydrogenation reaction of C_3H_4 over CeO_2(111), a **concerted mechanism** has been proposed.[15] In this mechanism, transfer of two H species takes places simultaneously via a six-membered cyclic transition state, composed of the C_1 and C_2 atoms of the molecularly adsorbed propyne, the H atoms of molecularly adsorbed H_2, and the O and H atoms of a neighboring OH group. The H atom closest to C_1 is added as a hydride from the H_2 species, while the second H is transferred as a proton from the OH group. The calculated energy of this cyclic transition state is ∼1 eV smaller than in the case of a Horiuti-Polanyi mechanism. Experimentally, it has not yet been possible to differentiate between the two mechanisms.[173]

For both mechanisms, two factors are essential for high conversion and selectivity:

Sufficiently high OH coverage. Since adsorbates react with their nearest neighbors, a too small OH coverage may give way to the recombination of neighboring β-C_2H_2 radicals to form oligomers. This effect is associated with the increased production of oligomers at T>523 K[11], triggered by the desorption of adsorbed H species. The dissociation of H_2 on CeO_2 has been identified as the rate-limiting step for the overall hydrogenation reaction.[11, 14, 15, 108]

Availability of O sites. Since H and alkyne species adsorb on top of O sites, the availability of O on the CeO_2 surface limits the overall turnover. This is mirrored in the lower conversion rates on O vacancy-rich CeO_2 surfaces.[11, 12, 15]

6.2 Propyne Adsorption on CeO_2(111)

In a first series of experiments, we investigated the adsorption of propyne (C_3H_4) onto CeO_2(111). Exposure to C_3H_4 above 150 K did not result in any vibrational features observable by IRAS (not shown). IRAS spectra recorded during the adsorption of C_3H_4 at T<130 K are shown in Fig. 6.1. During the initial stages of adsorption, features arise at 3270 cm^{-1}, 2966 cm^{-1}, 2924 cm^{-1}, and 1439 cm^{-1}.* With increasing exposure, further bands develop at 3323 cm^{-1}, 2864 cm^{-1}, and 2117 cm^{-1}. After exposure to ∼10 L of C_3H_4, the IRAS spectrum is dominated by sharp vibrational bands at 3270 cm^{-1} and 1439 cm^{-1}. At high dosages of C_3H_4, a band at 1298 cm^{-1} is apparent, most likely caused by chemisorption of residual CO_2.

*A very broad feature at 3200 cm^{-1}, which is apparent already before exposure, and a later arising feature at 3600 cm^{-1} may be attributed to H_2O ice formation in the IR detector.

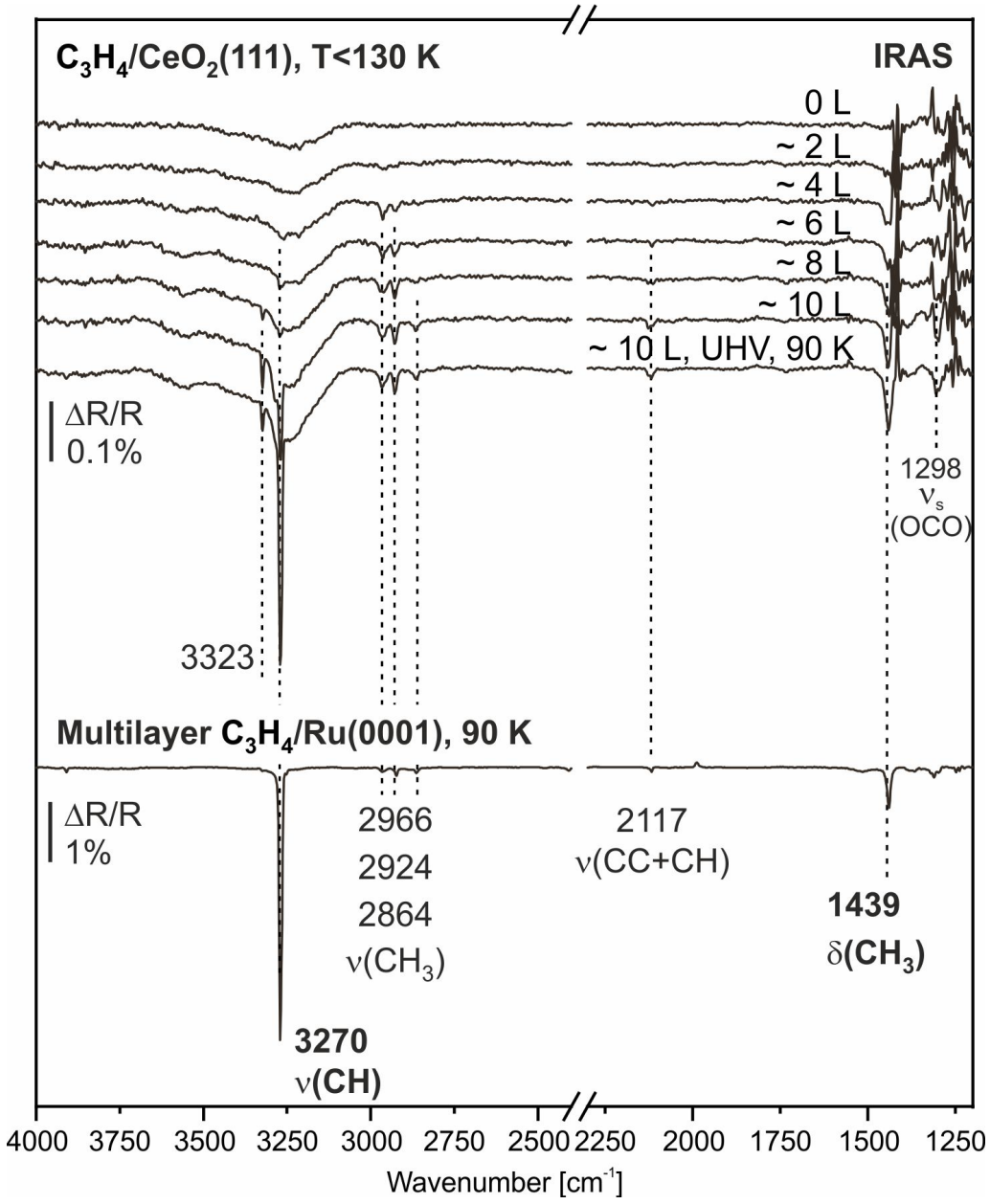

Fig. 6.1: IRAS spectra recorded during exposure of $CeO_2(111)$ to C_3H_4 at T<130 K. An IRAS spectrum of a C_3H_4 multilayer on Ru(0001) is shown for comparison. ν=stretching mode, δ=deformation mode, s=symmetric. Please note that the intensity scales for $C_3H_4/CeO_2(111)$ and $C_3H_4/Ru(0001)$ differ.

By comparison with a multilayer spectrum of C_3H_4 on Ru(0001) (bottom of Fig. 6.1), the features at 3270 cm^{-1} and 1439 cm^{-1} may be attributed to the $\nu(\equiv C-H)$ and the $\delta(CH_3)$ vibration of C_3H_4 in physisorbed multilayers. The similarity of the vibrational frequencies to those of the molecule in gas phase (see Table 6.1) indicates that C_3H_4 undergoes only minor structural changes upon physisorption.[174]

In the sub-monolayer regime, the adsorption of C_3H_4 on $CeO_2(111)$ may take place in four *potential* adsorption modes: (i) molecular adsorption as a π-complex,[14, 15] (ii) molecular adsorption as a σ-bound complex,[108] (iii) dissociative adsorption to form OH and a methacetylide species ($O-C\equiv C-CH_3$ or $Ce-C\equiv C-CH_3$),[14, 15] and (iv) dissociative adsorption to form OH and a propargyl species ($O-CH_2-C\equiv CH$ or $Ce-CH_2-C\equiv CH$)[172].
The vibrational band at 3270 cm^{-1} may be unambiguously attributed to the $\nu(\equiv C-H)$ vibration. With this, adsorption as a σ-complex or as a methacetylide species may be ruled out. Differentiation between a molecularly adsorbed π-complex and a propargyl species is challenging, since they are expected to show very similar vibrational features (see Table 6.1). An expected difference, however, would be the formation of a OH group during dissociation of C_3H_4 into H and a propargyl group. Since we do not observe any distinguishable signal in the OH stretching region (3700-3600 cm^{-1}), we assign the observed features to a weakly bound molecular π-complex. A further indication for this assignment is the low intensity of the observed bands in IRAS, which may be explained by the surface-parallel orientation of the π-complex.

Fig. 6.2 shows TPD traces recorded after adsorption of 0.2 L C_3H_4 on stoichiometric $CeO_2(111)$ and reduced $CeO_{2-x}(111)$, respectively. TPD of 0.2 L $C_3H_4/CeO_2(111)$ results in the desorption of C_3H_4 (40 amu) in a sharp peak with maximal intensity at 140 K. No considerable desorption of C_3H_6 (42 amu) is detectable, which excludes a self-hydrogenation reaction. Traces of H_2O desorb around 200 K, indicating H_2O physisorption from the background.

In line with the IRAS results, the low desorption temperature of C_3H_4 indicates a weak interaction between the alkyne and the $CeO_2(111)$ surface, thus supporting the assignment of a weakly bound π-complex. This result seems to contradict previous experimental studies,[108] which reported alkyne dissociation, yet it is crucial to note that these have been conducted on defect-rich CeO_2 powders with a largely different surface morphology than the present flat and well-defined $CeO_2(111)$ film.

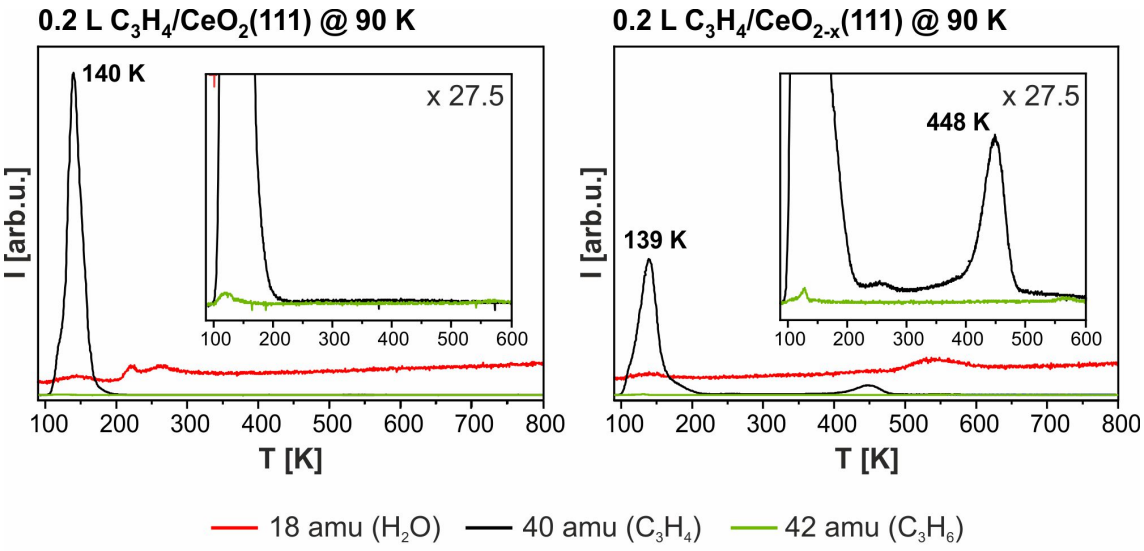

Fig. 6.2: TPD traces of stoichiometric $CeO_2(111)$ (left) and reduced $CeO_{2-x}(111)$ (right), recorded after exposure to 0.2 L C_3H_4 at 90 K.

TPD on reduced $CeO_{2-x}(111)$ after exposure to 0.2 L C_3H_4 shows a substantially different behavior. Here, less C_3H_4 desorbs at ~140 K, as judged from the reduced peak area of the desorption signal. Furthermore, an additional desorption feature arises at ~448 K, which indicates the desorption of a strongly bound alkyne adsorbate. This observation is in line with the computationally predicted strong adsorption of molecular C_3H_4 at O vacancies.[168] Additionally, H_2O desorbing above 500 K indicates the presence of OH groups on the surface, likely formed by dissociation of background H_2O over O vacancies. At this point, it is unclear whether these OH groups influence the adsorption of C_3H_4.

6.3 Interaction of Hydrogen and Propyne on $CeO_2(111)$

6.3.1 Adsorption of Propyne on OD-$CeO_2(111)$

In a first attempt to follow the hydrogenation of C_3H_4 on $CeO_2(111)$, we hydroxylated the oxide surface by exposure to 1×10^{-4} mbar D/D_2 at 220 K, and subsequently exposed it to ~5 L C_3H_4 at T<130 K. Fig. 6.3a shows IRAS spectra recorded after the individual steps of the adsorption experiment.

After exposure of $CeO_2(111)$ to a low pressure of D/D_2 (I), clear hydroxyl features arise in the IRAS spectrum. These features, at 2679 cm^{-1} and 3629 cm^{-1}, corre-

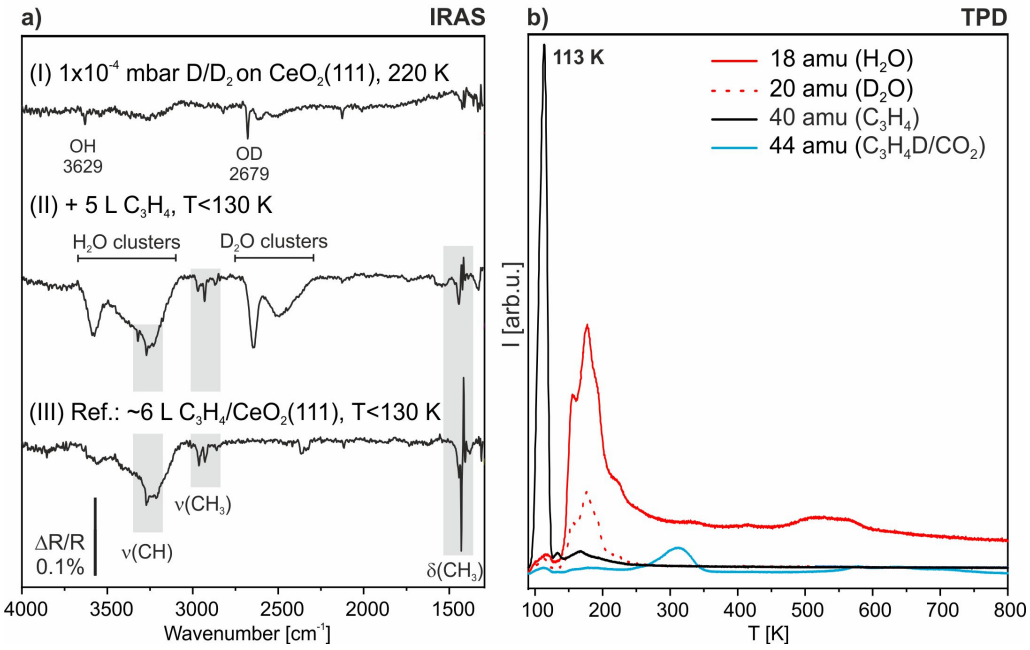

Fig. 6.3: Sequential hydroxylation and C_3H_4 adsorption onto $CeO_2(111)$: a) IRAS spectra recorded after exposure to (I) 1×10^{-4} mbar D/D_2 at 220 K, and (II) additional ~5 L C_3H_4 at T<130 K. (III) ~6 L $C_3H_4/CeO_2(111)$ as reference. C_3H_4 features are highlighted. b) TPD recorded following adsorption experiment shown in a).

spond to the stretching vibrations of surface OD and OH groups, respectively. We attribute the formation of OH groups here to the presence of H_2 traces in the D_2 gas feed. Judging from the intensity ratio of the signals, the amount of OH groups is considerably smaller than the amount of OD groups.
Subsequent adsorption of C_3H_4 at 90 K (II) gives rise to weak additional hydrocarbon features at 3321 cm^{-1}, 3271 cm^{-1}, 2972 cm^{-1}, 2931 cm^{-1}, 2870 cm^{-1}, and 1444 cm^{-1}. These features coincide with the features observed in a reference spectrum of $C_3H_4/CeO_2(111)$ (III). Since the vibrational features of adsorbed C_3H_4 are the same on clean and hydroxylated $CeO_2(111)$, we conclude that no strong interaction takes place between hydroxyls and C_3H_4 adsorbates. In addition to the features of adsorbed C_3H_4, broad vibrational bands develop between 3600-3100 cm^{-1} and 2700-2300 cm^{-1}, which indicate the formation of ice clusters,[175] most likely due to adsorption of residual H_2O and D_2O.

The formation of D_2O and H_2O ice clusters is also apparent from the subsequently recorded TPD traces (see Fig. 6.3b). Here, D_2O and H_2O desorb in broad desorption features below 200 K, which are typical for physisorbed water.[9] A broad H_2O

desorption feature above 500 K may be attributed to the recombinative desorption of surface OH groups as H_2O. C_3H_4 (40 amu) desorbs in a sharp feature at 113 K, hence at lower temperature than on clean CeO_2(111). This lowered desorption temperature is possibly linked to an interaction of C_3H_4 with surface hydroxyls and ice clusters. A broad desorption feature of the 44 amu trace around ∼300 K is caused by desorption of chemisorbed CO_2, rather than of propene-D_2 ($C_3H_4D_2$, 44 amu), which would be expected to desorb at lower temperature. Since no CO_2 adsorbate vibrations are apparent in the IRAS spectrum (Fig. 6.3a), the adsorption of CO_2 took place most likely during manipulation of the sample from IRAS to TPD position at 90 K.

Considering the IRAS and TPD data, we attribute the lack of hydrogenation reactivity in UHV to the weak interaction of C_3H_4 and CeO_2(111), which results in desorption of C_3H_4 at temperatures too low to activate the hydrogenation reaction.[14, 15]

6.3.2 H_2 and Propyne on CeO_2(111) at Elevated Pressure

To investigate whether hydrogenation of C_3H_4 takes place at more realistic pressures and temperatures, we performed a series of reactivity experiments on CeO_2(111) films using gas chromatography (GC). For these experiments, a "high pressure" cell of the UHV apparatus served as a batch-type reactor. CeO_2(111) thin films were prepared on both sides of the Ru(0001) crystal to maximize the oxide surface area and to minimize catalytic contribution from the Ru substrate. H_2 was provided in large excess ($p(H_2)$:$p(C_3H_4)$=10:0.3 mbar=30:1).[11–13, 108] H_2 and C_3H_4 were mixed in the gas line, immediately expanded into the chamber, balanced with Ar to ∼1 bar, and circulated by a membrane pump to ensure good mixing. The concentration of reactants and products in the gas phase was analyzed by GC.

Qualitative and Quantitative Analysis

Fig. 6.4 shows a typical gas chromatogram obtained during the reactivity tests. Apart from C_3H_4, the chromatogram shows signals of the hydrogenation products C_3H_6 and C_3H_8 at 5.4 min and 4.2 min retention time, respectively. The signal at 7.4 min retention time originates from a non-identified impurity in the propyne gas, which, however, did not engage in reaction. A third compound which formed during the experiment is labeled as compound '3'. Table 6.2 gives an overview of all observed species.

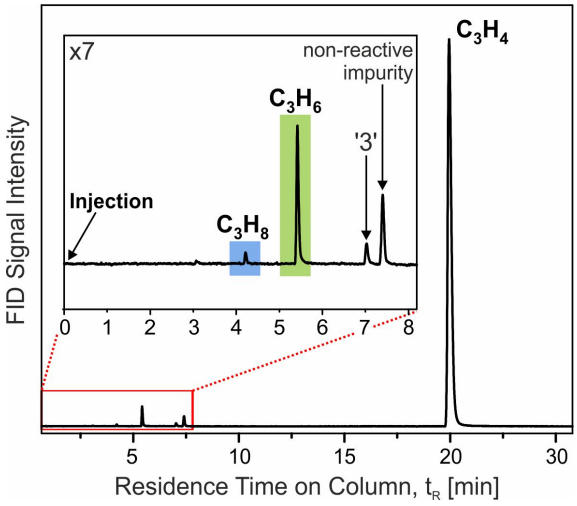

Fig. 6.4: Typical gas chromatogram obtained during the reactivity tests with reactants and reaction products indicated. (FID detector; data shown here: after 275 min hydrogenation time over $CeO_2(111)$, 400 K, initial pressures 10 mbar H_2, 0.33 mbar C_3H_4, balanced to ∼1 bar with Ar.)

t_R [min]	Assignment	Notes
4.2	Propane (C_3H_8)	Full hydrogenation product
5.4	Propene (C_3H_6)	Selective hydrogenation product
7.0	Unidentified compound ('3')	Unidentified product
7.4	Unidentified compound	Impurity (unreactive)
9.7	Propyne (C_3H_4)	

Table 6.2: Retention times t_R of compounds detected during elevated pressure hydrogenation of C_3H_4 (Al_2O_3 "KCl" column at 353 K, split-less injection). C_3H_4, C_3H_6, and C_3H_8 signals have been assigned in pure-compound reference experiments.

We obtain the relative concentration c(i)[%] of an individual hydrocarbon compound i in the reaction gas mixture from the FID detector response by the *Area Percent Method*:[90]

$$c(i)[\%] = \frac{A(i) \times RF(i)}{\sum_{i=1}^{n} A(i) \times RF(i)} \times 100\% \tag{6.4}$$

where $A(i)$ is the integrated peak area for i and $RF(i)$ is the response factor of the detector for compound i:

$$RF(i) = \frac{p(i)}{A(i)} \tag{6.5}$$

RF(i) was measured for C_3H_4, C_3H_6, and C_3H_8 in a series of pure and mixed-compound reference experiments with known pressures $p(i)$. For unidentified compounds, we assume the (intermediate) response factor of propene.

Finally, we calculate C_3H_4 conversion, $X(C_3H_4)$, at any given reaction time t from the individual concentrations:

$$\mathrm{X(C_3H_4)\ [\%]} = \frac{c(\mathrm{C_3H_4})_0 - c(\mathrm{C_3H_4})_t}{c(\mathrm{C_3H_4})_0} \times 100\% \tag{6.6}$$

where $c(C_3H_4)_0$ is the C_3H_4 concentration before reaction and $c(C_3H_4)_t$ is the concentration of C_3H_4 at reaction time t.

Similarly, we obtain the selectivity $S(i)$ for reaction product j as:

$$S(j)[\%] = \frac{c(\mathrm{j})_t - c(\mathrm{j})_0}{c(\mathrm{C_3H_4})_0 - c(\mathrm{C_3H_4})_t} \times 100\% \tag{6.7}$$

Equation 6.7 acts on the assumption that one C_3H_4 molecule reacts (with H_2) to form one product molecule. This is certainly true in the case of the hydrogenation products C_3H_6 and C_3H_8. Please note that for unidentified products, the actual selectivites may be different than the calculated values in case of differing reaction stoichiometries.

Hydrogenation Reactivity on $CeO_2(111)$

Fig. 6.5a shows the kinetics of the C_3H_4 hydrogenation reaction over $CeO_2(111)$ at 300 K. Hydrogenation yields C_3H_6 and C_3H_4, however only in small concentrations. The reaction rate is low from the start of the experiment on and decreases at longer reaction times (t>300 min). After 275 min reaction time, only ∼0.4% C_3H_4 is converted. The reaction proceeded to form C_3H_6 in a selectivity of ∼90% and C_3H_8 in a selectivity of ∼10%.

Fig. 6.5b shows XP spectra of the $CeO_2(111)$ surface before the reaction and after 300 min reaction time. Before the reaction, $CeO_2(111)$ exhibits only Ce^{4+} and O^{2-} species. After the reaction, additional Ce^{3+} and OH features arise in the Ce 3d and O 1s region, respectively. Both are justified by the dissociation of H_2 on the oxide surface.

Since the slow dissociation of H_2 at 300 K (see chapter 4) is expected to contribute crucially to the low reaction rate, we furthermore investigated the hydrogenation

performance of $CeO_2(111)$ at elevated temperatures. Fig. 6.6 summarizes C_3H_4 conversion and product selectivities over $CeO_2(111)$ between 300 K and 600 K, established after 275 min reaction time. Despite the higher temperatures the overall conversion of C_3H_4 remains small. Overall, no more than ∼2% conversion are detected at any reaction temperature. The reaction proceeds in optimal selectivity at 300 K, where ∼90% of the consumed C_3H_4 was hydrogenated to C_3H_6 and ∼10% to C_3H_8. The conversion at this temperature, however, was the lowest observed (X∼0.4%). At higher temperatures, the selectivities for C_3H_6 and C_3H_8 decrease at the expense of a third compound ('3'). The chemical nature of this compound could not be identified, but might be associated with the C_3H_4 isomerization product propadiene, which is suggested to form over O vacancies.[11]

In order to ensure that the observed hydrogenation happens indeed on $CeO_2(111)$, we performed blank experiments under equivalent conditions on two reference systems. One reference was comprised of only the sample holder, which consists of Mo and Ta rods and a chromel-alumel thermocouple. The second reference system was a hand-polished Au(111) crystal, spot-weld onto the sample holder. To exclude influences from the sample heating stage, we perform these reference experiments at 300 K. Fig. 6.7 compares the concentration of products on the different systems after 275 min reaction time. Both reference systems perform similarly to $CeO_2(111)$, the only apparent difference being the additional production of compound '3' on Au(111). Compared to the reference systems, $CeO_2(111)$ does not show any appreciable activity in the hydrogenation reaction.

The low C_3H_4 conversion on $CeO_2(111)$ in comparison to the experiments by Vilé et al.[11] ($X(C_3H_4)$=96% at 523 K) might be attributed to the low surface area of our sample and its low density of surface defects. However, also more recent studies on large surface area CeO_2 *powders* could not reproduce the conversion and selectivity values reported earlier. As such, Cao et al. detected conversion of C_2H_2 in the hydrogenation reaction of only 2% at 573 K.[108] Padole et al. note that "CeO_2 did not show any appreciable activity for the [hydrogenation] reaction in a temperature range of 35-700 °C".[168] The authors assign this lack of reactivity to weak alkyne adsorption on the oxide in the given temperature range. In the authors' comparative studies, doping of CeO_2 powder with Pd^{2+} increased the stability of adsorbed C_2H_2 and resulted in conversion rates of 70% at 343 K.

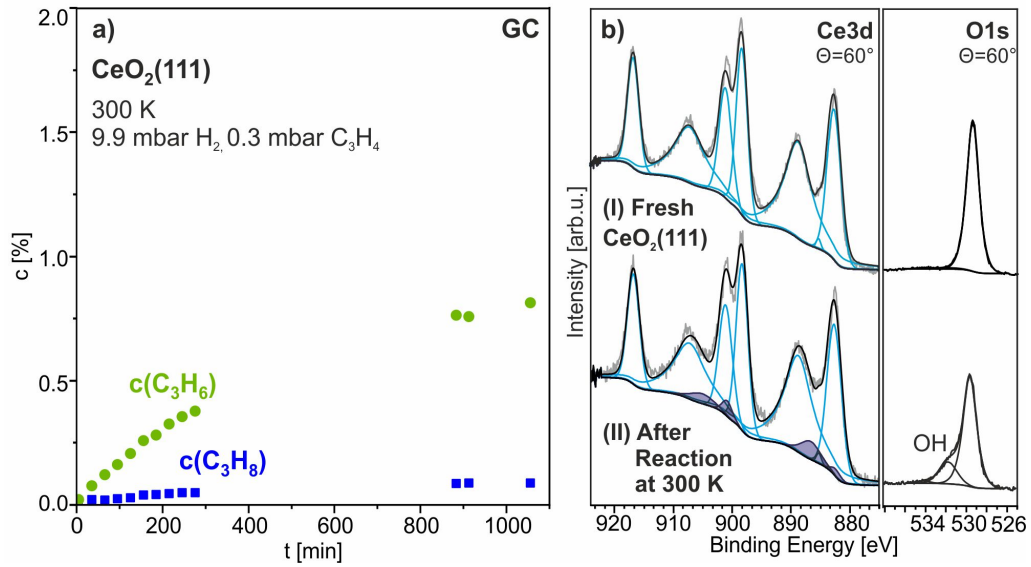

Fig. 6.5: C_3H_4 hydrogenation over stoichiometric $CeO_2(111)$ at 300 K. Left: Reaction time-dependent concentration of products. Right: Ce 3d and O 1s XP spectra of $CeO_2(111)$ before and after 300 min reaction time (grazing emission, 300 K).

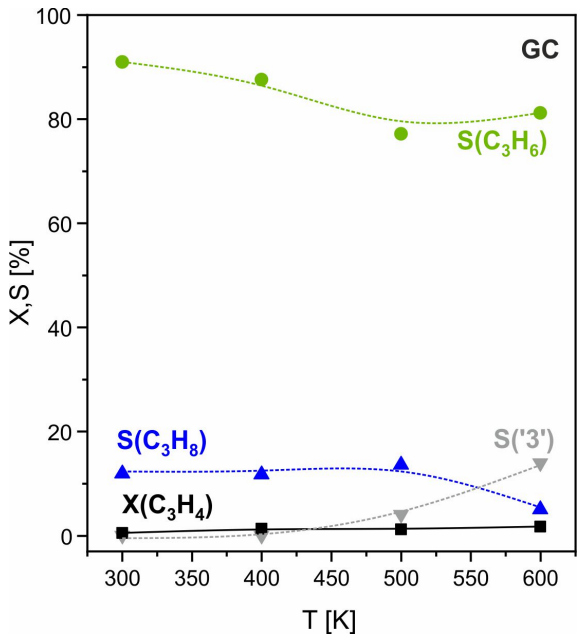

Fig. 6.6: Conversion (X) of C_3H_4 and product selectivities (S) in the hydrogenation reaction over $CeO_2(111)$ as a function of reaction temperature (∼10 mbar H_2, 0.3 mbar C_3H_4, t=275 min). Indicated lines are guides to the eye.

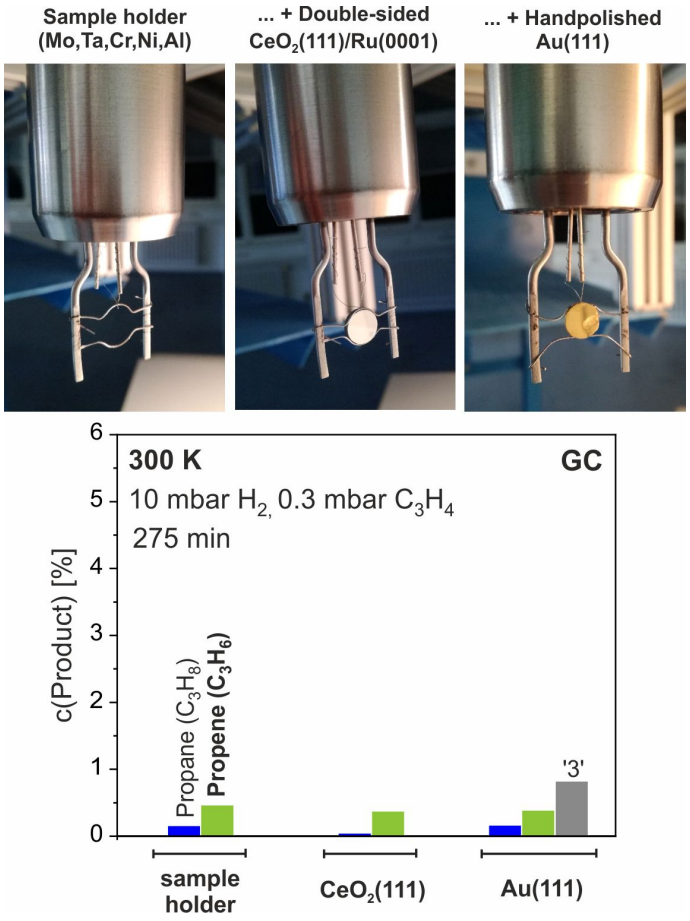

Fig. 6.7: Reference experiments at 300 K (275 min reaction time): Concentration of products after passing 10 mbar H_2 and 0.3 mbar C_3H_4 over sample holder, $CeO_2(111)$/Ru(0001), or hand-polished Au(111).

Hydrogenation Reactivity on Reduced $CeO_{2-x}(111)$

If the low hydrogenation reactivity of $CeO_2(111)$ is indeed caused mainly by its weak interaction with C_3H_4, reduced $CeO_{2-x}(111)$, with more strongly bound C_3H_4 adsorbates (see section 6.2), should show increased hydrogenation activity.

Fig. 6.8a shows the kinetics of the hydrogenation reaction on $CeO_{2-x}(111)$ at 300 K. After 275 min of reaction, only ~0.8% of C_3H_4 are consumed. The conversion of C_3H_4 yields C_3H_6 and C_3H_8 as hydrogenation products with selectivities of 64% and 14%, respectively. Compound '3' (S('3')=22%) is formed in the earliest stage of the reaction and stays unchanged in concentration thereafter. Interestingly, the hydrogenation rate on reduced $CeO_{2-x}(111)$, as opposed to $CeO_2(111)$, stays constant up to very long reaction times (t=1000 min).

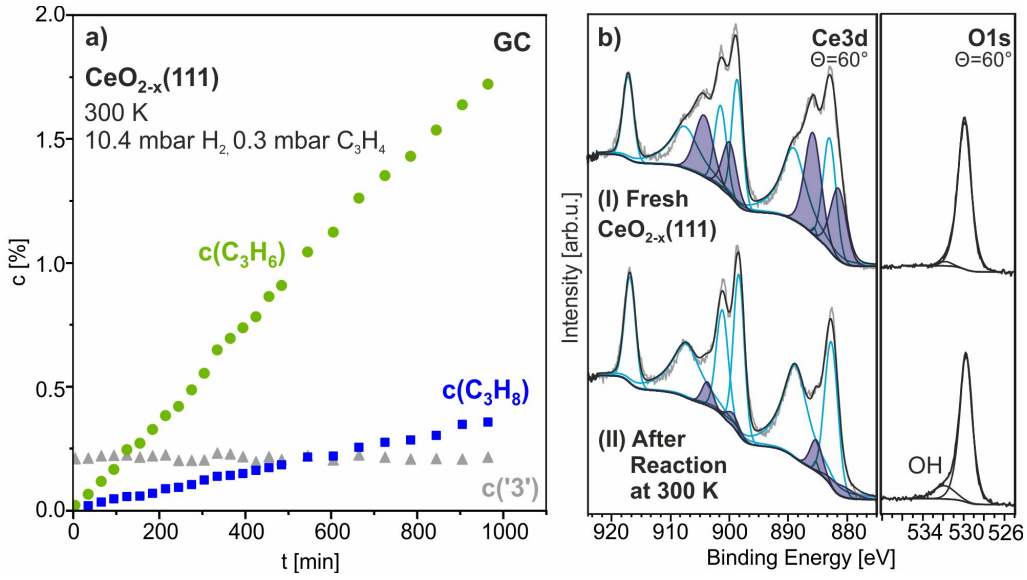

Fig. 6.8: C_3H_4 hydrogenation reaction over reduced $CeO_{2-x}(111)$ at 300 K. Left: Reaction time-dependent concentration of products in gas feed. Right: Ce 3d and O 1s XP spectra (60° emission) of $CeO_{2-x}(111)$ before and after 300 min reaction time.

In comparison to the selectivity values obtained on $CeO_2(111)$ ($S(C_3H_6)$=90%, $S(C_3H_6)$=10%), the presence of O vacancies seems to compromise the selectivity of the hydrogenation reaction in benefit of compound '3'. The chemical nature of this compound, as well as the reason for its vanishing production rate after initial formation, may be elucidated only by further investigations.

Fig. 6.8b shows XP spectra of reduced $CeO_{2-x}(111)$ before the reaction and after 300 min reaction time. Before the reaction, $CeO_{2-x}(111)$ shows a high intensity of Ce^{3+} features in the Ce 3d region, alongside features of Ce^{4+}. In the O 1s region, no hydroxyl feature is apparent. After 300 min of hydrogenation reaction, the O 1s main peak shows a high BE tail, indicating the presence of hydroxyl groups. Furthermore, the Ce 3d region shows a striking decrease of Ce^{3+} intensity. Thus, while $CeO_{2-x}(111)$ is hydroxylated during the reaction, it is also re-oxidized. This re-oxidation happens in the same manner as observed in D_2 exposure experiments in chapter 4, and is therefore attributed to the formation of hydride species.

While, at this point, we can only speculate about the increased reaction rate at long reaction times on reduced $CeO_{2-x}(111)$ as compared to $CeO_2(111)$, two factors may contribute to this. First of all, the increased stability of C_3H_4 adsorbates at

O vacancies may largely benefit the interaction of C_3H_4 with adsorbed H species at ambient temperatures. Secondly, the presence of hydride species may benefit the reaction. If hydrides are present on the CeO_{2-x}(111) *surface*, their direct participation in the hydrogenation via a concerted mechanism[15] (simultaneous transfer of H^+ and H^- to π-bound C_3H_4) is imaginable. Since hydrides are expected to be thermodynamically less stable in O vacancies on the surface than in the bulk,[144] such a contribution would only be plausible in case of kinetic limitations, e.g. by slow diffusion processes. As the DFT+U results of chapter 4 show, hydrides below the CeO_{2-x}(111) surface are stable, but may transform into surface hydroxyl groups, which could in turn be a valuable source of H for the hydrogenation reaction.[144]

6.4 Conclusions

C_3H_4 adsorbs weakly on the stoichiometric CeO_2(111) surface, most likely as a molecular π-complex. On reduced CeO_{2-x}(111), C_3H_4 is considerably stronger bound, possibly due to a direct interaction with O vacancies.

C_3H_4 barely interacts with hydroxylated CeO_2(111). In UHV at low temperature, no considerable interaction could be detected. Upon heating, C_3H_4 desorbs from the surface at temperatures too low to activate hydrogenation. Even when higher pressures of H_2 and temperatures of up to 600 K are applied, CeO_2(111) shows only minor activity in the hydrogenation of C_3H_4. The (very slow) hydrogenation reaction proceeded in highest selectivity ($S(C_3H_6)$= 90%) at 300 K. Selectivity for C_3H_6 decreased with increasing temperature, in benefit of the fully hydrogenated product C_3H_8 and another, yet unidentified product. The low hydrogenation activity suggests that CeO_2(111) is largely inactive in the hydrogenation reaction. The origin of previously reported high values of activity[11–14] is unclear, but may possibly be associated with a very high density of defects on the employed CeO_2 powders.

The presence of O vacancies on CeO_{2-x}(111) had little influence on the overall low C_3H_4 conversion. However, the hydrogenation rate is sustained on CeO_{2-x}(111) even at long reaction times, while it decreases on the stoichiometric CeO_2(111) surface. Reasons for the sustained reaction rate on CeO_{2-x}(111) as opposed to CeO_2(111) could be the stronger binding to C_3H_4 adsorbates and the presence of hydrides within the oxide. Whether these hydride species may contribute to the reactions on the oxide surface is an interesting research question, which to be answered will require further theoretical and experimental investigation.

7 Summary

CeO_2 is a catalytically active oxide that is unique in its redox properties and flexible stoichiometry. The ability of CeO_2 to easily release O atoms from its lattice without changing its lattice arrangement makes the oxide an outstanding supporting material in various catalytic reactions. The presence of O vacancies on the CeO_2 surface thereby considerably influences the oxide's reactivity. To gain new insights into the role of O vacancies in the surface chemistry of CeO_2, this thesis has explored the oxide's interaction with H_2, CO_2, and C_3H_4, and its activity in the selective hydrogenation reaction.

We have studied the influence of O vacancies on the surface chemistry of ceria by comparative experiments on stoichiometric $CeO_2(111)$ and reduced $CeO_{2-x}(111)$ thin films. $CeO_2(111)$ was prepared by epitaxial growth onto a Ru(0001) single crystal. Annealing of this thin film in UHV at high temperature yields reduced $CeO_{2-x}(111)$. These $CeO_{2-x}(111)$ thin films, as shown by XPS and LEED, are partially reduced, i.e. exhibit both Ce^{3+} and Ce^{4+} ions. The concentration of Ce^{3+} ions is highest close to the surface, with a gradient towards the more oxidized bulk. Likewise, O vacancies are present in highest density on the $CeO_{2-x}(111)$ surface, where they order into a periodic array with $(\sqrt{7} \times \sqrt{7})$ periodicity.

In the first part of this thesis, we have explored the interaction of atomic hydrogen with $CeO_2(111)$ by IRAS, XPS, and TPD. Adsorption of atomic H results in the formation of hydroxyl groups and the reduction of Ce^{4+} to Ce^{3+} ions. Surface hydroxyl groups on $CeO_2(111)$ are coordinated to three underlying Ce species (Ce^{3+} or Ce^{4+}). By IRAS and complementary DFT+U studies, we identify three types of hydroxyl groups, which coordinate to either one, two, or three Ce^{3+} species. With increasing degree of surface reduction, OH groups are stabilized on $CeO_2(111)$. At elevated temperature, hydroxyl groups recombine and desorb as water, leaving behind surface O vacancies.

We furthermore investigated the dissociation of H_2 on $CeO_2(111)$ by IRAS, XPS, TPD, and NRA experiments, and interpreted the experimental results on the basis of complementary DFT+U studies. Dissociation of H_2 on the oxide surface does not occur under UHV conditions. At elevated pressure (10 mbar), however, H_2 dissociates on $CeO_2(111)$ above 300 K to form surface hydroxyls. The amount of formed

hydroxyls increases with the sample temperature up to 500 K. At 500 K and higher temperature, hydroxyls desorb as water.
If O vacancies are present within the oxide, exposure to molecular hydrogen at room temperature leads to the formation of hydride species below the surface. This process is accompanied by a re-oxidation of the oxide, due to an electron transfer from Ce^{3+} to H species. Hydride species within CeO_{2-x} are stable, but may transform into surface hydroxyls upon heating. With increasing exposure temperature, less hydride species are incorporated into CeO_{2-x}. At 500 K, the interaction of $CeO_{2-x}(111)$ with molecular hydrogen is dominated by the formation of surface hydroxyls.

In the second part of this thesis, we have investigated the adsorption of CO_2 on $CeO_2(111)$. IRAS measurements and complementary DFT+U studies indicate that CO_2 chemisorbs on the oxide surface, most likely as a carbonate species. We have followed the thermal stability of this species with TP-IRAS and TPD, finding that chemisorbed CO_2 is stable on $CeO_2(111)$ up to 270 K. The presence of O vacancies does not alter the chemical state of CO_2 adsorbates, but increases their stability.

Finally, we investigated the interaction of $CeO_2(111)$ with C_3H_4 and the reactivity of the oxide surface in the selective hydrogenation reaction. IRAS and TPD experiments show that C_3H_4 adsorbs weakly on stoichiometric $CeO_2(111)$, most likely as a molecular π-complex, which desorbs at 140 K. When O vacancies are present, a small amount of C_3H_4 becomes substantially stronger bound.
The adsorption of C_3H_4 on hydroxylated $CeO_2(111)$ is weak and no apparent interaction between C_3H_4 and hydroxyl groups is apparent in UHV. In order to investigate the hydrogenation of C_3H_4 over $CeO_2(111)$, we thus performed GC reactivity experiments at elevated H_2 and C_3H_4 pressure. The reported outstanding activity of CeO_2 powders in the hydrogenation reaction could not be reproduced in our experiments, which might be related to the small area and/or the low defect density of the $CeO_2(111)$ thin film. Interestingly, the hydrogenation rate on $CeO_2(111)$ decreases at long reaction times, while it is sustained on reduced $CeO_{2-x}(111)$. This effect may be linked to the higher stability of adsorbed C_3H_4 close to O vacancies, or to the presence of hydrides in CeO_{2-x} under hydrogenation reaction conditions.

Ultimately, we show that O vacancies play an essential role in the surface chemistry of $CeO_2(111)$. Oxygen vacancies stabilize adsorbates, such as hydroxyl groups, CO_2, and C_3H_4. In the interaction of H_2 with $CeO_2(111)$, O vacancies enable the formation of hydrides below the surface, which results in an unusual re-oxidation of the oxide.

Appendix

List of Abbreviations

AFM	Atomic Force Microscopy
BE	Binding Energy
δ	Deformation Vibration
DFT	Density Functional Theory
FCC	Face-Centered Cubic
FID	Flame Ionization Detector
FTIR	Fourier Transform Infrared Spectroscopy
FWHM	Full Width Half Maximum
GC	Gas Chromatography
H-NRA	$^{1}\mathrm{H}(^{15}\mathrm{N},\alpha\gamma)^{12}\mathrm{C}$-NRA
HSA	Hemispherical Analyzer
IR	Infrared
IRAS	Infrared Reflection Absorption Spectroscopy
LEED	Low Energy Electron Diffraction
LEEM	Low Energy Electron Microscopy
ML	Monolayer
NRA	Nuclear Reaction Analysis
NP	Nanoparticle(s)
ν	Stretching Vibration
PID	Proportional Integral Derivative
PM	Polarization Modulation
ppb	Parts Per Billion
ppm	Parts Per Million
QMS	Quadrupole Mass Spectrometer
STM	Scanning Tunneling Microscopy
TEM	Transmission Electron Microscopy
TP-	Temperature-Programmed
TPD	Temperature-Programmed Desorption
TPR	Temperature-Programmed Reduction
UHV	Ultrahigh Vacuum
XPS	X-Ray Photoelectron Spectroscopy

Ce 3d XPS Fitting Parameters and Constraints

A deconvolution of Ce 3d XP spectra into individual peaks can only be meaningful if physically meaningful parameters are chosen. For this, the Ce 3d spectra included in this thesis have been analyzed using fitting parameters which are established within the scientific community.[25, 95–97, 100] Table 7.1 summarizes typical peak positions, peak widths, and constraints that have been implied in the fitting process. In brief, Ce 3d spectra were background-corrected by subtraction of a Shirley background.[86] All Ce 3d spectra were fitted as a linear combination of Ce^{4+} and Ce^{3+} peak envelopes. Peaks were fitted with Voigt-type functions. The doublet pairs were fitted in a peak area ratio of 3:2. FWHM in the spin-orbit split pairs were set to similar values. The BE difference between spin-orbit split doublet peaks was set to 18.45 eV. The intensity ratio and relative positions of Ce^{4+} features were determined from a stoichiometric $CeO_2(111)$ thin film, yielding a Ce^{4+} envelope function. An additional peak was incorporated to account for the asymmetry of peak V, as it has been suggested in previous studies.[100] A Ce^{3+} envelope was obtained from a highly reduced $CeO_{2-x}(111)$ sample after subtraction of Ce^{4+} features.
Even though precautions were taken in terms of physically meaningful constraints, deconvolution of Ce 3d spectra can be only approximate due to the high level of complexity with up to 10 overlapping peaks and due to the use of a Shirley background, which is not explicitly suited for the large Ce 3d binding energy interval.[17]

Error Analysis for XPS Quantification

To account for uncertainties in the fitting procedure, we have performed an analysis for standard errors. At least three deconvolution attempts were made per spectrum. For each attempt, the BE window was altered (in the limits of physically meaningful data evaluation), yielding slightly different background subtraction. Peak fitting was optimized using the predefined peak constraints, as they are described above.
For the calculated peak areas and related values, the standard error of the mean, σ_x^- , was estimated as:

$$\sigma_x^- = \frac{s}{\sqrt{N}} \tag{7.1}$$

where N is the size of the sample and s is the sample standard deviation:

$$s = \sqrt{\frac{1}{N-1}\sum_{i=1}^{N}(x_i - \bar{x})^2} \tag{7.2}$$

with x_i being the observed value derived from an individual fitting procedure and $\bar{x}$ the mean of the observed values of all fitting procedures. Please note that systematic errors, such as the inadequate subtraction of a Shirley background for Ce 3d spectra, a possible non-linearity of the intensity ratios of different final states, or instrument errors, are not yet accounted for in this estimation.

Label[95]	State	BE [eV]	Position	Area A	FWHM [eV]
U”’	$3d_{3/2}$	916.7			∼2
U”	$3d_{3/2}$	907.1			∼6
U’	$3d_{3/2}$	904.1			∼3
U	$3d_{3/2}$	901.0			∼2
U_0	$3d_{3/2}$	899.8			∼2
V”’	$3d_{5/2}$	898.2	BE(U”’)-18.45	1.5×A(U”’)	∼2
V”	$3d_{5/2}$	888.7	BE(U”)-18.45	1.5×A(U”)	∼5
V’	$3d_{5/2}$	885.6	BE(U’)-18.45	1.5×A(U’)	∼3
Asym. of V		885.2	BE(U)-15.8	0.02×A(U)	∼1
V	$3d_{5/2}$	882.6	BE(U)-18.45	1.5×A(U)	∼3
V_0	$3d_{5/2}$	881.4	BE U_0)-18.45	1.5×A(U_0)	∼2

Table 7.1: Ce 3d fitting parameters and constraints for Ce^{4+} and Ce^{3+} features (highlighted) in order of decreasing BE. Peak positions for Ce^{4+} features are given for CeO_2 and might slightly differ for CeO_{2-x} (see section 2.6.2).

Bibliography

[1] J. Hagen, *Industrial Catalysis: A Practical Approach*, 3rd ed., Wiley-VCH, **2015**.

[2] G. Ertl, H. Knözinger, F. Schüth, J. Weitkamp, *Handbook of Heterogeneous Catalysis*, 3rd ed., Wiley-VCH, **2008**.

[3] B. E. Smith, *Science* **2002**, *297*, 1654–1655.

[4] J. Zhao, Y. Yuan, X. Meng, L. Duan, R. Zhou, *Materials* **2018**, *12*, 46.

[5] S. Schauermann, K.-H. Dostert, C. O. Brien, H. J. Freund, *ECOSS* **2017**.

[6] A. Trovarelli, *Catalysis by Ceria and Related Materials*, *Vol. 2*, World Scientific, **2002**.

[7] R. J. Gorte, *AlChE J.* **2010**, *56*, 1126–1135.

[8] L. Vivier, D. Duprez, *ChemSusChem* **2010**, *3*, 654–678.

[9] D. R. Mullins, *Surf. Sci. Rep.* **2015**, *70*, 42–85.

[10] T. Montini, M. Melchionna, M. Monai, P. Fornasiero, *Chem. Rev.* **2016**, *116*, 5987–6041.

[11] G. Vilé, B. Bridier, J. Wichert, J. Pérez-Ramírez, *Angew. Chem. Int. Ed.* **2012**, *51*, 8620–8623.

[12] G. Vilé, S. Colussi, F. Krumeich, A. Trovarelli, J. Pérez-Ramírez, *Angew. Chem. Int. Ed.* **2014**, *53*, 12069–12072.

[13] G. Vilé, S. Wrabetz, L. Floryan, M. E. Schuster, F. Girgsdies, D. Teschner, J. Pérez-Ramírez, *ChemCatChem* **2014**, *6*, 1928–1934.

[14] J. Carrasco, G. Vilé, D. Fernández-Torre, R. Pérez, J. Pérez-Ramírez, M. V. Ganduglia-Pirovano, *J. Phys. Chem. C* **2014**, *118*, 5352–5360.

[15] M. García-Melchor, L. Bellarosa, N. López, *ACS Catal.* **2014**, *4*, 4015–4020.

[16] M. V. Ganduglia-Pirovano, *Catal. Today* **2015**, *253*, 20–32.

[17] F. P. Netzer, A. Fortunelli, *Oxide Materials at the Two-Dimensional Limit*, 1st ed., Springer International Publishing, **2016**.

[18] H.-Y. Li, H.-F. Wang, X.-Q. Gong, Y.-L. Guo, Y. Guo, G. Lu, P. Hu, *Phys. Rev. B* **2009**, *79*, 193401.

[19] J.-F. Jerratsch, X. Shao, N. Nilius, H.-J. Freund, C. Popa, M. V. Ganduglia-Pirovano, A. M. Burow, J. Sauer, *Phys. Rev. Lett.* **2011**, *106*, 246801.

[20] G. E. Murgida, V. Ferrari, M. V. Ganduglia-Pirovano, A. M. Llois, *Phys. Rev. B* **2014**, *90*, 115120.

[21] J. E. Sutton, A. Beste, S. H. Overbury, *Phys. Rev. B* **2015**, *92*, 144105.

[22] G. E. Murgida, V. Ferrari, A. M. Llois, M. V. Ganduglia-Pirovano, *Phys. Rev. Mat.* **2018**, *2*, 083609.

[23] R. Olbrich, G. E. Murgida, V. Ferrari, C. Barth, A. M. Llois, M. Reichling, M. V. Ganduglia-Pirovano, *J. Phys. Chem. C* **2017**, *121*, 6844–6851.

[24] M. Nolan, S. C. Parker, G. W. Watson, *Surf. Sci.* **2005**, *595*, 223–232.

[25] A. Pfau, K. D. Schierbaum, *Surf. Sci.* **1994**, *321*, 71–80.

[26] G. D. Wang, D. D. Kong, Y. H. Pan, H. B. Pan, J. F. Zhu, *Appl. Surf. Sci.* **2012**, *258*, 2057–2061.

[27] J. Xu, S. H. Overbury, *J. Catal.* **2004**, *222*, 167–173.

[28] W. Xiao, Q. Guo, E. G. Wang, *Chem. Phys. Lett.* **2003**, *368*, 527–531.

[29] U. Berner, K.-D. Schierbaum, *Phys. Rev. B* **2002**, *65*, 235404.

[30] H. Wilkens, O. Schuckmann, R. Oelke, S. Gevers, A. Schaefer, M. Bäumer, M. H. Zoellner, T. Schroeder, J. Wollschläger, *Appl. Phys. Lett.* **2013**, *102*, 111602.

[31] J. Höcker, J.-O. Krisponeit, T. Schmidt, J. Falta, J. I. Flege, *Nanoscale* **2017**, *9*, 9352–9358.

[32] E. Vescovo, C. Carbone, *Phys. Rev. B* **1996**, *53*, 4142–4147.

[33] T. Duchoň, F. Dvořák, M. Aulická, V. Stetsovych, M. Vorokhta, D. Mazur, K. Veltruská, T. Skála, J. Mysliveček, I. Matolínová, V. Matolín, *J. Phys. Chem. C* **2014**, *118*, 357–365.

[34] T. Duchoň, F. Dvořák, M. Aulická, V. Stetsovych, M. Vorokhta, D. Mazur, K. Veltruská, T. Skála, J. Mysliveček, I. Matolínová, V. Matolín, *J. Phys. Chem. C* **2014**, *118*, 5058–5059.

[35] D. R. Mullins, P. V. Radulovic, S. H. Overbury, *Surf. Sci.* **1999**, *429*, 186–198.

[36] E. L. Wilson, Q. Chen, W. A. Brown, G. Thornton, *J. Phys. Chem. C* **2007**, *111*, 14215–14222.

[37] T. X. T. Sayle, S. C. Parker, C. R. A. Catlow, *J. Chem. Soc. Chem. Commun.* **1992**, 977–978.

[38] J. Paier, C. Penschke, J. Sauer, *Chem. Rev.* **2013**, *113*, 3949–3985.

[39] Z. Wu, Y. Cheng, F. Tao, L. Daemen, G. S. Foo, L. Nguyen, X. Zhang, A. Beste, A. J. Ramirez-Cuesta, *J. Am. Chem. Soc.* **2017**, *139*, 9721–9727.

[40] N. V. Skorodumova, S. I. Simak, B. I. Lundqvist, I. A. Abrikosov, B. Johansson, *Phys. Rev. Lett.* **2002**, *89*, 166601.

[41] F. Esch, S. Fabris, L. Zhou, T. Montini, C. Africh, P. Fornasiero, G. Comelli, R. Rosei, *Science* **2005**, *309*, 752.

[42] Y. Pan, N. Nilius, H.-J. Freund, J. Paier, C. Penschke, J. Sauer, *Phys. Rev. Lett.* **2013**, *111*, 206101.

[43] Z.-K. Han, Y.-Z. Yang, B. Zhu, M. V. Ganduglia-Pirovano, Y. Gao, *Phys. Rev. Mat.* **2018**, *2*, 035802.

[44] M. V. Ganduglia-Pirovano, J. L. F. Da Silva, J. Sauer, *Phys. Rev. Lett.* **2009**, *102*, 026101.

[45] H.-Y. Li, H.-F. Wang, X.-Q. Gong, Y.-L. Guo, Y. Guo, G. Lu, P. Hu, *Phys. Rev. B* **2009**, *79*, 193401.

[46] J.-F. Jerratsch, X. Shao, N. Nilius, H.-J. Freund, C. Popa, M. V. Ganduglia-Pirovano, A. M. Burow, J. Sauer, *Phys. Rev. Lett.* **2011**, *106*, 21879–21885.

[47] S. Torbrügge, M. Reichling, A. Ishiyama, S. Morita, s. Custance, *Phys. Rev. Lett.* **2007**, *99*, 056101.

[48] B. W. Sheldon, V. B. Shenoy, *Phys. Rev. Lett.* **2011**, *106*, 216104.

[49] H. Nörenberg, G. A. D. Briggs, *Phys. Rev. Lett.* **1997**, *79*, 4222–4225.

[50] Y. Namai, K.-I. Fukui, Y. Iwasawa, *Catal. Today* **2003**, *85*, 79–91.

[51] D. C. Grinter, R. Ithnin, C. L. Pang, G. Thornton, *J. Phys. Chem. C* **2010**, *114*, 17036–17041.

[52] S. M. F. Shahed, T. Hasegawa, Y. Sainoo, Y. Watanabe, N. Isomura, A. Beniya, H. Hirata, T. Komeda, *Surf. Sci.* **2014**, *628*, 30–35.

[53] D. C. Grinter, C. Muryn, A. Sala, C.-M. Yim, C. L. Pang, T. O. Menteş, A. Locatelli, G. Thornton, *J. Phys. Chem. C* **2016**, *120*, 11037–11044.

[54] S. Eck, C. Castellarin-Cudia, S. Surnev, M. G. Ramsey, F. P. Netzer, *Surf. Sci.* **2002**, *520*, 173–185.

[55] J. I. Flege, B. Kaemena, S. Gevers, F. Bertram, T. Wilkens, D. Bruns, J. Bätjer, T. Schmidt, J. Wollschläger, J. Falta, *Phys. Rev. B* **2011**, *84*, 235418.

[56] V. Stetsovych, F. Pagliuca, F. Dvořák, T. Duchoň, M. Vorokhta, M. Aulická, J. Lachnitt, S. Schernich, I. Matolínová, K. Veltruská, T. Skála, D. Mazur, J. Mysliveček, J. Libuda, V. Matolín, *J. Phys. Chem. Lett.* **2013**, *4*, 866–871.

[57] K. Oura, V. G. Lifshits, A. A. Saranin, A. V. Zotov, M. Katayama, *Surface Science. An Introduction*, Springer, **2003**.

[58] F. M. Hoffmann, *Surf. Sci. Rep.* **1983**, *3*, 107–192.

[59] P. R. Griffiths, J. A. de Haseth, *Fourier Transform Infrared Spectrometry*, John Wiley and Sons, **2006**.

[60] J. M. Chalmers, P. Griffiths, *Handbook of Vibrational Spectroscopy*, John Wiley and Sons, **2006**.

[61] D. J. Tannor, *Introduction to Quantum Mechanics: A Time-Dependent Perspective*, University Science Books, **2006**.

[62] P. Atkins, R. Friedman, *Molecular Quantum Mechanics*, 5th ed., Oxford University Press, **2010**.

[63] R. G. Greenler, *J. Chem. Phys.* **1966**, *44*, 310–315.

[64] T. E. Madey, J. T. Yates, *Vibrational Spectroscopy of Molecules on Surfaces*, Springer, **1987**.

[65] M. Happel, PhD Thesis, **2012**.

[66] S. Schernich, PhD Thesis, **2014**.

[67] G. Pacchioni, G. Cogliandro, P. S. Bagus, *Surf. Sci.* **1991**, *255*, 344–354.

[68] G. D. Mahan, A. A. Lucas, **1978**, *68*, 1344–1348.

[69] P. Hollins, J. Pritchard, *Prog. Surf. Sci.* **1985**, *19*, 275–349.

[70] G. Blyholder, *J. Phys. Chem.* **1964**, *68*, 2772–2777.

[71] N. P. Lebedeva, A. Rodes, J. M. Feliu, M. T. M. Koper, R. A. van Santen, *J. Phys. Chem. B* **2002**, *106*, 9863–9872.

[72] C. Lemire, R. Meyer, S. K. Shaikhutdinov, H. J. Freund, *Surf. Sci.* **2004**, *552*, 27–34.

[73] P. St. Petkov, G. N. Vayssilov, J. Liu, O. Shekhah, Y. Wang, C. Wöll, T. Heine, *ChemPhysChem* **2012**, *13*, 2025–2029.

[74] N. M. Martin, M. Van den Bossche, H. Grönbeck, C. Hakanoglu, F. Zhang, T. Li, J. Gustafson, J. F. Weaver, E. Lundgren, *J. Phys. Chem. C* **2014**, *118*, 1118–1128.

[75] G. Orlandi, W. Siebrand, *J. Chem. Phys.* **1973**, *58*, 4513–4523.

[76] A. Einstein, *Annalen der Physik* **1905**, *322*, 132–148.

[77] F. Müller, Habilitation Thesis, **2014**.

[78] T. L. Barr, *Modern ESCA. The Principles and Practice of X-Ray Photoelectron Spectroscopy*, CRC Press, **1994**.

[79] M. P. Seah in *Surface Analysis by Auger and X-Ray Photoelectron Spectroscopy*, IM Publications, Surface Spectra Limited, **2003**.

[80] L. Zommer, *Vacuum* **1995**, *46*, 617–620.

[81] M. P. Seah, W. A. Dench, *Surf. Interface Anal.* **1979**, *1*, 2–11.

[82] G. A. Somorjai, *Chemistry in Two Dimensions: Surfaces*, Cornell University Press, **1981**.

[83] D. Briggs, J. T. Grant, *Surface Analysis by Auger and X-Ray Photoelectron Spectroscopy*, IM Publications, SurfaceSpectraLimited, **2003**.

[84] D. P. Woodruff, *Modern Techniques of Surface Science*, 3rd ed., Cambridge University Press, **2016**.

[85] B. H. Armstrong, *J. Quant. Spectrosc. Radiat. Transfer* **1967**, *7*, 61–88.

[86] D. A. Shirley, *Phys. Rev. B* **1972**, *5*, 4709–4714.

[87] P. A. Redhead, *Vacuum* **1962**, *12*, 203–211.

[88] E. Habenschaden, J. Küppers, *Surf. Sci.* **1984**, *138*, L147–L150.

[89] D. A. King, *Surf. Sci.* **1975**, *47*, 384–402.

[90] K. Dettmer-Wilde, W. Engewald, *Practical Gas Chromatography. A Comprehensive Reference*, Springer, **2014**.

[91] M. Wilde, K. Fukutani, *Surf. Sci. Rep.* **2014**, *69*, 196–295.

[92] K. Fukutani, M. Wilde, S. Ogura, *Chem. Rec.* **2017**, *17*, 233–249.

[93] J. L. Lu, H. J. Gao, S. Shaikhutdinov, H. J. Freund, *Surf. Sci.* **2006**, *600*, 5004–5010.

[94] M. Baron, O. Bondarchuk, D. Stacchiola, S. Shaikhutdinov, H. J. Freund, *J. Phys. Chem. C* **2009**, *113*, 6042–6049.

[95] P. Burroughs, A. Hamnett, A. F. Orchard, G. Thornton, *J. Chem. Soc. Dalton Trans.* **1976**, 1686–1698.

[96] E. Paparazzo, G. M. Ingo, N. Zacchetti, *J. Vac. Sci. Technol. A* **1991**, *9*, 1416–1420.

[97] D. R. Mullins, S. H. Overbury, D. R. Huntley, *Surf. Sci.* **1998**, *409*, 307–319.

[98] M. A. Henderson, C. L. Perkins, M. H. Engelhard, S. Thevuthasan, C. H. F. Peden, *Surf. Sci.* **2003**, *526*, 1–18.

[99] B. Chen, Y. Ma, L. Ding, L. Xu, Z. Wu, Q. Yuan, W. Huang, *J. Phys. Chem. C* **2013**, *117*, 5800–5810.

[100] Y. Lykhach, S. M. Kozlov, T. Skála, A. Tovt, V. Stetsovych, N. Tsud, F. Dvořák, V. Johánek, A. Neitzel, J. Mysliveček, S. Fabris, V. Matolín, K. M. Neyman, J. Libuda, *Nat. Mat.* **2015**, *15*, 284–289.

[101] A. Kotani, T. Jo, J. C. Parlebas, *Adv. Phys.* **1988**, *37*, 37–85.

[102] O. Gunnarsson, K. Schönhammer, *Phys. Rev. B* **1983**, *28*, 4315–4341.

[103] C. J. Nelin, P. S. Bagus, E. S. Ilton, S. A. Chambers, H. Kuhlenbeck, H. J. Freund, *Int. J. Quantum Chem* **2010**, *110*, 2752–2764.

[104] P. Ernesto, *J. Phys. Cond. Matter* **2018**, *30*, 343003.

[105] S. Sun, D. Mao, J. Yu, Z. Yang, G. Lu, Z. Ma, *Cat. Sci. Technol.* **2015**, *5*, 3166–3181.

[106] A. B. Dongil, B. Bachiller-Baeza, E. Castillejos, N. Escalona, A. Guerrero-Ruiz, I. Rodríguez-Ramos, *Catal. Today* **2018**, *301*, 141–146.

[107] A. Laachir, V. Perrichon, A. Badri, J. Lamotte, E. Catherine, J. C. Lavalley, J. El Fallah, L. Hilaire, F. Le Normand, E. Quemere, G. N. Sauvion, O. Touret, *J. Chem. Soc. Faraday Trans.* **1991**, *87*, 1601–1609.

[108] T. Cao, R. You, X. Zhang, S. Chen, D. Li, Z. Zhang, W. Huang, *PCCP* **2018**, *20*, 9659–9670.

[109] S. H. Overbury, D. R. Huntley, D. R. Mullins, K. S. Ailey, P. V. Radulovic, *J. Vac. Sci. Technol. A* **1997**, *15*, 1647–1652.

[110] Y. Lykhach, V. Johánek, H. A. Aleksandrov, S. M. Kozlov, M. Happel, T. Skála, P. S. Petkov, N. Tsud, G. N. Vayssilov, K. C. Prince, K. M. Neyman, V. Matolín, J. Libuda, *J. Phys. Chem. C* **2012**, *116*, 12103–12113.

[111] V. Matolín, I. Matolínová, F. Dvořák, V. Johánek, J. Mysliveček, K. C. Prince, T. Skála, O. Stetsovych, N. Tsud, M. Václavů, B. Šmíd, *Catal. Today* **2012**, *181*, 124–132.

[112] L. Kundakovic, D. R. Mullins, S. H. Overbury, *Surf. Sci.* **2000**, *457*, 51–62.

[113] M. Fronzi, S. Piccinin, B. Delley, E. Traversa, C. Stampfl, *PCCP* **2009**, *11*, 9188–9199.

[114] Z. Yang, Q. Wang, S. Wei, D. Ma, Q. Sun, *J. Phys. Chem. C* **2010**, *114*, 14891–14899.

[115] D. R. Mullins, P. M. Albrecht, T.-L. Chen, F. C. Calaza, M. D. Biegalski, H. M. Christen, S. H. Overbury, *J. Phys. Chem. C* **2012**, *116*, 19419–19428.

[116] M. Molinari, S. C. Parker, D. C. Sayle, M. S. Islam, *J. Phys. Chem. C* **2012**, *116*, 7073–7082.

[117] X. P. Wu, X. Q. Gong, G. Lu, *PCCP* **2015**, *17*, 3544–9.

[118] Y. Gao, R. Li, S. Chen, L. Luo, T. Cao, W. Huang, *PCCP* **2015**, *17*, 31862–31871.

[119] F. Dvořák, L. Szabová, V. Johánek, M. Farnesi Camellone, V. Stetsovych, M. Vorokhta, A. Tovt, T. Skála, I. Matolínová, Y. Tateyama, J. Mysliveček, S. Fabris, V. Matolín, *ACS Catal.* **2018**, *8*, 4354–4363.

[120] G. Vicario, G. Balducci, S. Fabris, S. de Gironcoli, S. Baroni, *J. Phys. Chem. B* **2006**, *110*, 19380–19385.

[121] M. K. Alam, F. Ahmed, R. Miura, A. Suzuki, H. Tsuboi, N. Hatakeyama, A. Endou, H. Takaba, M. Kubo, A. Miyamoto, *Appl. Surf. Sci.* **2010**, *257*, 1383–1389.

[122] M. K. Alam, F. Ahmed, R. Miura, A. Suzuki, H. Tsuboi, N. Hatakeyama, A. Endou, H. Takaba, M. Kubo, A. Miyamoto, *Catal. Today* **2011**, *164*, 9–15.

[123] J. L. G. Fierro, J. Soria, J. Sanz, J. M. Rojo, *J. Solid State Chem.* **1987**, *66*, 154–162.

[124] S. Bernal, J. J. Calvino, G. A. Cifredo, J. M. Gatica, J. A. P. Omil, J. M. Pintado, *J. Chem. Soc. Faraday Trans.* **1993**, *89*, 3499–3505.

[125] J. El Fallah, S. Boujana, H. Dexpert, A. Kiennemann, J. Majerus, O. Touret, F. Villain, F. Le Normand, *J. Phys. Chem.* **1994**, *98*, 5522–5533.

[126] V. Perrichon, A. Laachir, S. Abouarnadasse, O. Touret, G. Blanchard, *Appl. Catal. A* **1995**, *129*, 69–82.

[127] L. A. Bruce, M. Hoang, A. E. Hughes, T. W. Turney, *Appl. Catal. A* **1996**, *134*, 351–362.

[128] A. Badri, C. Binet, J.-C. Lavalley, *J. Chem. Soc. Faraday Trans.* **1996**, *92*, 4669–4673.

[129] H.-T. Chen, Y. M. Choi, M. Liu, M. C. Lin, *ChemPhysChem* **2007**, *8*, 849–855.

[130] K. Werner, X. Weng, F. Calaza, M. Sterrer, T. Kropp, J. Paier, J. Sauer, M. Wilde, K. Fukutani, S. Shaikhutdinov, H.-J. Freund, *J. Am. Chem. Soc.* **2017**, *138*, 17608–17676.

[131] H. J. Freund, M. W. Roberts, *Surf. Sci. Rep.* **1996**, *25*, 225–273.

[132] C. Weilach, C. Spiel, K. Föttinger, G. Rupprechter, *Surf. Sci.* **2011**, *605*, 1503–1509.

[133] F. Mirabella, E. Zaki, F. Ivars-Barcelo, S. Schauermann, S. Shaikhutdinov, H. J. Freund, *J. Phys. Chem. C* **2018**, *122*, 27433–27441.

[134] M. Schwarz, F. Faisal, S. Mohr, C. Hohner, K. Werner, T. Xu, T. Skála, N. Tsud, K. C. Prince, V. Matolín, Y. Lykhach, J. Libuda, *J. Phys. Chem. Lett.* **2018**, *9*, 2763–2769.

[135] T. Kropp, J. Paier, J. Sauer, *J. Phys. Chem. C* **2017**, *121*, 21571–21578.

[136] D. Marrocchelli, B. Yildiz, *J. Phys. Chem. C* **2012**, *116*, 2411–2424.

[137] M. García-Melchor, N. López, *J. Phys. Chem. C* **2014**, *118*, 10921–10926.

[138] D. Fernández-Torre, J. Carrasco, M. V. Ganduglia-Pirovano, R. Pérez, *J. Chem. Phys.* **2014**, *141*, 014703.

[139] F. R. Negreiros, M. F. Camellone, S. Fabris, *J. Phys. Chem. C* **2015**, *119*, 21567–21573.

[140] O. Matz, M. Calatayud, *ACS Omega* **2018**, *3*, 16063–16073.

[141] M. B. Watkins, A. S. Foster, A. L. Shluger, *J. Phys. Chem. C* **2007**, *111*, 15337–15341.

[142] J. Höcker, T. O. Menteş, A. Sala, A. Locatelli, T. Schmidt, J. Falta, S. D. Senanayake, J. I. Flege, *Adv. Mat. Interfaces* **2015**, *2*, 1500314.

[143] K. Sohlberg, S. T. Pantelides, S. J. Pennycook, *J. Am. Chem. Soc.* **2001**, *123*, 6609–6611.

[144] X. Li, J. Paier, J. Sauer, *arxiv.org Condensed Matter* **2019**, DOI `arXiv:1904.13200`.

[145] P. Feulner, D. Menzel, *Surf. Sci.* **1985**, *154*, 465–488.

[146] C. H. F. Peden, D. W. Goodman, J. E. Houston, J. T. Yates, *Surf. Sci.* **1988**, *194*, 92–100.

[147] K. R. Hahn, M. Iannuzzi, A. P. Seitsonen, J. Hutter, *J. Phys. Chem. C* **2013**, *117*, 1701–1711.

[148] W. G. Reimers, M. A. Baltanás, M. M. Branda, *J. Mol. Model.* **2014**, *20*, 2270.

[149] X. Lu, W. Wang, S. Wei, C. Guo, Y. Shao, M. Zhang, Z. Deng, H. Zhu, W. Guo, *RSC Advances* **2015**, *5*, 97528–97535.

[150] D. Kong, J. Zhu, K.-H. Ernst, *J. Phys. Chem. C* **2016**, *120*, 5980–5987.

[151] T. Jin, Y. Zhou, G. J. Mains, J. M. White, *J. Phys. Chem.* **1987**, *91*, 5931–5937.

[152] C. Li, Y. Sakata, T. Arai, K. Domen, K.-i. Maruya, T. Onishi, *J. Chem. Soc. Faraday Trans.* **1989**, *85*, 929–943.

[153] C. Li, Y. Sakata, T. Arai, K. Domen, K.-i. Maruya, T. Onishi, *J. Chem. Soc. Faraday Trans.* **1989**, *85*, 1451–1461.

[154] L. G. Appel, J. G. Eon, M. Schmal, *Catal. Lett.* **1998**, *56*, 199–202.

[155] R. Farra, S. Wrabetz, M. E. Schuster, E. Stotz, N. G. Hamilton, A. P. Amrute, J. Pérez-Ramírez, N. López, D. Teschner, *PCCP* **2013**, *15*, 3454–3465.

[156] G. N. Vayssilov, M. Mihaylov, P. S. Petkov, K. I. Hadjiivanov, K. M. Neyman, *J. Phys. Chem. C* **2011**, *115*, 23435–23454.

[157] S. D. Senanayake, D. R. Mullins, *J. Phys. Chem. C* **2008**, *112*, 9744–9752.

[158] P. M. Albrecht, D.-e. Jiang, D. R. Mullins, *J. Phys. Chem. C* **2014**, *118*, 9042–9050.

[159] Y. Lykhach, T. Staudt, R. Streber, M. P. A. Lorenz, A. Bayer, H. P. Steinrück, J. Libuda, *Eur. Phys. J. B* **2010**, *75*, 89–100.

[160] T. Staudt, Y. Lykhach, N. Tsud, T. Skála, K. C. Prince, V. Matolín, J. Libuda, *J. Catal.* **2010**, *275*, 181–185.

[161] T. Staudt, Y. Lykhach, N. Tsud, T. Skála, K. C. Prince, V. Matolín, J. Libuda, *J. Phys. Chem. C* **2011**, *115*, 8716–8724.

[162] W. Taifan, J.-F. Boily, J. Baltrusaitis, *Surf. Sci. Rep.* **2016**, *71*, 595–671.

[163] X. Weng, Y. Cui, S. Shaikhutdinov, H.-J. Freund, *J. Phys. Chem. C* **2019**, *123*, 1880–1887.

[164] O. Seiferth, PhD Thesis, **1997**.

[165] B. H. Solis, Y. Cui, X. Weng, J. Seifert, S. Schauermann, J. Sauer, S. Shaikhutdinov, H.-J. Freund, *PCCP* **2017**, *19*, 4231–4242.

[166] O. Matz, M. Calatayud, *Private Communication* **2019**.

[167] S. L. Dudarev, G. A. Botton, S. Y. Savrasov, C. J. Humphreys, A. P. Sutton, *Phys. Rev. B* **1998**, *57*, 1505–1509.

[168] M. C. Padole, B. P. Gangwar, A. Pandey, A. Singhal, S. Sharma, P. A. Deshpande, *PCCP* **2017**, *19*, 14148–14159.

[169] T. Shimanouchi, *Tables of Molecular Vibrational Frequencies. Consolidated Volume I*, National Bureau of Standards, **1972**.

[170] T. Nakajima, T. Sonoda, H. Miyata, Y. Kubokawa, *J. Chem. Soc. Faraday Trans.* **1982**, *78*, 555–565.

[171] A. V. Ivanov, A. E. Koklin, E. B. Uvarova, L. M. Kustov, *PCCP* **2003**, *5*, 4718–4723.

[172] Y.-J. Wu, W.-H. Wang, C.-M. Chiang, *Langmuir* **2002**, *18*, 1449–1452.

[173] E. W. Zhao, H. Zheng, R. Zhou, H. E. Hagelin-Weaver, C. R. Bowers, *Angew. Chem. Int. Ed. Engl.* **2015**, *54*, 14270–14275.

[174] A. J. Roberts, S. Haq, R. Raval, *J. Chem. Soc. Faraday Trans.* **1996**, *92*, 4823–4827.

[175] J. P. Devlin, J. Sadlej, V. Buch, *J. Phys. Chem. A* **2001**, *105*, 974–983.

Acknowledgments

Doing a PhD is not an easy task. Luckily, I was surrounded by people that supported me all along the way. I am deeply grateful to everyone who stood by my side during the last three years, making me the scientist I am today.

First of all, I thank Prof. Hans-Joachim Freund for his trust in me, for his constant support, and his visions in the project. He gave me all possible opportunities to learn and grow, and initiated many scientific collaborations, from which this thesis benefited enormously. I also thank Prof. Klaus Rademann for his kind support as my second supervisor. I thank Shamil Shaikhutdinov, who supported my scientific work on a daily basis, for productive discussions and directions.

I thank Burkhard Kell for introducing me patiently to the peculiarities of the IRAS 2 setup, and for taking meticulous care of the lab. He and Uwe Härtel were invaluable supporters that faced every technical problem professionally and with a stoic smile on their faces. Without them, this work would certainly not have been possible.

I am grateful to many people for their scientific guidance. Among them are Florencia Calaza, who introduced me to CeO_2, and Xuefei Weng, who worked with me during the beginning of my thesis. I thank Ewa Nowicka for new perspectives - scientific and personal -, for her brilliant humor, and her sparking scientific enthusiasm. Furthermore, I thank Agata Płucienik, JianQiang Zhong, and Helmut Kuhlenbeck for their joint efforts to unravel the mysteries of the ceria surface. I thank Prof. Markus Wilde for his support in the NRA experiments, for a great many scientific discussions, and for his kind hospitality in Tokyo. I thank Prof. Weixin Huang and his group for their collaboration on the hydride project. Thomas Kropp, Xiaoke Li, and especially Joachim Paier and Prof. Joachim Sauer were an indispensable support on the theoretical side. I thank them for their patience and their tireless scientific efforts. Also Oliver Matz and Prof. Monica Calatayud-Antonino were valuable partners, who showed me new computational perspectives on the chemistry of ceria.

I thank Earl Davis and Spencer Carey for being wonderful friends and colleagues. They stood with me through all ups and downs of this work, gave me wise scientific advice, and always made me feel supported. I also thank Markus Heyde, for running breaks, encouragement, and creative inspiration.

I thank Manuela Misch and Daniela Nikolaus for their kind and professional help in everything that needed to be organized.

I thank Alex Paarmann, Bettina Menzel, Ines Bressel, and all members of the IMPRS. To me, the IMPRS was an institution that inspired me, gave me scientific insights outside of my field, and always made me feel at home. I thank Giacomo Melani in particular for being a great partner in the organization of our IMPRS Ringberg workshop.

With my whole heart, I thank my extended family, here in Berlin and elsewhere. Stephan, Manouk, Dante, and Jule, I count myself immensely lucky to have you by my side. Thank you for calls, cheer-ups, gift bags, food, coffee, and companionship. Frankly, thank you for everything. Especially Stephan - you were the best PhD trainer anyone can ask for.

Ganz besonders danke ich meiner Familie, allen voran meinen Eltern, für ihre stetige liebevolle Unterstützung und ihr nie endendes Vertrauen in mich.

Selbstständigkeitserklärung

Hiermit erkläre ich, die Dissertation selbstständig und nur unter Verwendung der angegebenen Hilfen und Hilfsmittel angefertigt zu haben. Ich habe mich nicht anderwärts um einen Doktorgrad in dem Promotionsfach beworben und besitze keinen entsprechenden Doktorgrad. Die Promotionsordnung der Mathematisch-Naturwissenschaftlichen Fakultät, veröffentlicht im Amtlichen Mitteilungsblatt der Humboldt-Universität zu Berlin Nr. 42 am 11. Juli 2018, habe ich zur Kenntnis genommen.

Berlin, 14.05.2019

Kristin Werner